APPLICATIONS OF MULTI-SPECTRAL LIDAR: RIVER CHANNEL BATHYMETRY AND CANOPY VEGETATION INDICES

MAXIM OKHRIMENKO
Bachelor of Science, Moscow Institute of Physics and Technology, 1999

A Thesis
Submitted to the School of Graduate Studies
of the University of Lethbridge
in Partial Fulfillment of the
Requirements for the Degree

MASTER OF SCIENCE

Department of Geography
University of Lethbridge
LETHBRIDGE, ALBERTA, CANADA

APPLICATIONS OF MULTI-SPECTRAL LIDAR: RIVER CHANNEL BATHYMETRY AND
CANOPY VEGETATION INDICES

MAXIM OKHRIMENKO

Date of Defence: April 23, 2018

Dr. C. Hopkinson Supervisor	Professor	Ph.D.
Dr. C. Coburn Thesis Examination Committee Member	Associate Professor	Ph.D.
Dr. D. Peddle Thesis Examination Committee Member	Professor	Ph.D.
Dr. L. Spencer Thesis Examination Committee Member	Associate Professor	Ph.D.
Dr. P. LaRocque External Examiner Teledyne Optech Inc. Vaughan, Ontario	Vice President Special Projects	Ph.D.
Dr. S. Kienzle Chair, Thesis Examination Committee	Professor	Ph.D.

ACKNOWLEDGEMENTS

ABSTRACT

This thesis investigates the potential of new state-of-the-art multi-spectral (ms) lidar technology and develops methodologies for applications in water, wetlands, and forest resource monitoring. The scope of the thesis is split into two parts – lidar bathymetry and lidar radiometry. The first topic addresses the need for urban river environment bathymetry and refining of ms lidar data processing routines in complex riparian environments. The second topic presents a framework of experiments to investigate ms lidar radiometry.

As a result, a new routine for bathymetric correction was developed. The consistency of spectral vegetation indices (SVIs) through a variety of altitudes was investigated. Radiometric targets were constructed and, after radiometric calibration, comparability of reflectance values derived from ms lidar data to available spectral libraries was shown. Finally, forest plot-level canopy vertical SVI profiles were developed while attempting to understand attenuation losses due to sub-footprint reflectors within the canopy by means of additional complex radiometric targets.

TABLE OF CONTENTS

LIST OF TABLES

LIST OF FIGURES

LIST OF SYMBOLS & ABBREVIATIONS

< > - Average

$\overline{(\ )}$ - Mean

AGL - Above Ground Level

ALS - Airborne Laser Scanning

AOI - Areas Of Interest

AOP - Apparent Optical Properties

APD - Avalanche Photodiode

ASD - Analytical Spectral Devices

AVIRIS - Airborne Visible/Infrared Imaging Spectrometer

BRDF - Bidirectional Reflectance Distribution Function

C1 - channel 1 of Titan sensor

C2 - channel 2 of Titan sensor

C3 - channel 3 of Titan sensor

DEM - Digital Elevation Model

DN - Digital Number

DR - Discrete Return

DTM-W - Digital Terrain Model of the Watercourse

FOV - Field of View

FWF - Full-Waveform

GIS - Geographic Information System

GNSS - Global Navigation Satellite System

GPS - Global Positioning System

H1(2,3) - Heights

IMU - Inertial Measurement Unit

IOP - Inherent Optical Properties

K_d - diffuse attenuation coefficient

Lidar – Light Detection and Ranging

LMS - LiDAR Mapping Suite

LP - Lodgepole Pine

MIR - Middle-Infrared

ms – multi-spectral

NDII - Normalized Difference Infrared Index

NDVI - Normalized Difference Vegetation Index

NIR - Near-Infrared

NOAA AVHRR - Advanced Very High-Resolution Radiometer

NTU - Nephelometric Turbidity Units

nδ - Normalized Difference Index

OTS - Off-the-Shelf

P90 - 90th Percentile

PRF - Pulse Repetition Frequency

RMSE - Root Mean Square Error

SBET - Smoothed Best Estimate of Trajectory

SD - standard deviation
SVI - Spectral Vegetation Index
sw - Swath Width
SWIR - Short-Wave Infrared
sρ - Simple Ratio Index
USGS - United States Geological Survey
WSM - Water Surface Model
Z - Height

1   Introduction

1.1   Introduction

Research into multi-spectral lidar applications became of interest after

Teledyne Optech introduced its new Titan sensor in 2014 with three active beams at

wavelengths of 532 nm, 1064 nm, and 1550 nm. Although it is claimed to be the first

multi-spectral lidar sensor by its manufacturer ("Optech Titan," January, 2017),

development of dual-wavelength sensors for coastal water bathymetry started more

than two decades earlier (Irish & Lillycrop, 1999; Penny, Billard, & Abbot, 1989).

Furthermore, the concept of a multi-spectral lidar with four different wavelengths for

assessing forest structural and physiological information was studied by Morsdorf et

al. (Morsdorf, Nichol, Malthus, & Woodhouse, 2009) in 2009 with a description of a

demonstration project published in 2011 (Woodhouse et al., 2011). Regardless, the

Titan sensor represents the state-of-the-art in multi-spectral lidar, producing actual

datasets at three wavelengths. This technology introduces the potential to develop

new methods in water and forest resource monitoring – these enhancements will be

discussed in this thesis.

1.2   Thesis Organization

This thesis is divided into five chapters. Chapter I provides an overview of

airborne lidar technology and a brief description of the Teledyne Optech Titan multi-

spectral sensor. The purpose of the overview is to provide a brief introduction to the

technology and theory, thus allowing progress through the thesis without referring

to additional sources. Chapters II, III, and IV are presented in paper form, each with its

own introduction, data, results, and conclusion sections. Chapter II showcases a

bathymetric survey of the Bow and Elbow rivers in Calgary; Chapter III investigates

consistency of spectral vegetation indices derived from multi-spectral lidar data at

three different survey altitudes; Chapter IV presents a radiometric calibration target

experiment set up to study multi-spectral lidar radiometry and construction of

vertical spectral vegetation indices. Chapter V concludes the thesis, summarizing the

main results and key findings, and discusses future work.

1.3   Objectives of the study

The objective of the bathymetric study was to address knowledge gaps in

river-bed monitoring in urban areas. Recent floods in Canada have increased the

interest in improved flood modelling based on riverbed geomorphology data which

may be collected by multi-spectral lidar systems. However, depth performance of the

system varies with water turbidity and while depth cut off at ~6 m was reported in

nearshore ocean waters (Fernandez-Diaz et al., 2016), limitation in fluvial bathymetry

application has not yet been tested. Industrial applications require prediction of the

maximum penetration depth with readily accessible data, which has yet to be

developed. Moreover, bathymetric correction should be applied to raw data based on

proximity to the overlying water surface. Currently, ms lidar bathymetric correction

algorithms within off-the-shelf (OTS) software were developed for coastal waters and

lakes, and therefore have difficulties with rivers possessing high stream gradients. In

addition, riparian zones with overhanging tree crowns combined with urban built

environment may lead to a complication in water surface detection and resulting

bathymetric correction. Thus, the first research chapter (Chapter II) will test ms lidar bathymetry in an urban environment and refine data processing routines in a complex river corridor surroundings.

The objective of the radiometric study was to focus on radiometric calibration of ms lidar intensity data and on development of active spectral indices. In passive EO imagery, numerous Spectral Vegetation Indices (SVIs) were developed based on reflectance values derived from image-based digital numbers (DNs) as quantitative indicators of vegetation phenology characteristics, including long-term patterns of loss or growth of photosynthesizing foliage (Bannari, Morin, Bonn, & Huete, 1995). In recent years, a few publications have considered multi-spectral lidar for land surface classification using development of active SVIs from ms lidar (Morsy, Shaker, & El-Rabbany, 2017; Morsy, Shaker, El-Rabbany, & LaRocque, 2016). Within a forestry context, successful classification of vegetation has only recently been achieved using SVIs, specifically with normalized difference vegetation indices (NDVI) (Budei, St-Onge, Hopkinson, & Audet, 2018). Moreover, a potential of measuring plant physiology, leaf moisture content, and leaf-bark separation by generating vertical profiles of spectral indices was shown by modelling and laboratory experiments (Hancock, Gaulton, & Danson, 2017; Morsdorf et al., 2009; Woodhouse et al., 2011). However, for consistency over time and comparability with other sensors, SVIs should be calculated with reflectance derived from the lidar intensity DNs after rigorous radiometric correction (Yan, Shaker, Habib, & Kersting, 2012). For single-channel lidar, there is over a decade of published research into target-based radiometric calibration

(Kaasalainen et al., 2009), but such approaches are yet to be applied in operational

ms lidar SVI derivation. However, in practice, using calibration targets often is not

feasible and one can foresee a widespread use of SVIs derived directly from

uncorrected ms lidar DNs (Hopkinson, Chasmer, Gynan, Mahoney, & Sitar, 2016).

Chapter III will address the question of consistency of spectral indices, derived

without additional calibration, across multiple landcovers and when undergoing

different rates of signal attenuation, such as through canopy and with altitude.

Chapter IV will concentrate on results of target-based radiometric calibration of ms

lidar – comparability of derived reflectance values with spectral signatures obtained

with other instruments (hyperspectral cameras, analytical spectral devices - ASDs)

and development of plot-level canopy vertical SVI profiles, while attempting to

understand channel-based attenuation losses due to smaller-than-the-footprint

reflectors within canopy by means of additional complex radiometric targets.

1.4   Overview of airborne lidar principles

1.4.1   History

Lidar (light detection and ranging) is an active optical time-of-flight measurement

system which allows computing a distance from the system to a target. Initial work

on time-of-flight ranging systems used radio waves and the technology is known as

radar – radio detection and ranging (Skolnik, 2008). According to (Vosselman & Maas,

2010), the fundamental work can be traced back to Hertz and his experiments at the

end of the nineteenth century. By the late 1950s, lasers (light amplification by

stimulated emission of radiation) were invented, and it became possible to achieve

higher range and angular resolutions than those of radar. Early attempts to use laser scanners on airborne platforms started in the 1970s, however, only with the introduction of differential GPS (Global Positioning System), the sub-decimetre accuracy in measurements of the vertical and horizontal position of the scanner during flight became achievable (Friess, 1989). Adoption of IMU (Inertial Measurement Unit) technology in combination with differential GPS technology along with Kalman filtering provided sufficient accuracy – currently the accuracy of a reconstructed flight path can be better than 5 cm - for airborne laser scanning (ALS) from the beginning of the 1990s (Schwarz, Chapman, Cannon, Gong, & Cosandier, June 6-10, 1994, Ottawa).

1.4.2   *Time-of-flight measurements*

A fundamental property of light is its constant propagation velocity through a given medium. Thus, a distance (also referred to as range ρ) from a source to a reflective target can be calculated by measuring the time delay (τ) between emitted and received signals (assuming that the source and the receiver are at the same point in space) (Vosselman & Maas, 2010):

$$\rho = \frac{c}{n}\frac{\tau}{2} \quad . \hspace{3cm} \text{Equation 1.1}$$

In the *Equation 1.1*, *c* denotes the speed of light in a vacuum and *n* is the refractive index of the medium. The defined value for *c* is *299 792 458 m/s*. If the light waves travel in air, the corresponding refractive index depends on the air temperature,

pressure and humidity, and is estimated for standard values as $n \approx 1.00025$ (*Vosselman & Maas, 2010*).

Due to the potential complexity of a surveyed scene (e.g., forest canopy) and a given finite radius of the emitted beam, more than one backscattered echo can be detected by the receiver from one pulse emitted by the source (Hofton, Minster, & Blair, 2000). By design, most airborne lidar sensors measure and store time stamps for at least the first returned echo and the last returned echo for each emitted pulse. Currently, most systems are able to capture from four to eight separate echoes.

Because of the separation between multiple echoes from one emitted pulse, it is essential to understand limitations of the system due to emitted pulse shape. The characteristics of a transmitted pulse are the pulse width (t_p) and the pulse rise time t_r. A typical pulse is Gaussian with a pulse width (measured as the time interval between the half-peak-power points, also called full width half maximum - FWHM) (t_p) = *4 ns*, which corresponds to a length (l_p) of about 1.2 m at the speed of light, and a pulse rise time (t_r) *of 3 ns*, which corresponds to a length (l_r) of 0.9 m. It is assumed, that the two echoes can be separated if corresponding received signals do not have an overlap at FWHM, which leads to the following bounding equation (Baltsavias, 1999a):

$$\Delta \rho \geq \frac{1}{2} l_p \quad .$$
<div align="right">Equation 1.2</div>

For example, two echoes can be discriminated if the distance between them is larger than half the pulse length. For example, with pulses of width *5 ns*, it is possible to separate two targets only if their relative distance along the beam propagation is larger than 0.75 m.

There are three main detection methods to trigger an echo record (Vosselman & Maas, 2010): peak detection – at the maximum amplitude of the echo; leading edge detection – when the rising edge of the echo exceeds a predefined threshold; constant fraction detection – at the time an echo reaches a pre-set fraction of its maximum amplitude. Each method has its advantages and they are discussed in detail in (Wagner, Ulrich, Melzer, Briese, & Kraus, 2004). The range uncertainty (δ) is given by the formula (Wehr & Lohr, 1999):

$$\delta = \frac{c}{2}\frac{t_r}{\sqrt{SNR}} \quad , \qquad \text{Equation 1.3}$$

where the SNR is the signal to noise ratio (ratio of signal power of the photodiode current to thermal noise power of the photodiode and amplifier).

1.4.3   *On-board components and laser scanner properties*

The airborne laser scanning technique is based on two major components – a laser scanner system for ranging and a GNSS (Global Navigation Satellite System)/IMU combination to record the exact position and orientation of the system. The accuracy of the trajectory of an airborne lidar platform obtained from a GNSS/IMU unit adds to

the error budget of the final ranging product. Contemporary systems achieve

trajectory accuracies of < 5 cm under ideal conditions.

The main components of the laser scanner system are a light source, a

modulation unit, focusing optics, projection mechanism, collection optics,

photodetector, and received signal processing unit. Typically, the light source

consists of a laser with a wavelength in the range of 0.4 to 1.6 µm with a spectral

width between 0.1 and 0.5 nm. Eye safety is a factor which depends on the chosen

wavelength (visible light is more damaging to a human eye compared to longer

wavelengths) and thus limits are placed on the maximum allowed power at a given

beam divergence and flight altitude (ANSI, 2007). The modulation unit is responsible

for Pulse Repetition Frequency (PRF) and in contemporary systems provides up to 1

000 000 pulses per second (referred as PRF = 1000 kHz). Focusing optics illuminate an

area A_f on the ground (often referred as a footprint), which is given by the formula

(Baltsavias, 1999a):

$$A_f = \frac{\pi}{4}(D + \rho\gamma)^2 \quad , \qquad\qquad \text{Equation 1.4}$$

where γ (full angle in radians) is the laser beam divergence, the ρ is the range, and D

is the aperture of the laser (often is neglected in comparison to $\rho\gamma$). A projection

mechanism moves the laser beam over the surface of the object. There are four most

commonly used scanning mechanisms – oscillating mirror, rotating polygon, palmer

scan, and fiber scanner (Wehr & Lohr, 1999). Each of them produces a unique ground

pattern (Figure 1.1).

8
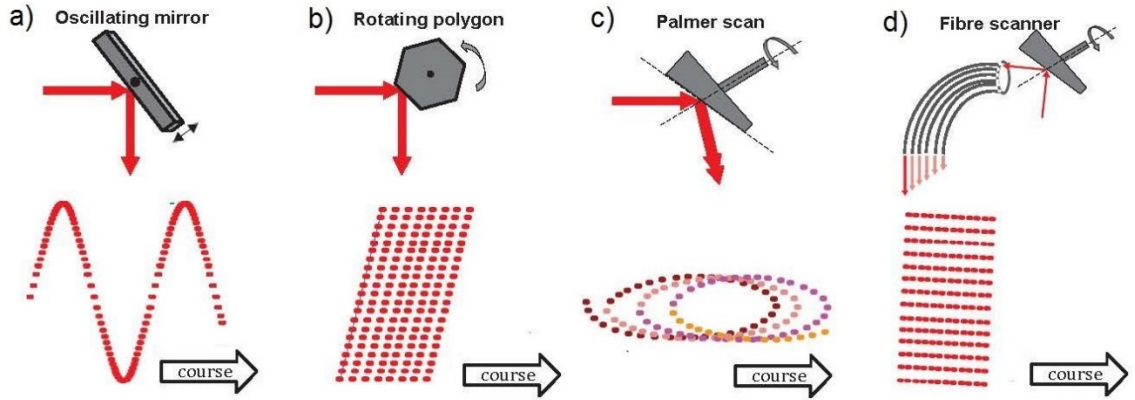
Figure 1.1 Scanning mechanisms and resulting ground patterns. a) – Oscillating mirror; b) – rotating polygon; c) – Palmer scanner; d) – Fiber scanner. Adapted from (Vosselman & Maas, 2010).

The Teledyne Optech Titan sensor uses an oscillating mirror mechanism (Figure 1.2), which features a zigzag pattern on the ground with larger across-track point spacing in the middle of the swath and smaller at the ends. The swath width (*sw*) of a scanner is given by (Wehr & Lohr, 1999):

$$sw = 2\,h\tan\left(\frac{\theta}{2}\right) \quad ,$$

Equation 1.5

where θ is the full scan angle and h is the height above ground. The collection optics are characterized by aperture diameter (D_r) and photodetectors, which are typically avalanche photodiodes (APDs). Finally, a received signal processing unit is responsible for echo triggering and storage.

Currently, there are two distinct approaches to backscatter signal retrieval: i) real-time echo triggering systems and ii) storing the complete received signal waveform. The first type is often referred to as discrete return (DR) because the output of the measurement is an echo range and a peak amplitude of the signal

(referred to as DR intensity). In such systems, for one outgoing pulse multiple backscattered echoes can be recorded. The second type of retrieval system does not process the backscatter signal on the fly, but stores the entire "waveform" by sampling the returned signal from each emitted pulse at some constant rate (typically at 1 ns interval) and often are called full-waveform (FWF) systems.

1.5   Descriptions of the Teledyne Optech Titan multi-spectral sensor

A detailed description of the Teledyne Optech Titan system can be found in (Fernandez-Diaz et al., 2016). The main characteristics are summarized in Table 1.1. Non-collinear laser beam channels are a significant feature of the system; Figure 1.2 illustrates the resulting ground pattern of Titan`s swath. The full specification provided by the manufacturer can be found in Appendix I.

Table 1.1 Performance specifications of each of the Titan`s channels. Adopted from (Fernandez-Diaz et al., 2016) and corrected after personal communication with Teledyne Optech (Paul LaRocque).

Channel	C1	C2	C3
Laser wavelength (nm)	1550	1064	532
Look angle (degrees)	3.5 forward	nadir	7.0 forward
Pulse Repetition Frequency (kHz)	50-300	50-300	50-300
Beam Divergence at 1/e, (mRad)	0.35	0.35	0.7
Pulse Energy (μJ)	50-20	~15	~30
Pulse Width (ns)	3.0 - 3.5	3.0 - 3.5	2.5 - 3.0
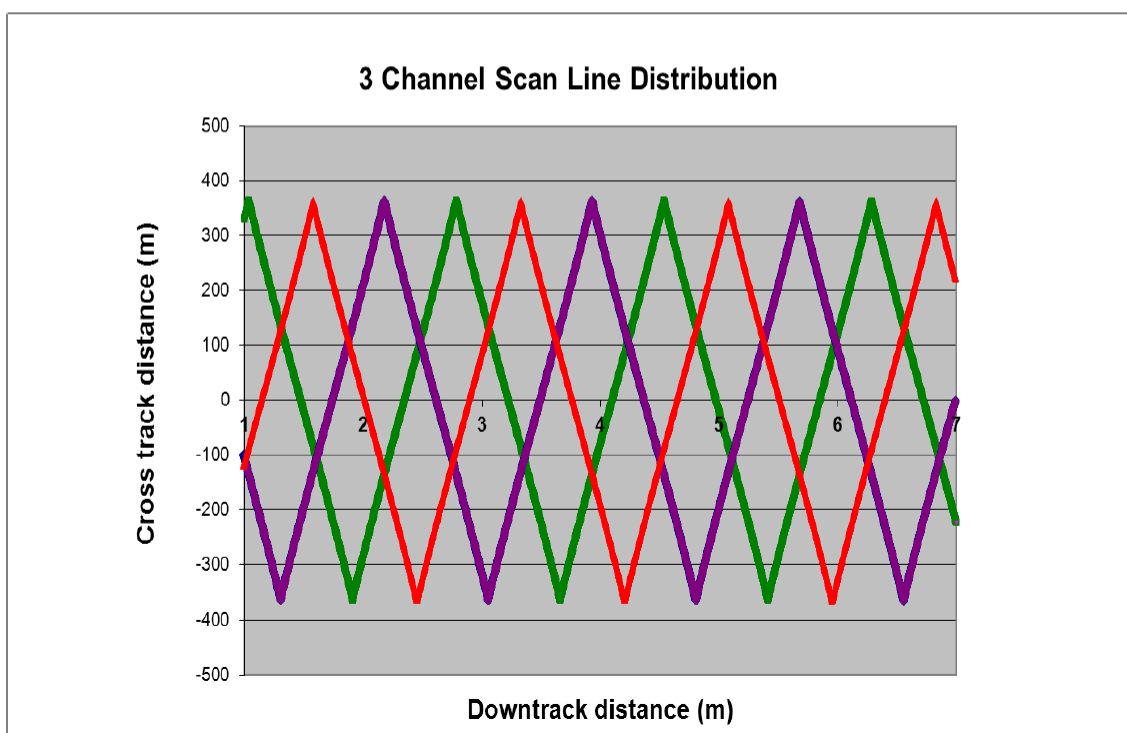
Figure 1.2 Ground pattern of Teledyne Optech Titan sensor. Adapted from (P. LaRocque, Smith, & Shaker, June, 2015). The actual scan pattern at ground level varies with PRF, scan frequency, scanner field of view and flying altitude above the target terrain.

2 Urban river environment digital water surface model generation and in situ bathymetric correction using multi-spectral LiDAR

Abstract

Airborne lidar bathymetry has been evolving in recent years and an introduction of multi-spectral lidar, such as Titan sensor from Teledyne Optech, allows for simultaneous mapping of aquatic and riparian areas. Recent floods in Canada have increased the interest in improved flood modeling based on riverbed geomorphology data which may be collected by such multi-spectral lidar systems. However, bathymetric correction should be applied to raw data based on proximity to the overlying water surface. Current algorithms within off-the-shelf (OTS) software were developed for coastal waters and lakes, and therefore have difficulty with rivers possessing high stream gradients. The objective of this thesis chapter is to present (i) a new methodology of *in situ* bathymetric correction, (ii) method of deriving digital water surface model, and (iii) a preliminary analysis of Titan sensor depth performance from an inland urban river case study environment.

Lidar data were collected over two areas of interest (AOI) inside the Calgary City limits, featuring Bow River as the first AOI and Elbow River as the second, with a Teledyne Optech Titan multi-spectral system. The lidar system collected data at three wavelengths: 1550 nm, 1064 nm, and 532 nm. Planned survey parameters were 200 kHz per channel with 36 degrees field of view. Flight lines were planned with 50% overlap at an altitude of 500 m above ground and provided double coverage for all overlapping lines with a planned pulse density of 18 points per square meter per

channel or 56 points per square meter overall. A proposed simplified correction

algorithm is based on a shift (scaling with k = 0.763) in height values of riverbed

returns, normalized toward the overlying water surface, and disregards dependence

from a laser beam angle of incidence for each point. For this purpose digital water

surface models (WSM) have been developed based on virtual transects derived from

lidar points within *a priori* defined water boundaries. The resulting correction proved

superior to that of the OTS software. In addition, water surface variations of up to 80

cm were observed across two channels of the river around a small island, illustrating

that assuming locally flat water surfaces is not a viable approach for robust

bathymetric correction in dynamic river environments.

2.1   Introduction

River environments are dynamic, and accurate bathymetric data are vital

sources of information needed for the mapping and management of the riparian

zone (Lane & Chandler, 2003). The need for accurate mapping is especially acute

when rivers and human settlements intersect in flood-prone areas (Grunthal et al.,

2006). Rapid changes in channel morphology is common and information related to

these spatial and temporal changes are vital for our understanding of these

environments (Dutta, Herath, & Musiake, 2006).

Airborne lidar has established itself during the past two decades as a unique

high-resolution remote sensing technology in land management due to its 3D

sampling of land cover and terrain, and its ability to penetrate into vegetation from

treetop to ground (Baltsavias, 1999b; Glennie, Carter, Shrestha, & Dietrich, 2013). At

the same time, airborne lidar bathymetry has been rapidly evolving in the context of capturing shallow water bodies, utilizing either a green laser due to its better penetration (Fernandez-Diaz et al., 2014) or a combination of green and near-infrared laser beams for better water surface detection (G. C. Guenther, Brooks, & LaRocque, 2000; Irish & Lillycrop, 1999; Mandlburger, Pfennigbauer, & Pfeifer, 2013). Cutting-edge lidar technology produces active multi-spectral (ms) 3D imagery, which allows multipurpose spectral sampling of land cover combined with moderate bathymetric capabilities for shallow coastal and river waters (Fernandez-Diaz et al., 2016; Hopkinson et al., 2016).

With ms lidar, it is possible to enhance computational fluid dynamic models of water flow by utilizing precise Digital Terrain Models of the Watercourse (DTM-W) derived from lidar data and map vulnerable areas (Mandlburger & Briese, 2007). A recent flood event in Calgary (Whitfield & Pomeroy, 2016) made flood risk assessment of high public concern and has increased the interest in improved flood modeling based on riverbed geomorphology data. This paper presents results of a bathymetric case study at the Bow and Elbow Rivers within the City of Calgary using an ms lidar Titan sensor from Teledyne Optech.

2.1.1 Maximum penetration depth (depth performance)

From a practical/data collection/survey point of view, it is important to estimate depth performance (how deep lidar pulse can penetrate into the water) of the lidar sensor ahead of the bathymetric survey (G. C. Guenther, Cunningham, LaRocque, & Reid, 2000). Previously, depth performance for bathymetric lidar

sensors was often given using a Secchi depth definition (Tyler, 1968) because it is an old and intuitive measure of water clarity. However, Secchi depth is not a good predictor of maximum penetration depth (G. C. Guenther et al., 2000), due to its relationship to the diffuse attenuation coefficient (Gordon, 1989; Gordon, Brown, & Jacobs, 1975). A more accurate parameter describing depth penetration utilizes the scattering-to-absorption ratio (Gordon et al., 1975). For the Teledyne Optech Titan sensor, the system specification (Appendix I) provides depth performance (D_{max}) in form of:

$$D_{max}(m) = \frac{1.5}{K_d} \quad ,$$

<div align="right">Equation 2.1</div>

where K_d is the diffuse attenuation coefficient of the water. Additional conditions from the specification are 20% reflective surface or bottom and operating altitudes from 300 m to 600 m above ground level, noting that lower operating altitudes may be required to ensure measurable returns from low reflectance targets at 532 nm.

Whereas inherent optical properties (IOP), such as absorption and scattering, depend only on the medium, the apparent optical properties (AOP) such as K_d depend not only on the medium, and thus from IOPs, but from the illumination source and viewing geometry as well (Legleiter et al., 2016). However, both IOP and AOP measurements are rarely available. Meanwhile, nephelometric turbidity, an index of light scattering by suspended particles, which lacks the physical basis of IOPs, is widely used in water clarity monitoring because of its simplicity and cost-effectiveness (Davies-Colley & Smith, 2001). By utilizing an empirical model, such as

(Davies-Colley & Nagels, 2008), it is possible to estimate corresponding K_d values

from available nepholometric turbidity values and, consequently, predict depth

performance of a given lidar sensor.

2.1.2   Bathymetric correction

To produce DTM-W, the positions of lidar returns need to be corrected for the

refraction of green light in the water. This procedure is referred to as bathymetric

correction. Normally, the bathymetric correction takes into account the exact

distance the laser beam traveled through the water and recalculates lidar point

positon utilizing Snell`s law of refraction (Westfeld, Maas, Richter, & Weiss, 2017). As

inputs for recalculating each lidar point position, it requires the exact sensor

coordinates and a WSM. Usually, corrected data are provided by a vendor and rely on

OTS proprietary software. However, if the resulting correction from the OTS

software is not acceptable, it is useful for an end user to have an independent and

alternative algorithm, i.e., an *in situ* bathymetric correction that uses data attributes

available to the end user.

For an *in situ* bathymetric correction, a simpler end user approach can be

developed with minor loss of precision using the outputted high-quality data pre

bathymetric correction. Light beam refraction is described by Snell`s law:

$$\frac{\sin \theta_{air}}{\sin \theta_{water}} = \frac{n_{water}}{n_{air}} \quad , \qquad \qquad \text{Equation 2.2}$$

where n_{air} and n_{water} are refractive indices in air and water. For the estimation, n_{air}

can be approximated to *1,* disregarding the difference between the speed of light in

air compared to vacuum. Introducing a virtual path of a laser ray without refraction L_{virt} in water and corresponding depth D_{virt} of water together with actual refracted path L_{water} and corresponding actual depth D_{water} (Figure 2.1), the dependence of D_{water} on D_{virt} and angle of incidence θ_{air} can be written as:

$$D_{water} = D_{virt} \frac{1}{n_{water}} \frac{\sqrt{1 - \frac{\sin^2 \theta_{air}}{n_{water}^2}}}{\cos \theta_{air}} \ . \qquad \text{Equation 2.3}$$

Introducing projections of the L_{virt} and L_{water} on the XY plane (Figure 2.1), their difference dXY can be calculated as a function of D_{virt} and angle of incidence θ_{air}:

$$dXY = D_{virt} \tan \theta_{air} \left[1 - \frac{1}{n_{water}^2} \right] \ . \qquad \text{Equation 2.4}$$
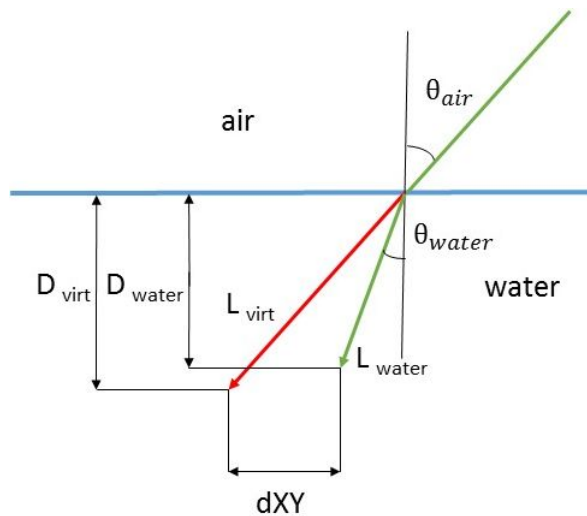
Figure 2.1 Diagram showing the refraction of green light at an air/water interface.

Both functions are presented in graphical form In Figures 2.2 and 2.3 for easier

interpretation. On the first graph (Figure 2.2), angles of incidence from 7° to 19°,

which are corresponding to common flight parameters, are highlighted in red.
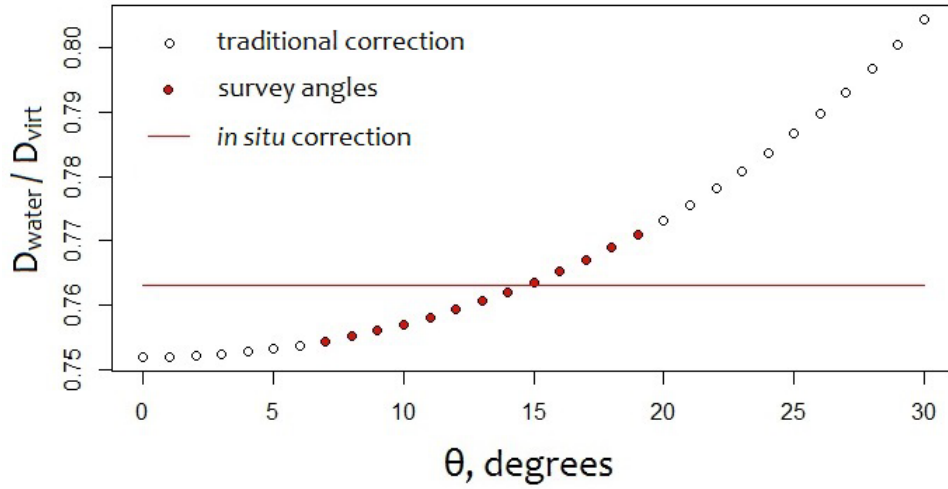
Figure 2.2 D_{water}/ D_{virt} as a function of beam angle of incidence θ^{air}. Proposed correction scaling coefficient depicted by red line.
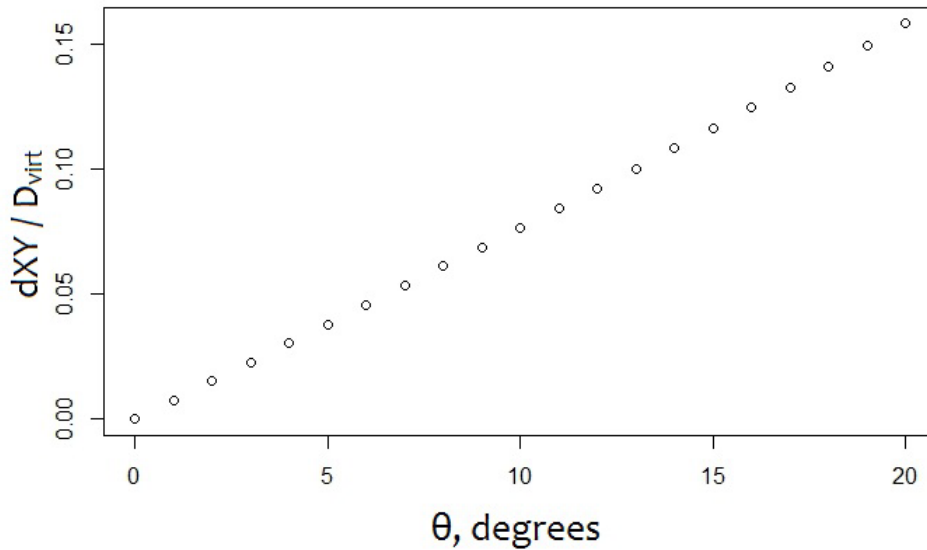
Figure 2.3 dXY/D_{virt} as a function of angle of incidence θ_{air} .

The plot on Figure 2.2 allows to infer that the difference in bathymetric

correction in depth for different angles of incidence should be less than 2% - the range

of variations in $D_{water}/D_{virtual}$ ratio is from 0.75 to 0.77 - in case of simplistic flat water

surface and laser beam angles of incidence less than 20 degrees. Thus, for shallow

rivers such as Bow River and Elbow River, with a maximum depth of up to 2 meters

and an average depth of less than 1 meter, the difference in vertical correction should

be less than 4 cm with an average difference of less than 2 cm. The difference in plane

dXY due to refraction is bigger (Figure 2.3) and has almost linear dependence on the

angle of incidence, measured in degrees, starting from 0% of virtual depth at nadir

and reaching 15% of virtual depth at 20 degrees. If neglecting correction, it would lead

to a maximum shift of 30 cm in plane for a 2 m water column which is often smaller

than the green lidar beam footprint diameter (50 cm at $1/e^2$ for the case study). As a

result, for an estimate (*in situ* bathymetric correction), a simple scaling of D_{virt} with a

coefficient 0.763 (Figure 2.2) can be made to calculate D_{water}, and a correction in the

XY plane can be neglected.

2.1.3   *Water Surface Model*

Regardless of the complexity of a chosen bathymetric correction approach (*in*

situ vs traditional), it is essential to build a correct and full WSM. In complex cases,

such as high stream gradients, built environments, and/or other natural obstacles,

such as tree crowns, algorithms for land-water classification and water surface

detection (Morsy et al., 2016) may experience difficulties if they were developed for

coastal waters and lakes . Consequently, many algorithms disregard *a priori* known

information, such as approximate water boundaries, which might be key for successful implementation.

Results of hydrodynamic modelling show that transverse inclination of water surface happens only where open channels bends (Blanckaert et al., 2013; Wu, Rodi, & Wenka, 2000). If one can disregard the transverse inclination, it can be argued that having at least one point of water surface lidar return in case of a small to moderate sized river would allow to draw a horizontal transect water surface line and then gradually build an "artificial" water surface model based on a number of these surface transect lines. Such a procedure excludes radiometric analysis required for known algorithms (Morsy et al., 2016) provided that some *a priori* information is available. However, it relies on the assumption of water surface elevation uniformity within stream cross-sections.

2.1.4 *Objectives*

The objectives of this paper are: (i) presenting a new and user-friendly methodology of approximate bathymetric correction without utilizing exact sensor coordinates, (ii) developing a semi-automated method for deriving a digital WSM based on virtual transects and assessing the viability of the surface elevation uniformity within stream cross-sections assumption, and (iii) analyzing system`s depth performance from the case study.

2.2   Study site and data

Lidar data were collected on the night of August 9th, 2016 over two Areas Of Interest (AOI) inside the Calgary City limits (Figure 2.4), featuring Bow River as the first AOI and Elbow River as the second, with the multi-spectral Teledyne Optech Titan system mounted onboard a Piper Navajo fixed wing aircraft. The lidar system collected data at three wavelengths – 1550 nm, 1064nm, and 532 nm corresponding to the system`s channels referred to as C1, C2, and C3, respectively. Planned survey parameters were 200 kHz per channel with a 36 degrees Field Of View (FOV) and a 44 Hz scanning frequency. Flight lines were planned with 50% overlap at an altitude of 500 m above ground which provided double coverage for all overlapping swath lines. The planned pulse density was 18 points per square meter per channel or 56 points per square meter overall.

Raw data in the form of range file and SBET file (Smoothed Best Estimate Trajectory) were processed in LMS (Lidar Mapping Suite, proprietary software from Teledyne Optech) and, after block adjustment, point cloud data were obtained with verified accuracy (over available rooftops) of Root Mean Square Error (RMSE) < 0.06 m in horizontal separation and RMSE < 0.04 m in height separation. Data were output with and without LMS bathymetric correction for C3 channel.
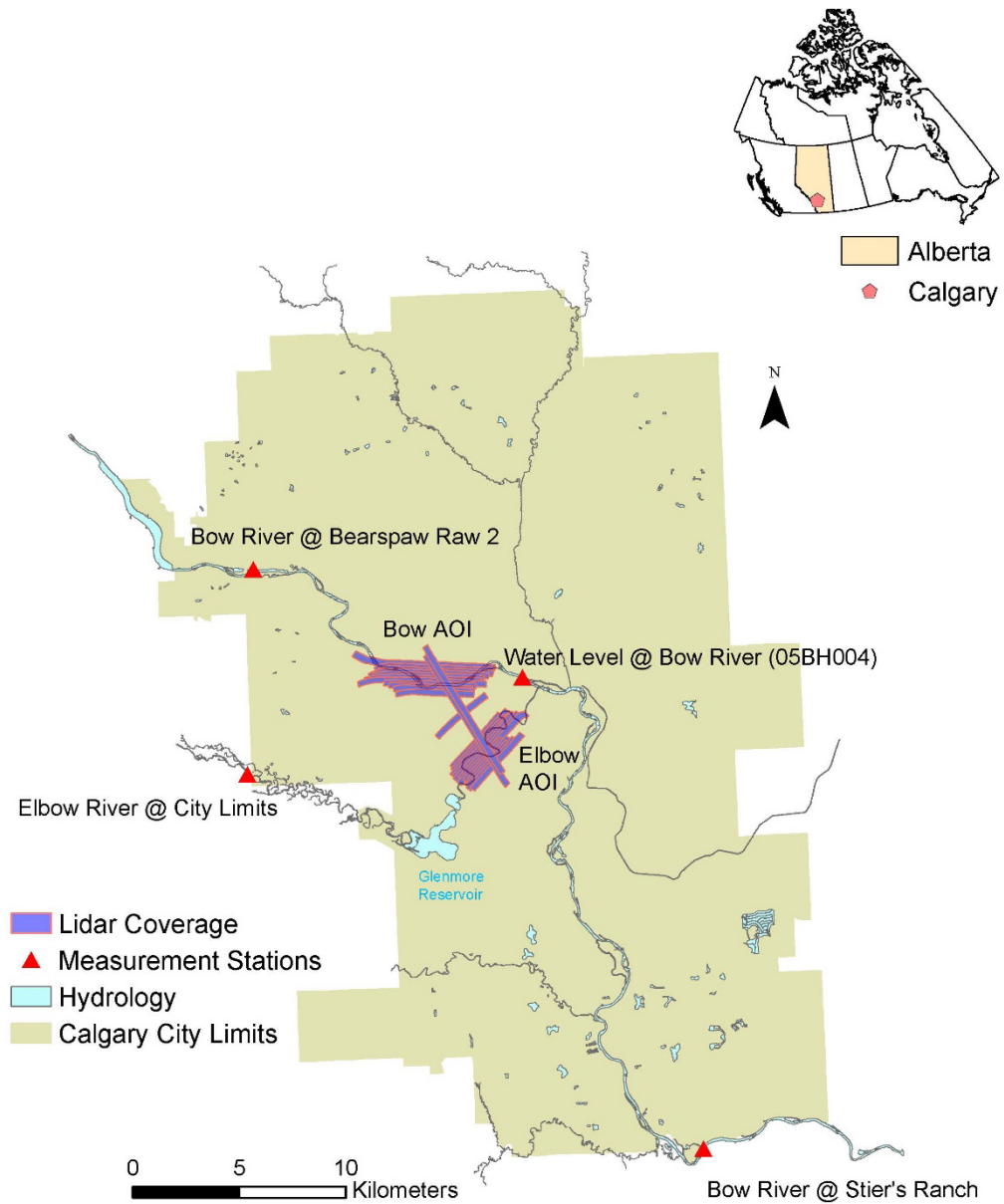
Figure 2.4 Map of lidar coverage, turbidity measurement stations, and water level measurement station.

Water turbidity data were received from the City of Calgary for three locations (Figure 2.4). The water level measured by permanent station 05BH004 (Environment-Canada, 2016), approximately 2 km downstream from the Bow River AOI (Figure 2.4) during the time of survey, was 1.2 m above the gauge. This value is close to an

average for this time of the year and roughly 20 cm higher than the annual minimum of approximately 1.0 m (Environment-Canada, 2016). A water boundary polygon was retrieved from the City of Calgary web portal (Calgary, 2016).

In the case study area, both rivers have moderate stream gradients up to 1 m rise over 300 m run; furthermore, a mix of natural and urban environments provides a lot of "obstacles" in the laser pulse path above the water surface, such as tree crowns, power lines, and bridges. The river bed consists of mid-size boulders and sediments, with aquatic plants largely absent or extremely rare in the AOIs.

2.3   Methods

2.3.1   Virtual Water Surface Model development

For creating WSM, a three-step method was used. In the first step, a river centerline with 1 m increments was digitized based on the hydrology feature layer provided by the City of Calgary. Points were saved into a text file as an input for the third step. In addition, a polygon with a 1 m buffer was created around the centerline and kept as an input for the second step. All manipulations in the first step were done in the ArcGIS (ESRI Canada) software.

In the second step, the polygon created in the step one was used to clip points from near-infrared channels (C1 and C2) in LAStools proprietary software (Isenburg, 2016). Resulting points were output into a text file as a second input for the third step.

In the third step, a Python script (Okhrimenko, 2017) takes two text files from the previous steps as an input and produces a virtual water surface model based on the elevation of the clipped points. The script creates area bins around centerline points limited by virtual one-dimensional transects (lines perpendicular to the centerline) and calculates mean elevation values inside the bins. Then, it creates points along a transect line – one transect line associated with each point of the centerline - with a 1 m distance between created points along the transect line, and assigns elevation calculated from the associated bin for each point. Thus, it creates an "artificial" point cloud which represents a virtual water level (or virtual WSM) extended beyond water boundaries along a transect by a length of an arbitrarily chosen parameter (250m in case of the Bow River and 150 meters in case of the Elbow River). The diagram in Figure 2.5 illustrates the described workflow.

Draw waterbody centerline and a 1 m buffer polygon around it in ArcGIS

Clip C1 and C2 lidar points from inside the polygon

Build virtual WSM with Python script by calculating elevation of lidar points inside 2 m bins and extending this elevation in a direction perpendicular to the centerline for each bin with 1 m increment
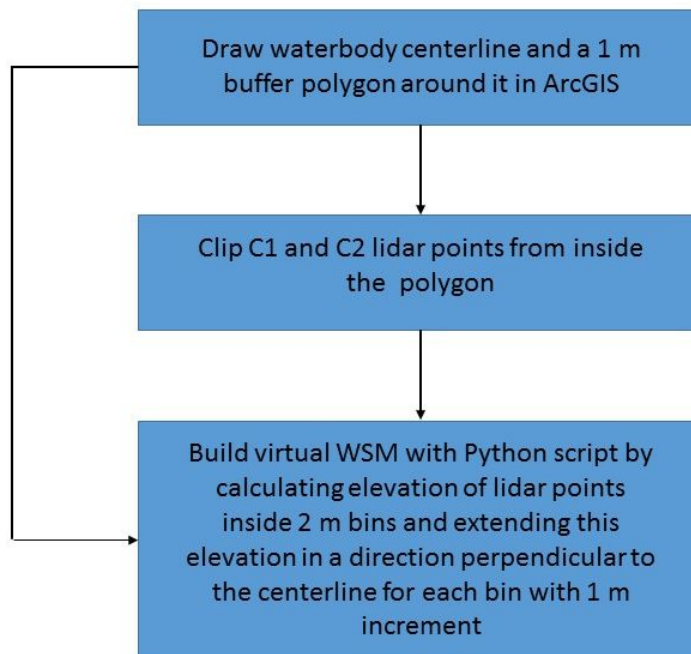
Figure 2.5 Virtual WSM workflow diagram.

24

For verification of the virtual WSMs, an 80 m by 560 m polygon for the Bow River AOI was selected and water surface points were classified visually by an operator; then, RMSE with *in situ* models was calculated.

2.3.2   *Assessment of water surface elevation uniformity within stream cross sections*

Virtual WSM is based on the assumption of water surface elevation uniformity within stream cross-sections. To check this assumption, two lines - left line (LL) and right line (RL) - approximately 1 m from the left and right banks of the Bow River were drawn inside the AOI based on the available hydrology polygon. Then transect lines from the step three in Figure 2.5 were used to intercept LL and RL. For points of interception, elevation was calculated by repeating the workflow on the diagram in Figure 2.5. Then residuals of elevation to the centerline (from the step one in Figure 2.5) for both LL and RL were calculated and output in a graph together with centerline elevation along the river.

2.3.3   *Bathymetric correction*

In situ bathymetric correction described in section 2.1.2 with scaling coefficient 0.763 was applied toward all points below virtual WSM. For verification, *in situ* correction was compared to the LMS bathymetric correction over a 130 m by 120 m polygon in the Bow River AOI. The polygon was chosen based on a minimal number of artifacts from the LMS correction. The ground classification algorithm from TerraScan (Terrasolid Ltd., Finland) software (Axelsson, 1999) was run over both point clouds and results were gridded using minimum value with LAStools (Isenburg, 2016) in 1 m raster files. Consequently, DTM maps, hillshaded DTM maps, and a

residual map were output and areas with obvious differences were visually compared in the TerrasScan viewer.

2.3.4   Depth performance and classification of the bottom returns

To assess depth performance of the system, height frequency distributions of the depth of C3 channel returns classified as water were output. All C3 returns below the WSM were classified as water, corrected via the bathymetric correction, and depth was calculated as a normal distance from each return to the WSM. To compare the depth performance with the one predicted by Equation 2.1, available turbidity data and the empirical model from Davies-Colley and Nagels (2008) to estimate K_d based on turbidity values were used.

A final step for preparing data for analyzing riverbed morphology would be a classification between water surface, volumetric, and riverbed returns, in order to utilize only last ones for creating riverbed DTM-W. The development of a complete classification is beyond the scope of the current study, and a workaround methodology was created by analyzing and utilizing double returns from the C3 channel within river boundaries. By filtering only double returns which are 50 cm below WSM, it can be ensured that second returns belong to the river bed while first returns are either volumetric or from the air/water boundary.

2.4   Results and Discussion

2.4.1   *Verification of the Virtual Water Surface Model*

WSMs of the Bow and Elbow rivers inside both AOIs are presented in

Figure 2.6 (a and b). A transect cut in Figure 2.6c illustrates the model and its use for

the classification – e.g. all points below the model can be classified as water. In the

illustration of the transect cut, the model produces visibly reasonable results in a

complicated area with the overhanging powerline. Verification of the virtual WSM

with manually derived model resulted in a RMSE of 0.05 m.

The advantage of the proposed method is in its flexibility to incorporate

additional inputs after pre-processing and relative simplicity (i.e. an additional

radiometric analysis is not required). The extension of the model in areas without

near-infrared returns (C1 and C2 in case of the Titan sensor) is simple and does not

require additional analysis. A disadvantage of the method is in the extra non-

automated steps, and a requirement of some a priori information (i.e. local hydrology

feature data in the case study). However, the method may be further developed

toward complete automation by incorporating radiometric methods, such as (Morsy

et al., 2016) or by developing more complex spatial algorithms.
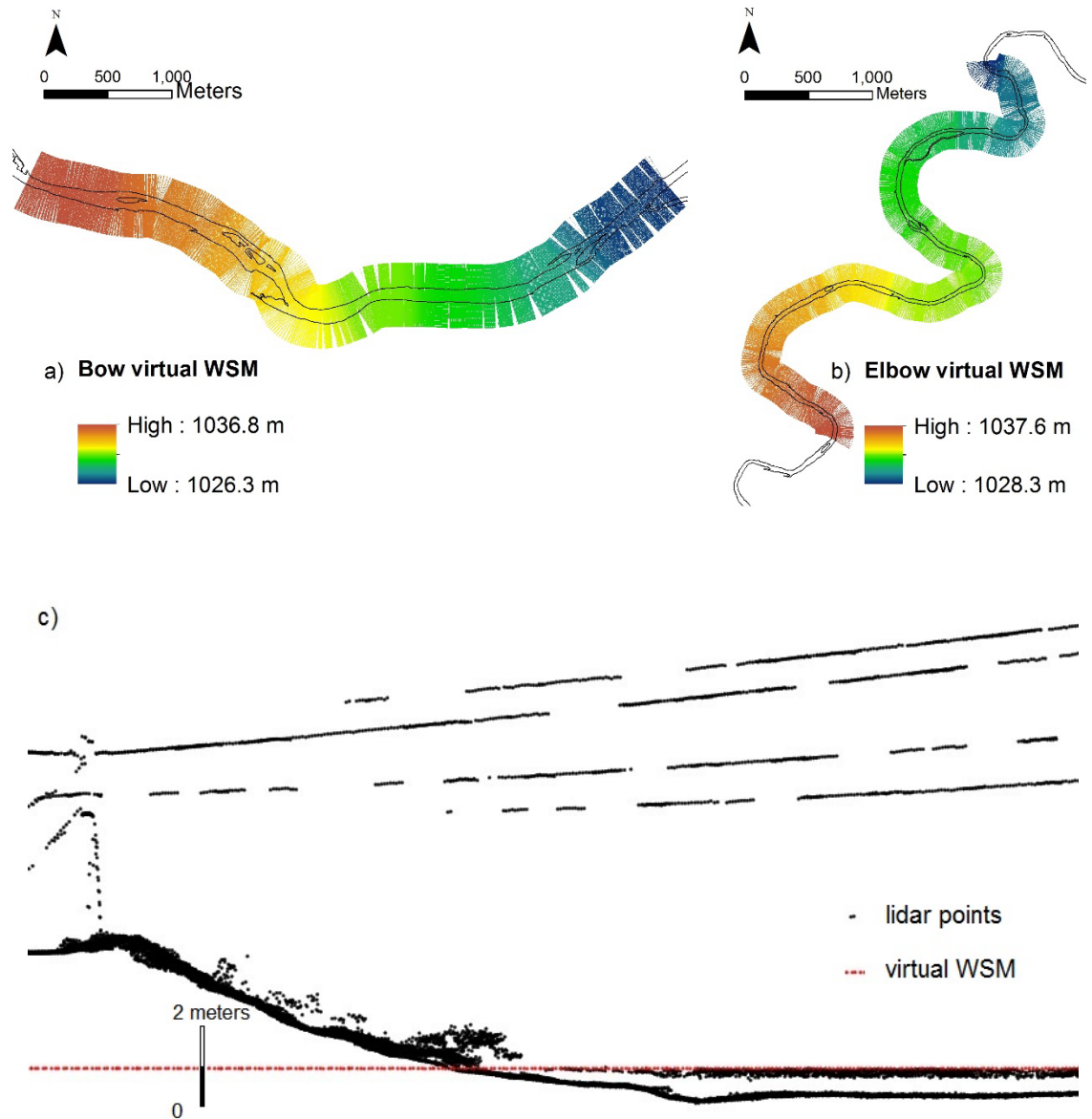
Figure 2.6 Virtual WSMs. a) - The Bow River; b) the Elbow River. c) - Illustration of a transect cut across the Bow River with virtual WSM depicted in red.

2.4.2 Assessment of water surface elevation uniformity within stream cross sections

The Bow River centerline water surface elevation , combined with the left side

and right side residuals to the centerline in Figure 2.7 shows residuals less than 5 cm

over half of the AOI, thus, confirming viability of assuming flat water surface across a

transect. However, there are three areas where residuals reach 20 cm, 40 cm, and 80 cm. These three areas on the graph coincide with areas where the river splits into two (or more) channels bypassing an island. The spatial distribution of water surface elevation in these areas is presented in Figure 2.8.
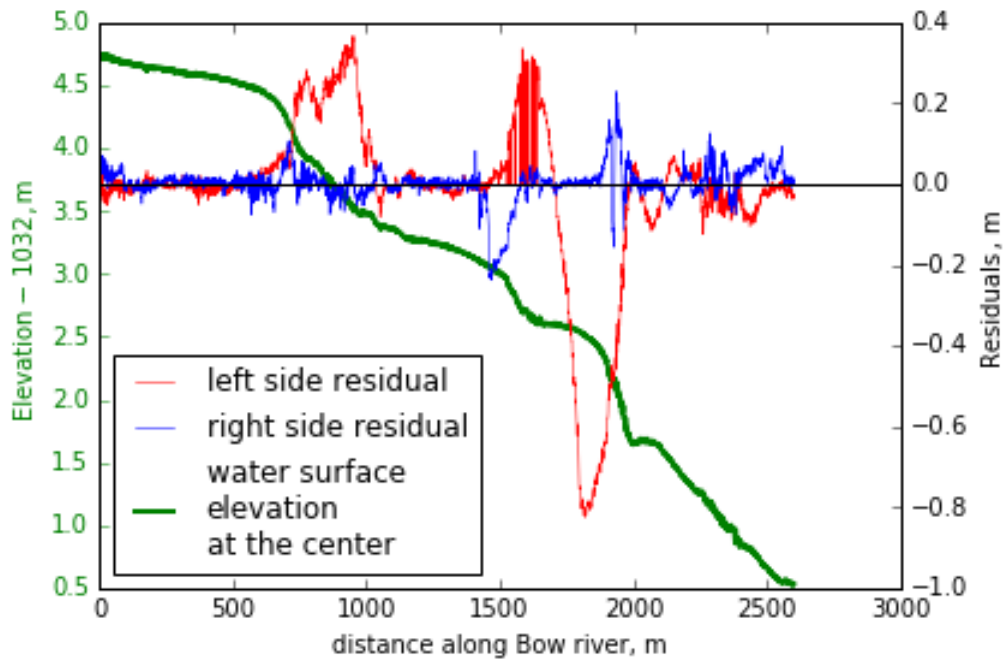
Figure 2.7 The water surface elevation of the Bow River with the left and right residuals from the left and right side of the river.

Note, that the centerline used in the analysis was digitized based on the spatial center of the water boundary polygon but not based on riverbed morphology (centerline in Figures 2.8). Thus, the gradient line on the graph in Figure 2.7 might be misleading in the areas exactly where the islands are and the main water flow may deviate toward the left or right side on the graph.
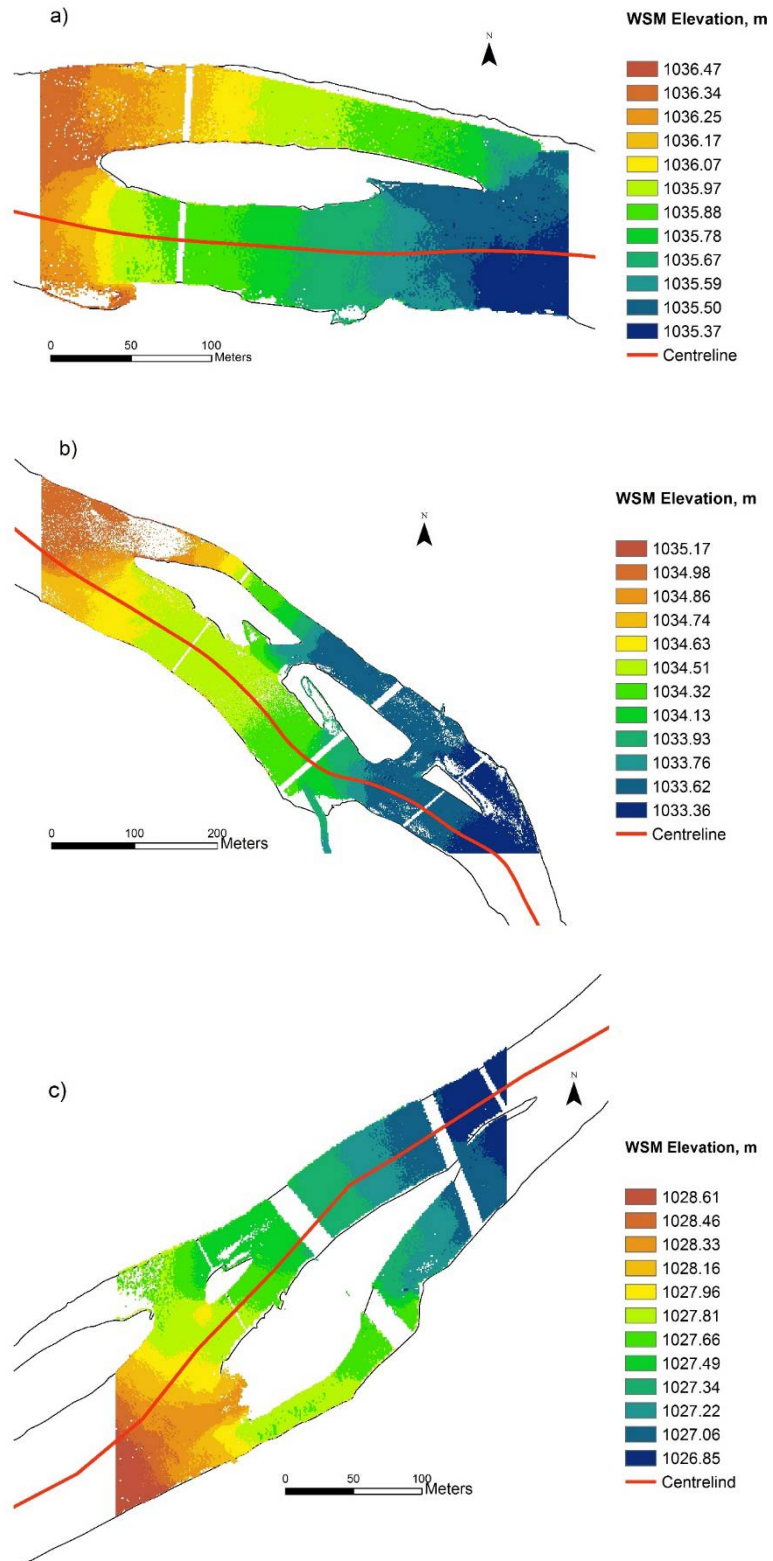
Figure 2.8 Spatial distribution of the water surface elevation at three areas along three islands in the Bow River. Centreline used for calculations depicted by red line.

All three areas in Figure 2.*8* show a *complex distribution of the water surface*

elevation *and il*lustrate residuals in Figure 2.7. Different water levels have already

been reported by Hopkinson, Crasto, Marsh, Forbes, and Lesack (2011) but on a

completely different scale of the Mackenzie Delta. A clear outcome from this

assessment is that extending flat water surfaces across small mid-channel islands is

not a viable approach for bathymetric correction in dynamic river environments.

2.4.3   *In Situ bathymetric correction*

In situ bathymetric correction was applied to both AOIs. Examples of the

obtained DTM-W and water depth (D_{water}) for an area coincident with the area in

Figure 2.8a are presented in Figures 2.9a and 2.9b. In this area, maximum water

penetration depth for the Titan sensor was 1.77 m. The DTM-W enables interpretation

of causes for different water elevation in two channels in Figure 2.8a. From the DTM-

W it is evident that in the case of this island – it features 30-40 cm positive difference

in the left residual in Figure 2.7 (direction is following the stream) – the left river

channel has a higher bed elevation in the first part in comparison to the right river

channel. This at least partially explains the observed difference in water surface

elevation.
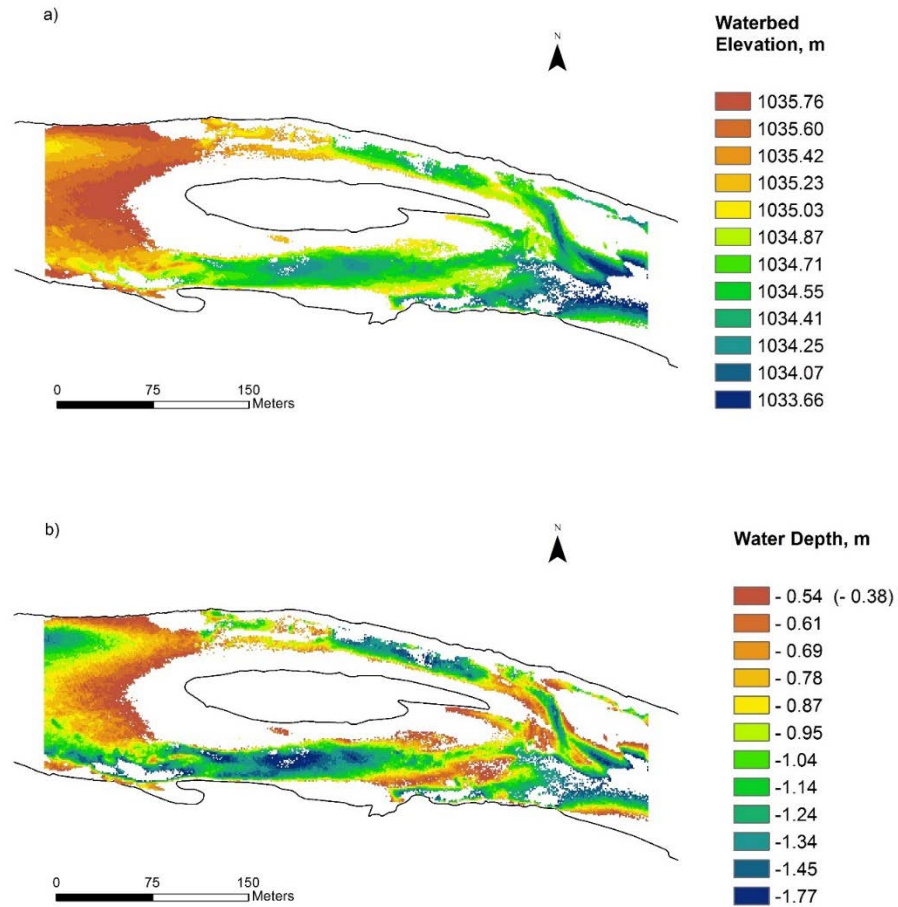
Figure 2.9 a) – DTM-W (lidar returns from C3 channel with a cut of 0.5 m below WSM to remove volumetric returns). b) - Water depth.

Results of the verification with the LMS bathymetric correction are shown in

Figure 2.10. Hillshade surfaces in Figure 2.10a and 2.10b show that while the *in situ*

correction is smoother, the LMS correction produces some artifacts, which are

illustrated in Figure 2.10e where the residual difference is >20 cm. Visual cross-section

comparisons from two datasets in TerraScan (screengrabs in Figures 2.11) shows that

in situ correction is very close to the LMS correction; however, in some areas the LMS

routine omitted bottom returns during correction and at other places it corrected

points by shifting them deeper or by creating two layers of bottom points where the

lower layer seems to be uncorrected.

a) LMS correction, hillshade surface   b) In situ correction, hillshade surface
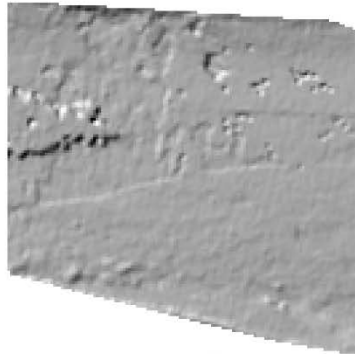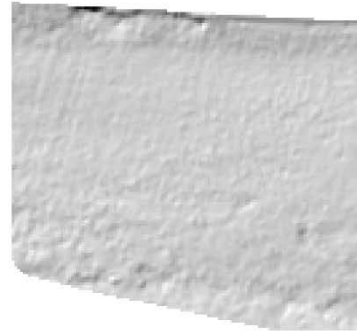
c) LMS correction, depth   d) In situ correction, depth
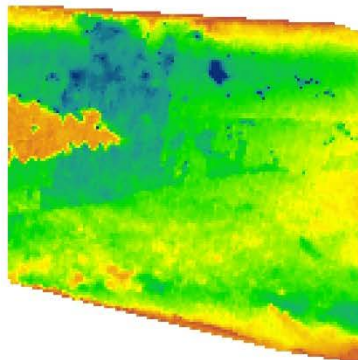
0 m

-2.0 m

e) Residuals

Residuals, m

	-1.0 - -0.5
	-0.5 - -0.3
	-0.3 - -0.2
	-0.2 - -0.1
	-0.1 - 0
	0 - 0.1
	0.1 - 0.2
	0.2 - 0.3
	0.3 - 0.5
	0.5 - 0.7
	0.7 - 0.9
	0.9 - 1.3

N

Meters

0   50   100
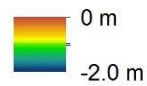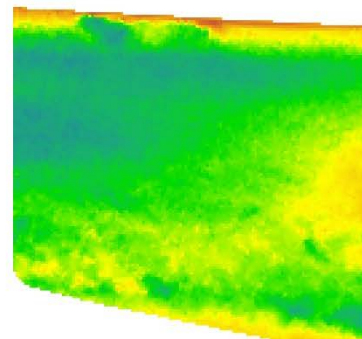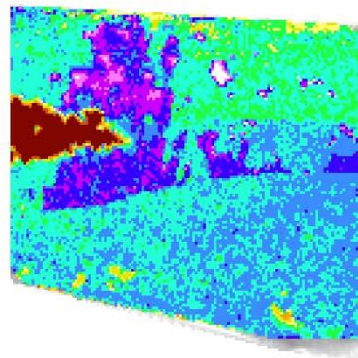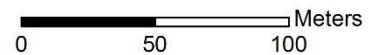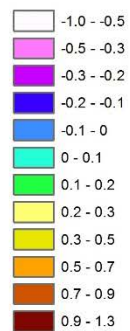
Figure 2.10 Hillshade raster maps of two bathymetric corrections – LMS on the left
and *in-situ* on the right – with residuals below.

33

a)
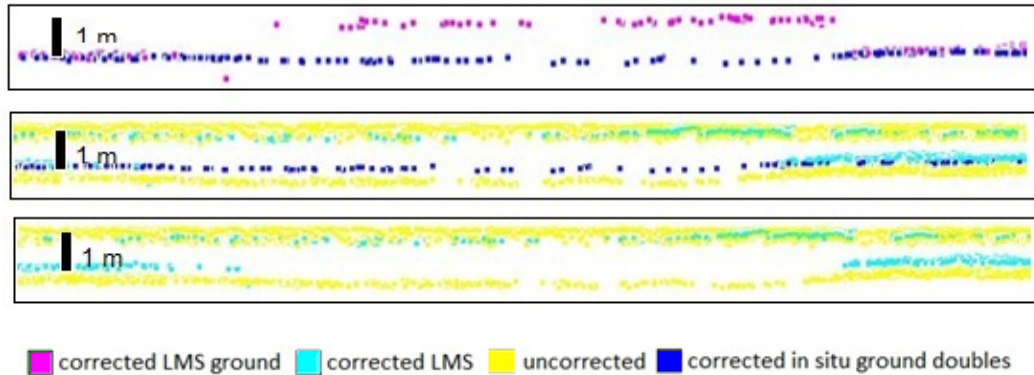
b)
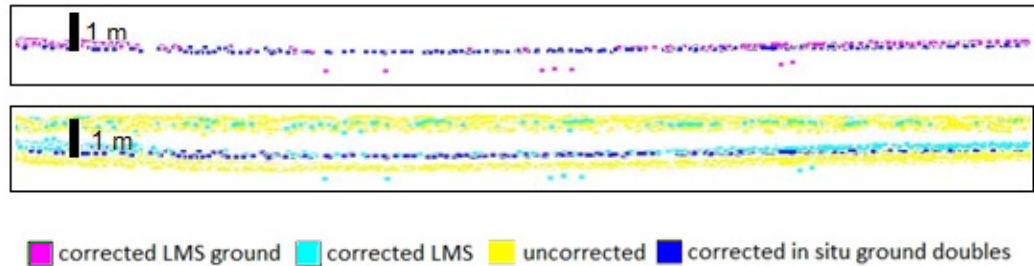
c)
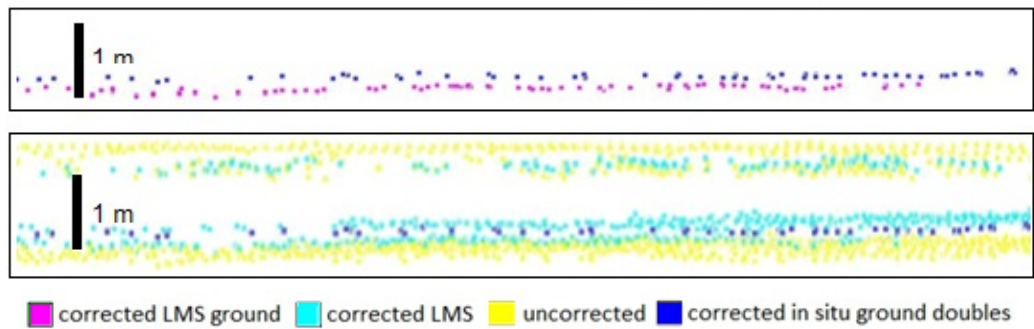
Figure 2.11 a) - An area with LMS corrections 1 m above *in situ* correction. It is clear, that LMS omitted some bottom returns. b) – An area with LMS correction below *in situ* correction. It is clear, that LMS moved some points deeper than most of the points. c) - An area with LMS correction below *in situ* correction. It is clear, that LMS split its correction in two layers. In situ correction lays in-between these layers.

Comparison of the *in situ* correction with the one from LMS suggests that the results of the *in situ* correction are more favorable. The key component of the *in situ* correction is an adequate WSM to initiate the bathymetric correction step. This

comparison shows the potential of the *in situ* approach for quality assurance. Two

surfaces can be created similar to the *in situ* correction with scaling coefficients

corresponding to the minimum and maximum angles of incidence (for instance, 0.75

and 0.80 for the range between 0 and 30 degrees in Figure 2.2) and OTS bathymetric

correction can be tested to be located in-between these two surfaces.

However, it must be noted, that a bathymetric correction, based on the

assumption of a simple flat water surface may bring inaccuracy of the same

magnitude as was estimated by Equations 2.3 and 2.4 (Westfeld, Richter, Maas, &

Weiss, 2016). Westfeld et al. (2016) reported elevation displacement between 0.7%

and 4.7% of water depth and dXY displacement between 4.0% and 15.8% of water

depth depending on the type of wave patterns used within their ray tracing modeling

experiment. Although the simulation was done for ocean waves, the beam

divergence used in modeling was rather large and the authors predicted that with a

smaller footprint the effect will increase. Thus, in order to achieve the highest

accuracy, an algorithm must account not only for the trajectory and angles of

incidence but also for roughness of the water surface, which inevitably makes the

corresponding correction complicated. Such complexity might be another reason for

advocating for a simplified bathymetric correction based only on water column depth

and disregarding angles of incidence as the first iteration with lower accuracy if the

latter is acceptable for practical purposes.

2.4.4 Depth performance and volumetric returns

Depth performance of the system was estimated from the D_{water} frequency distribution of C3 channel returns classified as water. Depth frequency distribution for double returns and single returns for AOIs of the Bow River and the Elbow River are presented in Figures 2.12. Histograms in Figure 2.12 show good penetration of the green laser for up to 1.5 m below the water surface. Only a few returns penetrated up to 1.8 m but not deeper than this threshold.
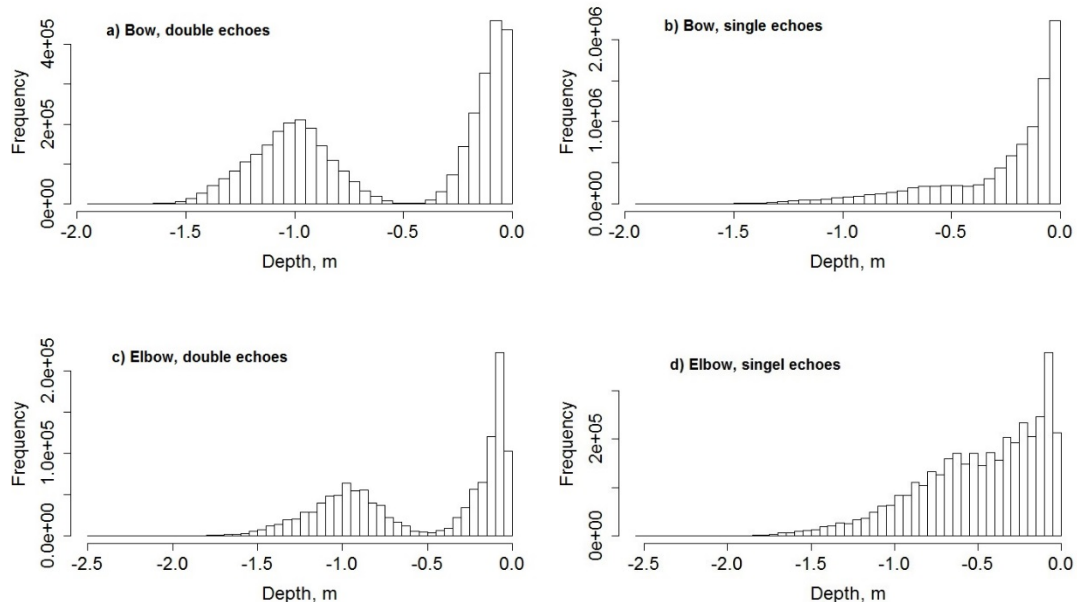
Figure 2.12 Depth frequency distribution histograms for both AOIs. a) – double echoes from the Bow River. b) – single echoes from the Bow River. c) – double echoes from the Elbow River. d) – single echoes from the Elbow River.

Turbidity data, measured in nephelometric turbidity units (NTU) in Table 2.1 show low values (2-3 NTU) for a point at the Bow River (downstream from the Bearspaw Dam) which is 9 km upstream of the Bow River AOI (Figure 2.4), but high values (27-39 NTU) at a station 30 km downstream of the AOI. The Elbow River

measurements were taken upstream of the Glenmore Reservoir and therefore

provide no direct information about the actual turbidity of the Elbow River

downstream of the reservoir. The Elbow station data shows rather high values of

turbidity (18-30 NTU) during the flight period.

Table 2.1 Turbidity data received from the City of Calgary municipality for the time of the survey.

		Bow @		Elbow @
		Bearspaw Raw 2	Stier's Ranch	City Limits
Date (yyyy/mm/dd)	Time	Turbidity (NTU)	Turbidity (NTU)	Turbidity (NTU)
2016/08/09	0:00:00	3.3	39.6	30.29
2016/08/09	0:15:00	3.2	38.8	29.33
2016/08/09	0:30:00	3.2	37.2	27.07
2016/08/09	0:45:00	3.2	36.4	23.96
2016/08/09	1:00:00	3.1	35.5	24.23
2016/08/09	1:15:00	3.1	34.3	23.6
2016/08/09	1:30:00	3.0	33.3	22.62
2016/08/09	1:45:00	3.1	31.6	21.83
2016/08/09	2:00:00	3.0	30.0	21.72
2016/08/09	2:15:00	3.1	28.9	20.19
2016/08/09	2:30:00	2.9	28.2	19.1
2016/08/09	2:45:00	2.9	27.0	18.5

Based on Davies-Colley and Nagels (2008) model, K_d corresponding to

turbidity values (2.8-3.3 NTU) measured in an upstream station during the survey time

was estimated as 0.8-1.2 m^{-1} . Subsequently, from Equation 2.1, depth performance for

Titan sensor was calculated as 1.2-1.8 meters below the water surface which is close

to the threshold value derived from the histograms in Figures 2.12. Although it should

be noted, that the turbidity data for the model were collected upstream of the AOI

and may not represent the conditions sampled by Titan.

A more reliable method of estimating depth performance before a bathymetric lidar survey is needed. A recently reported algorithm (Dogliotti, Ruddick, Nechad, Doxaran, & Knaeps, 2015) that allows retrieving turbidity values from satellite imagery combined with more precise models of deriving values of the diffuse light attenuation coefficient (K_d) from nephelometric turbidity may be a key for tackling this problem.

Histograms in Figures 2.12 also allow for a first simple analysis of volumetric returns. Depth frequency distribution of volumetric returns on the double-returns graphs in Figure 2.12 (a and c) is evident in the form of the first peak; a distinct gap between the first and second peaks is explained by "dead" detection time between the registration of the first pulse and the second pulse. The same peak exists in the single-returns graphs and may also be associated with volumetric returns. The shape of the peak of the double-returns graphs reconciles the visual exploration of the dataset in which it was found that volumetric returns do not exist below 60 cm from the water surface in the study area. This observation coincides with the results reported in (Mandlburger et al., 2013).

Although it is widely accepted that volumetric returns are due to the water turbidity (G. C. Guenther et al., 2000; Mandlburger et al., 2013), one element of the dataset attracts attention in this sense - the areas lacking surface return points from the C1 and C2 channels in the Elbow River (Figure 2.13). A visual exploration of the C3 channel returns (Figure 2.13) shows that it also lacks surface and volumetric returns in these areas; however, there are many bottom returns. If the volumetric explanation

is correct, volumetric returns should be seen in these areas together with bottom

returns. If turbidity would be the only factor for the explanation of volumetric

returns, it would be difficult to accept that in the case of these areas turbidity

changed dramatically over 20 meters and then changed back in another 100 meters.
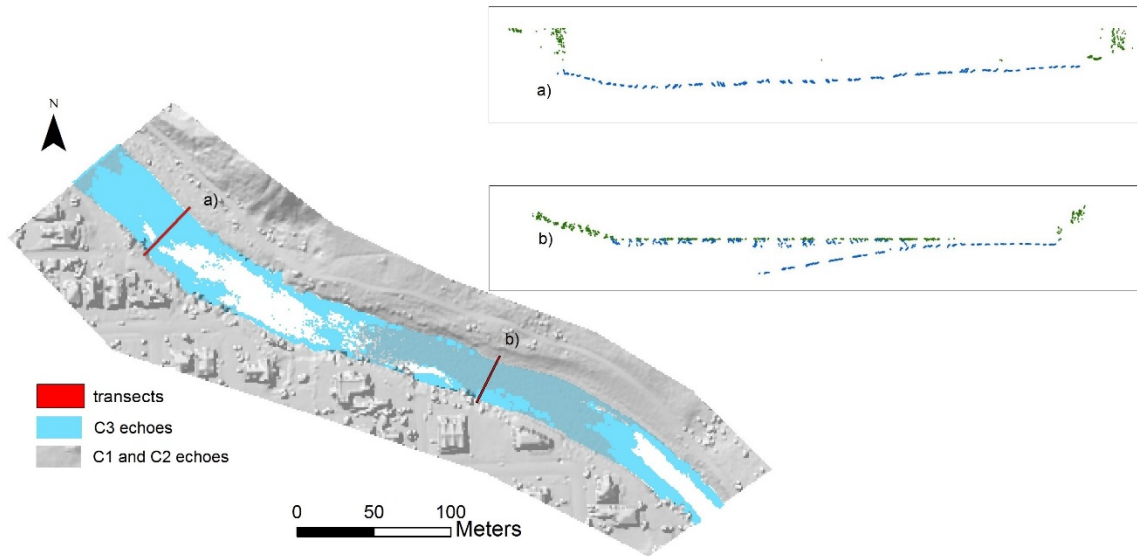
Figure 2.13 Section of the Elbow River. Transect a) shows no volumetric returns from C3 (blue) and no surface returns from C1 and C2 (green). Transect b) shows volumetric returns from C3 and surface returns from C1 and C2.

2.5   Conclusions

In this chapter, a simplified algorithm for an *in situ* bathymetric correction of

lidar returns has been presented which provided favorable results in comparison to a

proprietary software routine. Relative to contemporary proprietary OTS solution, the

in situ method presented has the potential to sacrifice absolute accuracy in some

situations. However, the benefit is a routine that can be employed by an end user

with access to typical data and software resources to produce a realistic river bed

morphology with fewer artifacts. A quality assurance application of the proposed *in situ* correction was also briefly discussed. Method of deriving a WSM from multi-spectral lidar data was described providing the key component for the *in situ* bathymetric correction. Water surface variations of up to 80 cm across two channels of the river around a small island in the Bow River AOI were observed showing that extending flat water surfaces across small mid-channel islands is not a viable approach for bathymetric correction in dynamic river environments. Thus, this study provides further evidence that lidar is as a valuable instrument for mapping water surfaces and creating DTM-W for hydraulic and hydrodynamic analyses.

Maximum water penetration was assessed and showed good correspondence with the depth performance prediction based on turbidity measurements and the system specification. There remains the problem of classification of the green C3 channel water returns into three categories – surface, volumetric, and river bed, as this was only briefly addressed. Finally, a potential method of predicting depth performance of bathymetric lidar –information much needed by industry and other stakeholders – which would include the employment of passive imagery and optical water quality variables was outlined.

Future work will include data fusion with passive imagery to aid prediction of depth performance of the system and to distinguish volumetric returns from river bed returns, which also may provide a way of extrapolating lidar-derived bathymetry to areas lacking lidar returns. Bathymetry belongs to the domain of complicated remote sensing tasks and different approaches may add to each other and create a

synergy effect. Multi-spectral lidar, combined with hyperspectral/RGB camera and a full waveform digitizer for a green channel provides a large amount of information in general and in a bathymetric context in particular. It is clear that more advanced algorithms will be developed potentially based on Bayesian networks or machine learning approaches, combined with an intensive usage of known *a priori* information, such as contemporary regional hydrology GIS data layers.

3   Investigating consistency of uncalibrated Titan spectral vegetation indices at different altitudes

Abstract

Multi-spectral (ms) airborne lidar data are increasingly used for mapping and change monitoring. Geometric data are enriched by intensity digital numbers (DNs) and, by utilizing this additional information either directly, or in the form of active Spectral Vegetation Indices (SVIs), enhancements in classification and change monitoring are possible. In the case of SVIs, the indices should be calculated from reflectance values derived from intensity DNs after rigorous calibration. In practice, such calibration is often not possible, and SVIs calculated from intensity DNs are used. However, the consistency of such active ms lidar products is poorly understood. Here, we report on an ms lidar mission carried out in July 2016 at three different altitudes above ground to investigate this problem. The need for atmospheric correction in case of considerable range difference is established. The consistency of SVIs derived from intensity DNs through a variety of altitudes was investigated, and it was demonstrated that by filtering only single echoes it is possible to derive stable SVI products. The stability of two families of indices – spectral ratios and normalized differences – was compared. Finally, a criterion is proposed for comparing different lidar acquisitions over vegetated areas.

3.1 Introduction

Light Detection and Ranging (lidar) established itself as a unique high-resolution remote sensing technology due to its 3D sampling of land cover and terrain, and its ability to penetrate into and characterize vegetation structure from treetop to ground (Vosselman & Maas, 2010). Lidar is primarily used to construct detailed digital elevation models (DEMs), but the intensity channel (an index of signal reflectance) is increasingly used in a similar fashion to black and white aerial photographs or single channels in multispectral imagery. Using passive imagery, numerous SVIs have been developed based on reflectance values derived from image-based DNs for environmental monitoring and change detection (Lu, Mausel, Brondizio, & Moran, 2004; Lyon, Yuan, Lunetta, & Elvidge, 1998; Pettorelli, 2013). Modern multi-spectral lidar technology allows for active narrow-band vertical spectral sampling of vegetation profiles and provides an alternative method of deriving SVI maps - active SVI, therefore, presenting a new tool for high resolution thematic mapping, enhanced classification and change detection, and forest resource monitoring (Hopkinson et al., 2016).

In general, the main limitation of using spectral vegetation indices derived from passive remote sensing is in the dependence of passive imagery on the sun as a source of illumination (Baret & Guyot, 1991), which leads to sensitivity of passive SVIs to sun position (Huete, 1987) and cloudiness (Jackson, Slater, & Pinter, 1983). In addition, passive SVIs as quantitative indicators of vegetation phenology characteristics are also affected by canopy structural properties, background scene,

and leaf surface, shape, and orientation (Zhang, Chen, Miller, & Noland, 2008). The benefit of lidar, as an active sensor that measures the backscatter signal, is in its ability to collect data without an external source of illumination and in its potential to eliminate multiple scattering and geometric viewing effects (Gaulton, Danson, Ramirez, & Gunawan, 2013; Morsdorf et al., 2009). Additionally, for a small-footprint system, background radiance can be easily separated from the canopy response. The main factors affecting lidar backscatter, besides the spectral reflectance properties of the target, are the area of effective backscattering surface and the local incidence angle of the target (Gaulton et al., 2013). However, if the optical path at different wavelength channels is similar, like in the sensors described by Hakala, Nevalainen, Kaasalainen, and Makipaa (2015) and Morsdorf et al. (2009), or close to each other, like in the Titan ms lidar, one can assume that the influence of these factors is reduced or potentially canceled in active SVI. Consequently, to maximize the utility and comparability of active SVIs, it is necessary to study their consistency through different sensors and/or different survey configurations.

3.1.1   The Titan Spectral Vegetation Indices

In general, if there are a number of spectral bands of some particular sensor, we can construct, following Rees (2004), two types of indices – the simple ratio index ($s\rho$) and the normalized difference index ($n\delta$) by the following mathematical expressions:

$$s\rho_m^l = \frac{\rho^l}{\rho^m} \quad , \qquad\qquad\qquad \text{Equation 3.1}$$

$$n\delta_m^l = \frac{\rho^l - \rho^m}{\rho^l + \rho^m} \quad . \qquad\qquad\qquad \text{Equation 3.2}$$

Here ρ^l and ρ^m denote *spectral reflectance of the target (or scene) at the l_{th} and m_{th} channel/band. There is an obvious non-linear relation between these two indices* (Perry & Lautenschlager, 1984)*:*

$$n\delta_m^l = \frac{s\rho_m^l - 1}{s\rho_m^l + 1} \quad . \qquad\qquad\qquad \text{Equation 3.3}$$

The first SVIs where introduced as a result of an effort to reduce multispectral measurements of Landsat I to a single value (Perry & Lautenschlager, 1984; Rouse Jr, Haas, Schell, & Deering, 1974) and inevitably referred to the available Landsat spectral bands. Following the same logic, we can limit our interest in SVIs to the particular wavelengths of 532nm, 1064nm, and 1550nm, which are available in the Teledyne Optech Titan sensors as channels C3, C2, and C1 – a brief description of the system can be found in Chapter I of this thesis. Thus, we can construct six $s\rho$ indices and correspondingly six $n\delta$ indices. However, due to symmetry:

$$s\rho_m^l = \frac{1}{s\rho_l^m} \quad , \text{ and} \qquad\qquad\qquad \text{Equation 3.4}$$

$$n\delta_m^l = -n\delta_l^m \quad . \qquad\qquad\qquad \text{Equation 3.5}$$

We will consider only three *spectral ratio indices and three normalized difference indices* which we will refer to as $s\rho(C_l,C_m)$ and $n\delta(C_l,C_m)$ with l, m indices corresponding to Titan`s channel numbers or, for indicating the actual wavelengths, as $s\rho_{\lambda_m}^{\lambda_l}$ and $n\delta_{\lambda_m}^{\lambda_l}$.

In passive imagery, the abbreviation NDVI (Normalized Difference Vegetation Index) is reserved for the particular band combination, i.e., red and near-infrared (NIR) bands (Pettorelli, 2013). This index helps to distinguish vegetated areas on an image due to the way light reflects from vegetation. Spectral signatures of green vegetation are well known (Gates, Keegan, Schleter, & Weidner, 1965) and a generic curve is presented in Figure 3.1. Spectral reflectance is low in the visible range, with a peak in the green region. This is due to absorption of light by chlorophyll and other pigments in leaf tissue. The following sharp increase in the spectral reflectance curve is referred to as the red edge. After the red edge, there is a region of relatively high reflectance known as the NIR plateau. The leaf cell structure dominates the response in this region. After NIR plateau, there are two regions of lower reflectance around 1450 nm and 1950nm due to absorption by water in the leaf tissue, with a region of increased reflectance in-between.
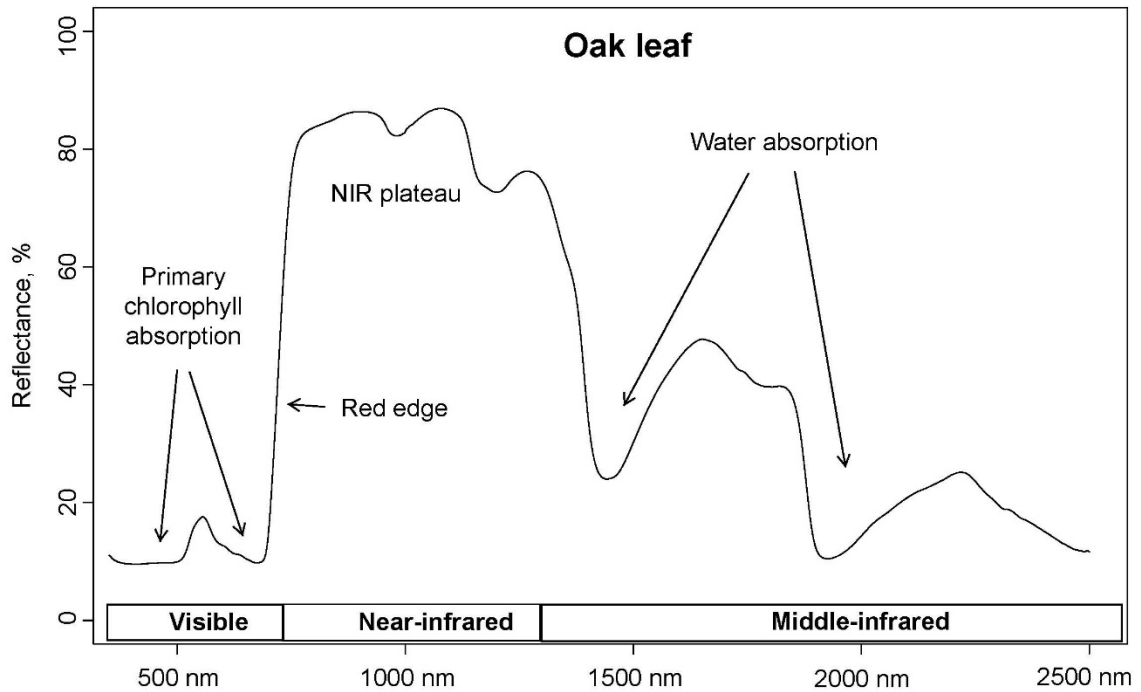
Figure 3.1 Typical leaf reflectance curve between 350 nm and 2500 nm. Spectral reflectance data for the figure were retrieved from USGS Spectral Library (R.F. Kokaly et al., 2017b).

As we see in Figure 3.1, it is possible to distinguish vegetated and non-vegetated areas by using NDVI by adopting a broader definition, as the normalized difference in reflectance between NIR and any of the visible bands. For example, the NOAA AVHRR (Advanced Very High-Resolution Radiometer) sensor has only one band for the visible spectrum. Using this approach, Titan`s $n\delta_{532\,nm}^{1064\,nm}$ index is comparable to a commonly defined and utilised NDVI. Moreover, in narrow-band hyperspectral passive imagery, another index - PRI (Photochemical Reflectance Index) - was developed for assessing the canopy photosynthetic light use efficiency of vegetation (Gamon, Serrano, & Surfus, 1997). This index is based on a change in canopy reflectance at 531 nm with interconversion of the xanthophyll cycle pigments, a

process which is closely linked to light absorption. Currently, the most commonly used definition of PRI is the normalized difference between the 531 nm and the 570 nm wavebands, with the latter being used as a reference. However, in the original work (Gamon, Penuelas, & Field, 1992) Gamon et al. introduced PRI as, using our notation, $n\delta_{ref}^{531\,nm}$ and, assuming that reflectance of the canopy at 1064 nm does not change with overexposure to light, we may expect from Titan`s $n\delta(C2, C3)$ properties comparable to PRI.

For passive imagery it has been shown that the Normalized Difference Infrared Index (NDII), which utilized near-infrared (0.7 - 1.3 μm) and middle-infrared (MIR, 1.3 - 2.5 μm) wavelengths, is highly correlated with canopy water content (Hardisky, Klemas, & Smart, 1983) and was applied for the detection of plant water stress (Hunt & Rock, 1989). In a recent study, Hancock et al. (2017), investigated angular reflectance of leaves with a dual-wavelength terrestrial lidar system and its implications for leaf-bark separation and leaf moisture estimation, and showed that change in the Normalized Difference Index (NDI , at 1063 nm and 1545 nm) associated with leaf water content was larger than the change related to the angle of incidence. In our notation, this index is close to Titan`s $n\delta_{1550\,nm}^{1064\,nm}$. In addition, Chasmer et al. (Chasmer, Hopkinson, Petrone, & Sitar, 2017) used active normalized burn ratio (ANBR) derived from ms lidar utilizing 1064 nm and 1550 nm channels for assessing burn severity in vegetated areas and compared obtained ANBR to normalized burn ratio derived from Landsat data.

Finally, the normalized difference of the green band and MIR was used by Xu

(2006) for distinguishing water bodies from the soil, vegetation, and man-made

features. In a recent study, Morsy et al. (2016) suggested using Titan`s NDVI$_{NIR-G}$

($n\delta_{532\,nm}^{1550\,nm}$) for vegetation extraction. It is yet to be found what this index indicates in

the canopy.

3.1.2   Lidar radiometry

Radiometry characterizes or measures how much electromagnetic energy is

associated with some location or direction in space (Schott, 2007). In case of lidar this

is the target`s intensity response to the emitted laser pulse. The relationship between

transmitted and received laser pulse power in the far field is given by the radar

equation in the form of (Jelalian, 1992):

$$P_r = P_t \frac{D^2}{4\,R^2} \frac{\sigma}{4\theta_t^2 R^2} \mu_{atm}\mu_{sys} \quad , \qquad \text{Equation 3.6}$$

where:

P_r – received signal power, μ_{atm} – atmospheric transmission factor,

P_t – transmitted power, μ_{sys} – system transmission factor,

D – aperture diameter, θ_t – transmitter beam width, and

R – system range to target, σ – effective target cross section.

The effective target cross section is defined as:

$$\sigma = \frac{4\,\pi}{\Omega}\,\rho_t\,\partial A \quad , \qquad \text{Equation 3.7}$$

where

Ω – scattering steradian solid angle of target, ∂A – target area, and

ρ_t – target reflectivity.

Assuming a standard scattering diffuse target (Lambertian target), equation 3.7 can

be re-written:

$$\sigma = 4\,\rho_t\,\partial A \quad .$$
<div align="right">Equation 3.8</div>

The area A_{fp}, illuminated by a circular beam at a range R at nadir, is:

$$A_{fp} = \frac{\pi\,R^2\,\theta_t^2}{4} \quad .$$
<div align="right">Equation 3.9</div>

Note, that beam divergence θ_t is provided for only a part of the spatial energy beam

profile (e.g., Gaussian at 1/e or 1/e²); therefore, A_{fp} only approximates the total

illuminated area. If a target intercepts the entire beam, it is referred to as an

extended target. If the target area is smaller than the transmitted footprint, it is

referred to as a point target. Thus, for an extended Lambertian target substituting ∂A

with A_{fp}:

$$\sigma_{ext} = \pi\,\rho_t\,R^2\,\theta_t^2 \quad ,$$
<div align="right">Equation 3.10</div>

leading to the radar equation in the form:

$$P_r = P_t\,\frac{\pi\,D^2}{16\,R^2}\rho_t\,\mu_{atm}\mu_{sys} \quad .$$
<div align="right">Equation 3.11</div>

For a point target, the radar equation can be re-written in the form:

$$P_r = P_t\,\frac{\pi\,D^2}{16\,R^2}\,\frac{4\,\partial A}{\pi\,\theta_t^2 R^2}\,\rho_t\,\mu_{atm}\mu_{sys} \quad .$$
<div align="right">Equation 3.12</div>

In discrete return systems it is often assumed that the recorded intensity DN is linearly dependent on the peak of the received power (Baltsavias, 1999a; Hopkinson, 2007).

3.1.3   Lidar intensity metrics

The intensity of the small-footprint systems has been shown to be useful in land cover classification (Yan, Shaker, & El-Ashmawy, 2015), tree species classification (Korpela, Tuomola, Tokola, & Dahlin, 2008), fractional cover estimation (Hopkinson & Chasmer, 2009), and carbon contained in forest biomass (Garcia, Riano, Chuvieco, & Danson, 2010). Although many studies have shown the utility of all returns (Holmgren & Persson, 2004; Hopkinson & Chasmer, 2009), some studies use the intensity of the first returns (Donoghue, Watt, Cox, & Wilson, 2007; Korpela et al., 2008). Korpela, Orka, Maltamo, Tokola, and Hyyppa (2010) explained that the choice of working with first returns was made because of insufficient point density of single returns in the study dataset. Usually, intensity metrics are calculated by averaging values in raster grids of a certain size, after range normalization, or, if possible, after rigorous calibration (Yan et al., 2012). The procedure of rasterization with assigned average value can be written for grids of extended targets, with an index i running through points inside a given cell:

$$< P_r^{ext} > = < P_t^i \frac{\pi\, D^2}{16\, R_i^2} \rho_t^i\, \mu_{atm}^i \mu_{sys}^i > \quad . \qquad \text{Equation 3.13}$$

Here we use notation $<x^i>$ to denote rasterization of an attribute x associated with a point from the lidar point cloud by averaging ($<>$) through i numbers of attribute

values from corresponding *i* points inside a grid cell. We can presume that intensity

DN (I) is a linear function of the received peak power ($I = k\,P_r$) and range

normalization to the range $\mathbb{R}$ was applied to intensity DNs. Then, assuming that

atmospheric losses, transmitter power, and the system factor are constant, we can

rewrite the above equation in the form of (denoting intensity normalized to inverse

square range as $\tilde{I}$):

$$< \tilde{I}_i^{ext} > = k\,P_t\,\frac{\pi\,D^2}{16\,\mathbb{R}^2} < \rho_t^i > \mu_{atm}\mu_{sys} \quad \cdot \qquad \text{Equation 3.14}$$

The same procedure can be done for point targets, and with the same assumptions

for each point target we can write:

$$< \tilde{I}_i^{pt} > = kP_t\,\frac{\pi\,D^2}{16\,\mathbb{R}^2} < \frac{4\,\partial A^i \rho_t^i}{\pi\,\theta_t^2 R_i^2} > \mu_{atm}\mu_{sys} \quad \cdot \qquad \text{Equation 3.15}$$

Or, if we use area A_{fp} (Equation 3.9) as a normalization value:

$$< \tilde{I}_i^{pt} > = kP_t\,\frac{\pi\,D^2}{16\,\mathbb{R}^2} < \frac{\partial A^i}{A_{fp}^i}\rho_t^i > \mu_{atm}\mu_{sys} \quad \cdot \qquad \text{Equation 3.16}$$

Interpretation of single returns intensity from an extended target is quite

straightforward, as it represents an average reflectance over the grid. However, in

the case of single returns from vegetation, this is generally not true. For a lidar beam,

vegetation represents a porous 3D target leading to a widening of the response echo

and, in effect, causes volumetric backscattering. The process can be described in

mathematical terms as a convolution of the emitted pulse with a differential effective

cross-section of each cluster of inseparable targets (Roncat, Morsdorf, Briese,

Wagner, & Pfeifer, 2014) and is illustrated on Figure 3.2b. Thus, the peak of the

intensity does not quantitatively correspond to the energy scattered by the particular

volume of the target with the same coefficient as in the case of a flat extended

target. However, assuming a Gaussian distribution along the beam propagation we

can calibrate such returns in FWF (Full Waveform) systems by utilizing the pulse

width information from the returned signal waveform (Wagner, Ullrich, Ducic,

Melzer, & Studnicka, 2006). In case of DR systems, this information is not available

and one can only assume similarity of volumetric echo widths. Moreover, in case of

FWF scanners, a response signal of the system to an emitted pulse is recorded, and it

was shown (Wagner et al., 2006) that this waveform is also a convolution (in time) of

the received signal with the detector response function (illustrated on Figure 3.2b).

The latter should be used for more accurate analysis of the lidar intensity DNs.
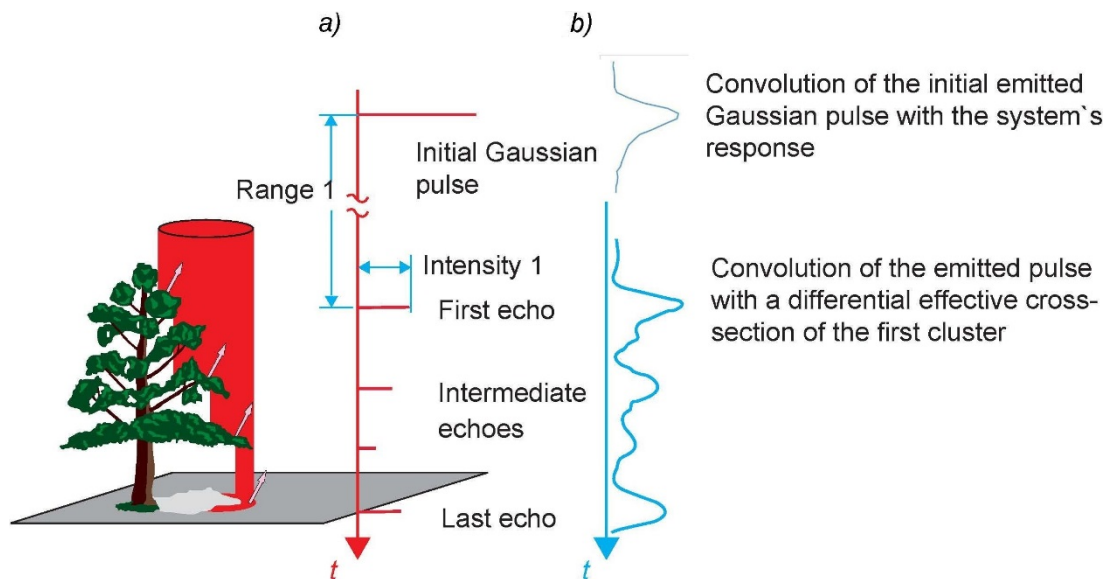
Figure 3.2 Multiple echoes and full waveforms: a) discrete returns; b) full waveform.
Image adopted from Vosselman and Maas (2010).

3.1.4 *Angular effects of lidar backscatter*

In Equation 3.7, we omitted explicit consideration of the angle between the surface of the target and the lidar beam, and lumped it into reflectance ρ by assuming the target is an ideal diffuse Lambertian reflector. This is a common approach in the interpretation of lidar backscatter, and a backscatter coefficient (Roncat et al., 2014; Wagner, 2010) is used to combine the Lambertian assumption with normalization of the lidar backscatter to the illuminated area. However, in general, the reflectance of a particular object is more complex and described by a corresponding bidirectional reflectance distribution function (BRDF) (Nicodemus, Richmond, Hsia, Ginsgerb, & Limperis, 1977). The ideal Lambertian diffuse target assumption simplifies analytical solutions in passive imagery, but, in lidar radiometry, it leads to a well-known cosine correction (Wagner et al., 2006). Alternatively, an ideal isotropic diffuse target assumption allows the omission of a cosine correction and simplifies analytical formulas for active imagery. While both models represent simplifications of an actual BRDF, work by Kukko, Kaasalainen, and Litkey (2008) suggests that ideal isotropic diffuse reflectance might be a better assumption for certain materials. For vegetation, the work of Govaerts, Jacquemoud, Verstraete, and Ustin (1996) demonstrated that neither of the simple diffuse models is correct. The research on angular effects of lidar backscatter in vegetation is sparse and among the recent literature one can highlight the work of Hancock et al. (2017) in which the authors investigated leaf moisture estimation and leaf-bark separation.

3.1.5   *Relevant studies and impetus for the experiment*

As discussed in 3.1.1, SVIs are widely used and of immediate practical interest in many applications. However, the major difficulty in the case of ms lidar is that true surface reflectance is not equivalent to pulse return signal intensity DNs. Reflectance is a spectral characteristic of the target, while the intensity captured by commercial lidar sensors is an index of peak signal backscatter amplitude, which is further influenced by sensor and data acquisition characteristics (Hopkinson, 2007). Without calibration targets (Kaasalainen et al., 2009; Wagner et al., 2006) or a proven model which accounts for system and external factors (e.g., atmospheric conditions), it is not possible to accurately calculate reflectance values from intensity DNs. Using calibration targets often is not practical, and, currently, most of the characteristics of a particular system are considered a manufacturer's intellectual property and are not readily provided for precise modeling. It is possible, however, to conduct an independent calibration of a given system for a particular application. Consequently, one can foresee a widespread use of SVIs calculated from ms lidar intensity DNs, leading to a question of how consistent such products might be with a diversity of instrumentation used to collect the DNs. Moreover, from Equations 3.16 we see that in the case of split returns, average intensity is not a wholly spectral characteristic, and this fact, in turn, raises the question of how SVIs calculated with this metric might differ from SVIs derived from only single returns` intensities over the same vegetated area.

In (Hopkinson et al., 2016), Titan intensity responses were compared with

values obtained from three single-wavelength (corresponding to Titan`s) sensors and

noted that the intensity distributions obtained from the former were closer to each

other, explaining this fact by a Titan system design consideration. Because

radiometric targets were not used for the study above, it would not be possible to

compare SVIs derived from single-wavelength sensors to those of Titan. However, if

the same ms lidar system is flown over the same area at different altitudes during the

same time window, it is possible to compare the consistency of ratio-based SVIs

derived from the different channels of lidar emission wavelengths for different

altitudes. Following this logic, an experimental survey was conducted with the Titan

sensor at three different altitudes above ground: 500 m, 1000 m, and 1500 m (note

that 1500 m is higher than 1070 m from (Hopkinson et al., 2016)).

3.1.6   Hypothesis and objectives

3.1.6.1   Single channel intensity ratios

It is expected that, for extended targets, intensity single-channel`s ratios follow the

radiometric equation (we denoted height above ground as *H1 < H2 < H3*):

$$
\frac{< \tilde{I}_i^{ext} > |_{H1}}{< \tilde{I}_i^{ext} > |_{H2(3)}} = \frac{< \rho_t^i > |_{H1}}{< \rho_t^i > |_{H2(3)}} \; \frac{\mu_{atm}^{H1}}{\mu_{atm}^{H2(3)}} \quad .
$$

Equation 3.17

E.g., we expect to see increases in ratio due to atmospheric transmission losses.

However, for vegetated areas it is unclear how single-channel ratios of averaged

intensity from all returns, and from single returns, compare to the extended target return ratios.

3.1.6.2   *Comparison of point density distributions across three altitudes*

It is understood that with increasing survey altitude, the density of points over vegetated areas will decrease, both due to sampling geometry and pulse energy extinction, eventually reaching zero. From Hopkinson et al. (2016) paper, we see that average intensity value (a unit-less index) at a flight altitude of 1070 m AGL (above ground level) is low (reported 12.4) for C3. Thus, for the purpose of extracting SVIs from ms lidar data, it is crucial to adopt survey parameters (e.g., AGL) that enable sufficient point density for analysis.

3.1.6.3   *Consistency of spectral vegetation indices through different altitudes*

Here we evaluate the consistency and behaviour of active laser SVIs sampled from different altitudes. The expectation is that spectral indices are consistent over extended targets. However, over vegetated areas consistency is likely to be influenced by sample point density, differential canopy attenuation with each channel and raster methodology; all of which require exploration to build a deeper understanding of active laser SVIs. Firstly, one can filter out single returns and expect that the volumetric nature (or returned pulse width) is similar over different channels at different altitudes. Secondly, one can use all echoes and calculate averaged intensity assuming that the same structure would provide similar properties of lidar backscatter across all channels.

If we normalize intensities using the inverse square of target range for calculating the spectral ratio, we can write:

$$s\rho^{lm}(<\tilde{I}_i^l>,<\tilde{I}_i^m>) = \frac{k^l\, P_t^l\, \frac{\pi\, D_l^2}{16\, \mathbb{R}^2} <\rho_i^l>\, \mu_{atm}^l\, \mu_{sys}^l}{k^m\, P_t^m\, \frac{\pi\, D_m^2}{16\, \mathbb{R}^2} <\rho_i^m>\, \mu_{atm}^m\, \mu_{sys}^m} \quad . \qquad \text{Equation 3.18}$$

Neglecting any differences in atmospheric correction for different slant ranges, we can define a shorthand for a constant c^{lm}:

$$c^{lm} = \frac{k^l\, P_t^l\, D_l^2\, \mu_{atm}^l\, \mu_{sys}^l}{k^m\, P_t^m\, D_m^2\, \mu_{atm}^m\, \mu_{sys}^m} \approx constant \quad , \qquad \text{Equation 3.19}$$

leading to:

$$s\rho^{lm}(<\tilde{I}_i^l>,<\tilde{I}_i^m>) \approx s\rho^{lm}\left(<\rho_i^l>, \frac{<\rho_i^m>}{c^{lm}}\right)$$

$$\qquad\qquad\qquad \text{Equation 3.20}$$

$$= c^{lm}\, s\rho^{lm}(<\rho_i^l>,<\rho_i^m>) \quad .$$

Repeating the same manipulation with the normalized difference index, we obtain:

$$n\delta^{lm}(<\tilde{I}_i^l>,<\tilde{I}_i^m>) \approx \frac{c^{lm}<\rho_i^l>-<\rho_i^m>}{c^{lm}<\rho_i^l>+<\rho_i^m>} =$$

$$\qquad\qquad\qquad \text{Equation 3.21}$$

$$= n\delta^{lm}\left(<\rho_i^l>, \frac{<\rho_i^m>}{c^{lm}}\right) \quad .$$

The latter may lead to confusion for a target of different spectral characteristics, while $s\rho$ - because we can move constant c^{lm} from inside the function - might be easier to compare to each other from different sensors and datasets. Thus, by calculating spectral ratios and normalized differences at three different altitudes, we can investigate the consistency of both indices.

3.1.6.4 Comparing the consistency of sρ vs. nδ

It is well established, that normalized differences and spectral ratios help to overcome calibration and atmospheric correction problems in passive imagery (Steven, Malthus, Baret, Xu, & Chopping, 2003). However, with the Titan sensor, because of non-coincident beam geometries, it is not clear, which family of indices is more consistent throughout altitudes. If we calculate SVIs derived from intensity DNs normalized to the inverse square range at three different altitudes (H1 < H2 < H3), we can compare them to each other across AOI by calculating ratios of SVI(H1)/SVI(H2) and SVI(H1)/SVI(H3). Let us introduce some simplification in notation:

$$< \rho_i^l >\equiv \hat{\rho}^l \ ,$$ Equation 3.22

$$< \tilde{I}_i^l >= \tilde{k}^l \, \mu_{atm}^l \, \hat{\rho}^l \ ,$$ Equation 3.23

$$s\rho^{lm}\big(< \tilde{I}_i^l >, < \tilde{I}_i^m >\big) \ \equiv \ \widetilde{s\rho}^{lm} \ , \text{ and}$$ Equation 3.24

$$n\delta^{lm}\big(< \tilde{I}_i^l >, < \tilde{I}_i^m >\big) \ \equiv \ \widetilde{n\delta}^{lm} \ .$$ Equation 3.25

Then, it can be shown that:

$$\frac{\widetilde{s\rho}_{H1}^{lm}}{\widetilde{s\rho}_{H2(3)}^{lm}} = \frac{\mu_{atm|H1}^l}{\mu_{atm|H1}^m} \frac{\mu_{atm|H2(3)}^m}{\mu_{atm|H2(3)}^l} \approx constant \ ,$$ Equation 3.26

and

$$\frac{\widetilde{n\delta}_{H1}^{lm}}{\widetilde{n\delta}_{H2(3)}^{lm}} = \frac{1 - \dfrac{\tilde{k}^m}{\tilde{k}^l} \dfrac{\mu_{atm|H1}^m}{\mu_{atm|H1}^l} \dfrac{\hat{\rho}^m}{\hat{\rho}^l} \quad 1 + \dfrac{\tilde{k}^m}{\tilde{k}^l} \dfrac{\mu_{atm|H2(3)}^m}{\mu_{atm|H2(3)}^l} \dfrac{\hat{\rho}^m}{\hat{\rho}^l}}{1 - \dfrac{\tilde{k}^m}{\tilde{k}^l} \dfrac{\mu_{atm|H2(3)}^m}{\mu_{atm|H2(3)}^l} \dfrac{\hat{\rho}^m}{\hat{\rho}^l} \quad 1 + \dfrac{\tilde{k}^m}{\tilde{k}^l} \dfrac{\mu_{atm|H1}^m}{\mu_{atm|H1}^l} \dfrac{\hat{\rho}^m}{\hat{\rho}^l}} \ .$$ Equation 3.27

Thus, we see that the $\widetilde{sp}$ ratios at different altitudes should be equal to a constant (at nadir) over the whole AOI and the $\widetilde{n\delta}$ ratios are a complex function of averaged target reflectance, system spectral irradiance, atmospheric transmittance factor, and system factor. Consequently, by comparing these two families of indices with each other, we may examine which one is preferable for classification purposes.

3.2   Data and Methods

3.2.1   Study Area and Data Collection

Discrete return Lidar data were collected at three wavelengths (532 nm, 1064 nm, and 1550 nm) using the multi-spectral Teledyne Optech Titan system in July 28th, 2016 at flying altitudes of 500 m, 1000 m, and 1500 m AGL over a rural area in south-east Ontario (near the town of Warkworth), characterised by field crops, forest stands, open pasture, roads, and houses (Figure 3.3). This site was chosen because of logistical convenience and familiarity of the field support team with the AOI. Data were collected at 75 kHz per channel and with a scan angle of +/-20 degrees. Scan frequencies (40 Hz, 38 Hz, and 32 Hz) varied with flying altitude (500 m, 1000 m, and 1500 m, respectively) to maintain a reasonably uniform sampling distribution. Altogether, ten swaths were collected – five at 500 m, two at 1000 m, and three at 1500 m – see Table 3.1 and Figures 3.4. Sensor characteristics are presented in the Table 1.1 and Appendix I.
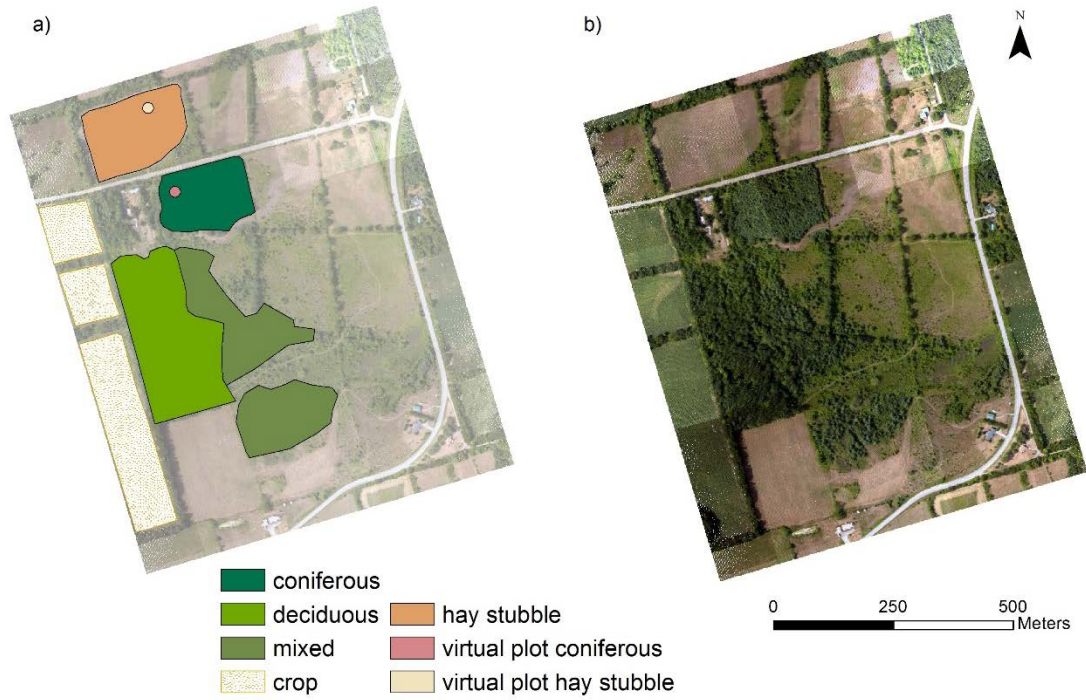
Figure 3.3 The AOI with highlighted classes on a) and Lidar point cloud colorized by passive RGB imagery on b). Thematic map was classified based on passive imagery and the familiarity of the field support team with the AOI.
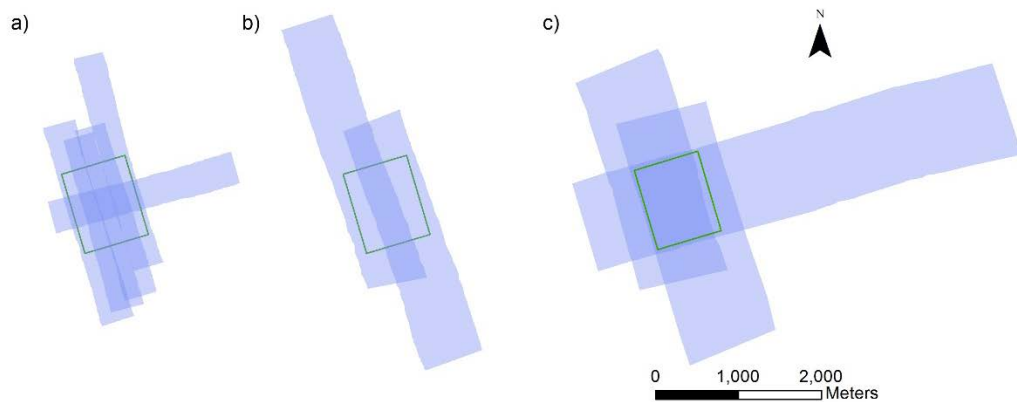
Figure 3.4 Swath coverage of the AOI by lidar at altitudes a) – 500 m, b) – 1000 m, and c) – 1500 m.

61

Table 3.1 Lidar parameters for each swath. *PRF (Pulse Repetition Frequency) is given for one channel.

Flight line	1	2	3	4	5	6	7	8	9	10
<Range>, m	491	540	547	546	536	942	1018	1475	1540	1555
PRF*, kHz	75	75	75	75	75	75	75	75	75	75
SF, Hz	40	40	40	40	40	38	38	32	32	32
Swath, deg	40.0	40.0	40.0	40.0	40.0	40.0	40.0	40.0	40.0	40.0
<Speed>, m/s	67	65	65	69	66	63	68	64	59	68
Heading, deg	160	340	160	340	250	160	340	160	340	250

Raw data in the form of a range file and a SBET file (smoothed best estimate trajectory) were processed in LMS (Lidar Mapping Suite, proprietary software from Teledyne Optech) and, after block adjustment, point cloud data were obtained with verified accuracy of RMS < 0.06 m in horizontal separation and RMS < 0.02m in height separation (LMS report).

3.2.2 Banding problem

During preliminary analysis, we found that intensity values differ based on the mirror scan direction of the system. For estimating the severity of this issue, we outputted scattered plots (Figures 3.5) of intensity vs. time for all channels at all altitudes for a virtual hay stubble plot (Figure 3.2a) of 11.3 m radii. As we can see from the plots, C3 channel shows no obvious evidence of this problem, C2 channel data display the greatest differences in intensity values with altitude, and C1 channel is affected to a lesser degree. As explained by (P. LaRocque, 2017), the effect is due to optical misalignment of the system, and its amplitude differs with a change in flight altitude,

maximum scan angle, and scan frequency. Because our study deals with system radiometry, we omitted the half of the data which was compromised for radiometric analysis, but we used all data for spatial or geometric products. Thus, the ground pattern for our radiometric data became similar to a rotating polygon scanning system with halved data density.
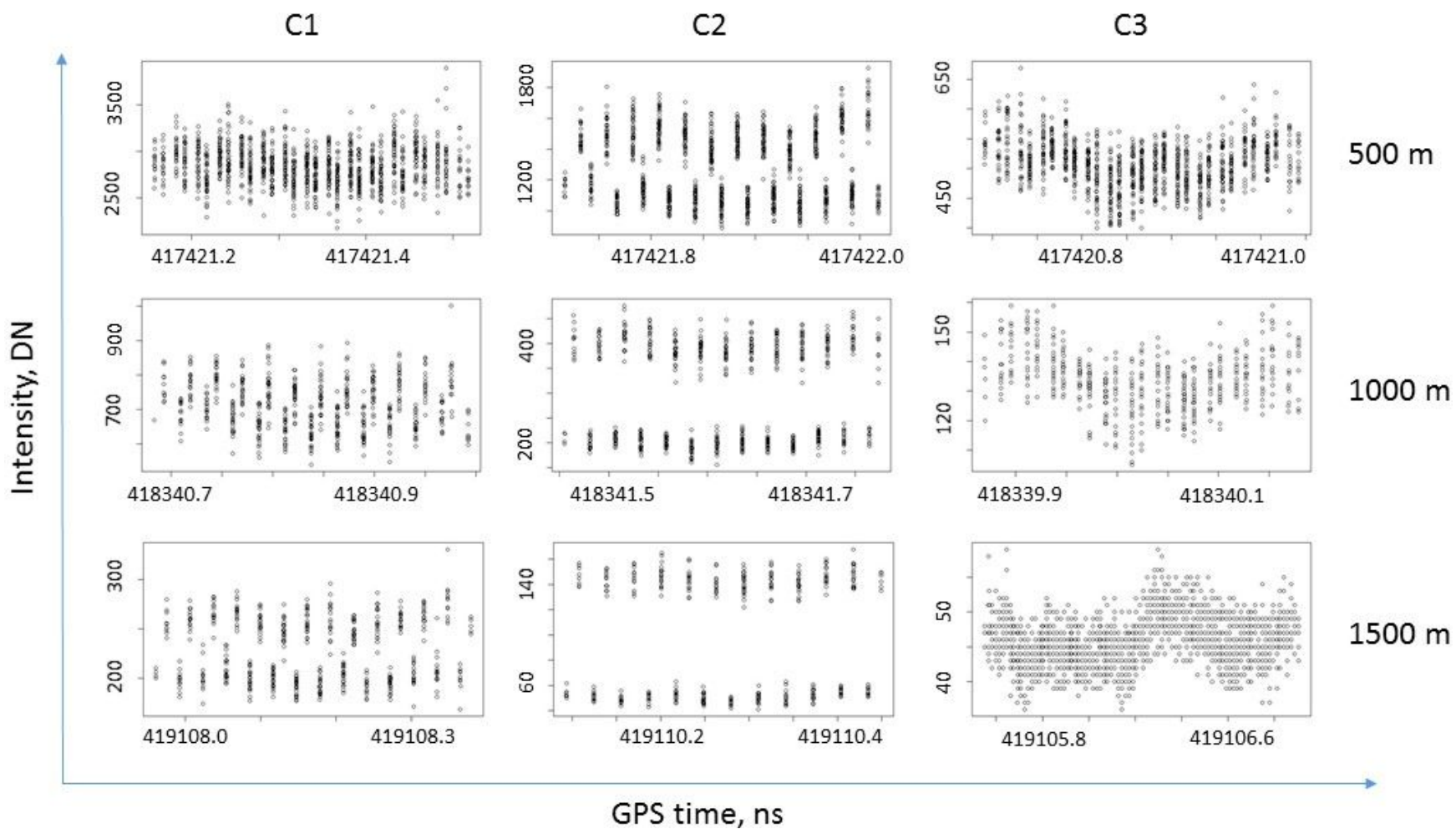
Figure 3.5 Intensity vs. time graphs for three channels and three altitudes over a virtual hay stubble plot. A difference in intensity with scan direction – zigzag patterns are clearly visible in time axes – is obvious for C2 and C1 channels.

3.2.2   Comparative analysis

Lidar data were outputted from LMS in LAS format with intensities normalized to a range of 1000 m. For radiometric analysis, two types of intensity raster grids of 4 m x 4 m were created with LAStools (rapidlasso GmbH (Isenburg, 2016)) for each channel and each flight altitude from normalized to range DN intensity values (note, that we used only one scan direction to avoid the banding issue) – one raster grid was calculated by averaging intensity of all returns inside the grid cell, and the second raster grid was calculated by including only single-echo returns and represents averaged-over-grid cell single-echo returns`intensity. These products were used for comparative analysis in the forms of different ratios, as explained below.

3.2.2.1   Single channel ratios

From intensity raster grids, single channel ratio grids were calculated with ArcGIS Spatial Analyst, separately for all returns and for single returns for two combinations – intensity at 500 m divided by intensity at 1000 m, and intensity at 500 m divided by intensity at 1500 m.

3.2.2.2   Point density

Point density raster grids of 2 m x 2 m were calculated with LAStools (Isenburg, 2016) for each channel and each altitude separately (note, we use both scan directions for this calculation). For the full AOI analysis, a summary table was filled with point densities, and numbers of returns, separated by echo type.

3.2.2.3   Spectral Vegetation Indices maps

Two types of SVI map were calculated with Spatial Analyst (ArcMap, ESRI) for three normalized difference indices $n\delta(C_2, C_3)$, $n\delta(C_2, C_1)$, and $n\delta(C_1, C_3)$, together with corresponding simple ratios, for each altitude – from averaged-all intensity raster grids and from averaged single return intensity raster grids.

3.2.2.4   Spectral Vegetation Indices ratios

Analogous to single channel ratios, SVI to SVI ratios at different altitudes were calculated, although, only for single return intensity products. For analyzing maps, raster histograms were outputted for ratios SVI (500 m) / SVI (1000 m), limiting the range of visualized values in such a way that outliers were not included. Histograms allow qualitative comparisons of simple ratio vs. normalized difference products derived from Titan sensor intensity DNs normalized to range.

3.3   Results

3.3.1   Single channel intensity ratios

Maps, resulting from calculating single-channel ratios are presented in Figures 3.6 and 3.7. Note, lower values of pixels over vegetated areas for all-echoes maps (Figure 3.6) in comparison to values of extended surfaces (fields), and different result for single-echo maps (Figure 3.6) – higher ratio values for vegetated areas in comparison to fields. Table 3.2 provides mean values and standard deviations for the images in Figures 3.6 and 3.7, together with p-values of significant difference from mean value equal to one for each distribution (95% confidence interval). In addition,

p-values of two-sample *Mann-Whitney* test for comparing all-echoes vs. single-echoes

are presented (95% confidence interval).

Table 3.2 Mean values and standard deviation for single-channel ratios for the whole AOI. One sample t-test (for the mean equals to one) p-values are given for 0.95 confidence interval. Two sample Mann-Whitney test p-values are given for 0.95 confidence interval.

		all echoes			Paired test, p-value	single echoes		
		MEAN	SD	p		MEAN	SD	p
a)	C3(500 m) / C3(1000 m)	1.08	0.20	< 0.01	< 0.01	1.31	0.23	< 0.01
d)	C3(500 m) / C3(1500 m)	1.14	0.30	< 0.01	< 0.01	1.30	0.18	< 0.01
b)	C2(500 m) / C2(1000 m)	1.19	0.15	< 0.01	< 0.01	1.31	0.23	< 0.01
e)	C2(500 m) / C2(1500 m)	1.20	0.17	< 0.01	< 0.01	1.51	0.33	< 0.01
c)	C1(500 m) / C1(1000 m)	1.22	0.20	< 0.01	< 0.01	1.34	0.27	< 0.01
f)	C1(500 m) / C1(1500 m)	1.29	0.20	< 0.01	< 0.01	1.60	0.33	< 0.01
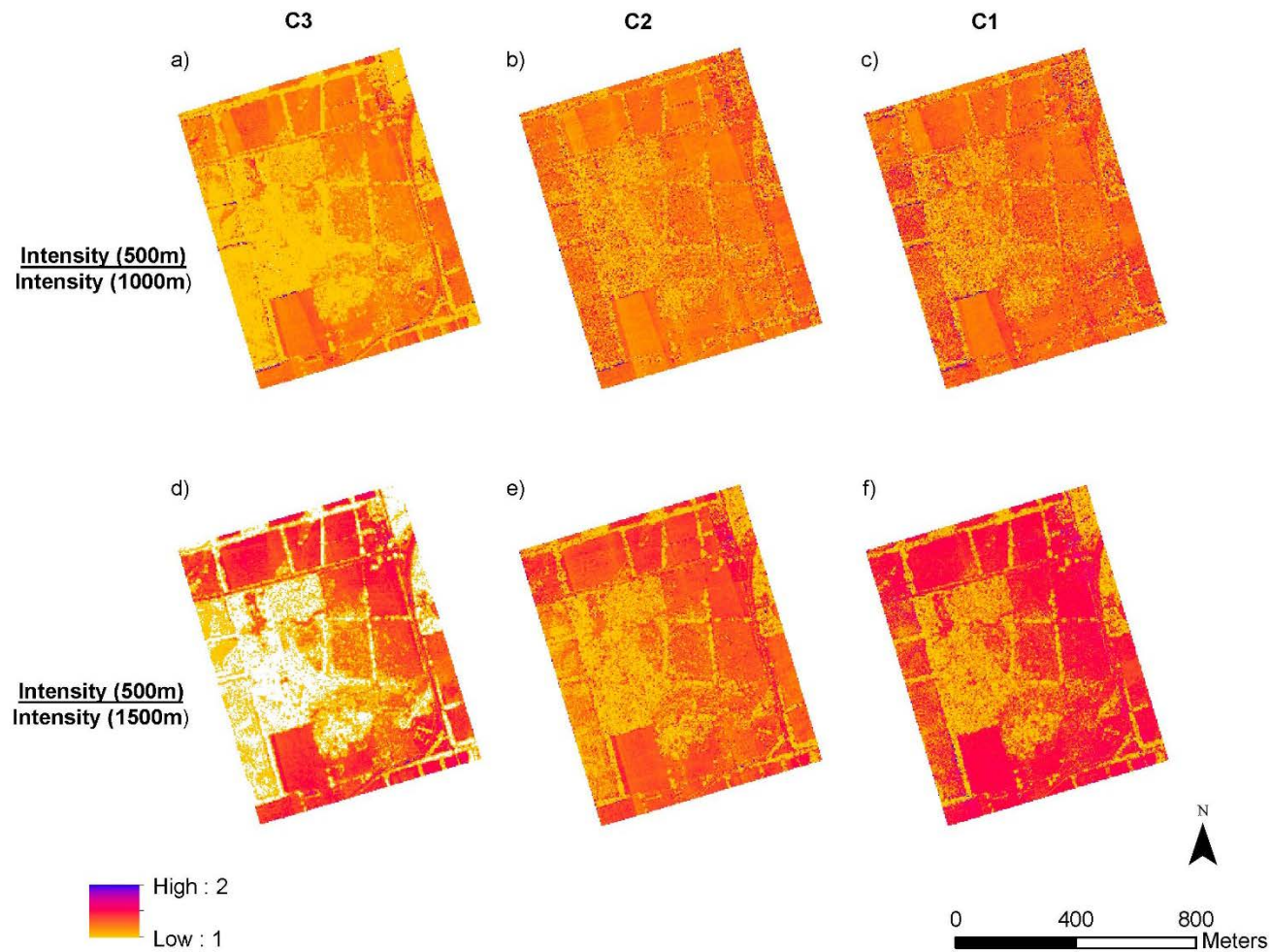
Figure 3.6 Single channels ratios - C_i (500 m) / C_i (1000 m) top and C_i (500 m) / C_i (1500 m) bottom – of normalized to range 1000 m average intensity at 4 m x 4 m grid from all returns. Left to right – C3, C2, and C1.
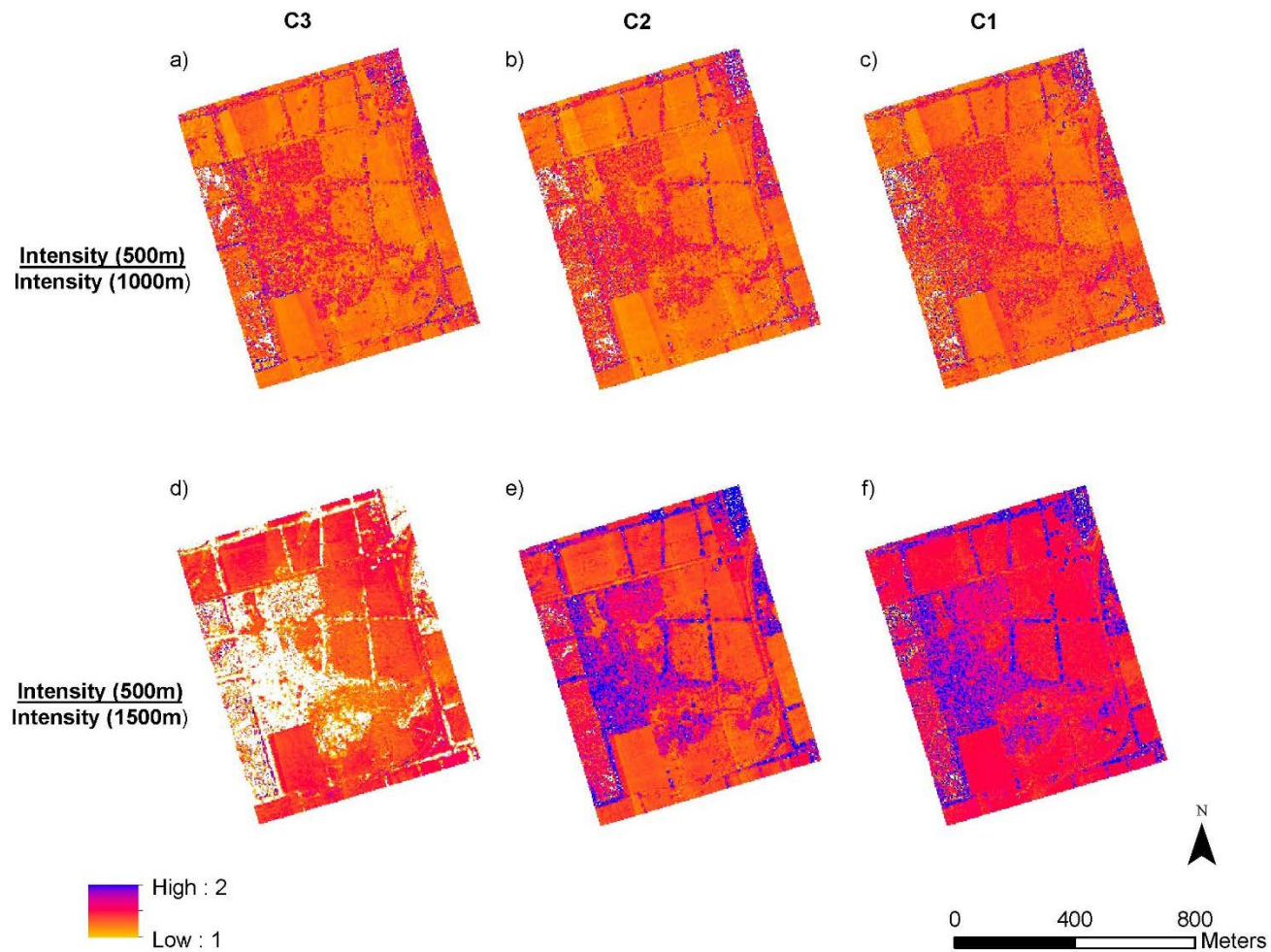
Figure 3.7 Single channels ratios - C_i (500 m) / C_i (1000 m) top and C_i (500 m) / C_i (1500 m) bottom – of normalized to range 1000 m average intensity at 4 m x 4 m grid from single echo returns. Left to right – C3, C2, and C1.

3.3.2   *Point density maps*

Table 3.2 presents a summary of the whole dataset. Figure 3.8 features density maps

for all channels and altitudes separately (note cross line 5 at 500 m AGL vivid on maps

a), d), and g)). Wide pattern of higher density on maps b), e), and i) corresponds to

swath overlaps and narrow patterns of higher density on the same maps, together

with ones on the maps c), f), and j) are due to aircraft attitude variation (e.g., rapid

pitch change) during the survey. Most noticeable are white (no data) pixels inside the

AOI over the majority of the vegetated areas on map c), which correspond to C3

channel at 1500 m survey altitude. In addition, some empty pixels appears over

vegetated areas on the map b) – C3 channel at 1000 m.

Table 3.3 Summary table of the Lidar dataset (note that statistics is given for all points in AOI)

C1 / C2 / C3	500 m			1000 m			1500 m		
	C1	C2	C3	C1	C2	C3	C1	C2	C3
Point density all	8.05	8.35	7.57	2.55	2.57	1.9	3.14	2.85	2.38
Point density last	5.7	5.71	5.68	2	2	1.8	2.8	2.59	2.38
Spacing all, cm	0.35	0.35	0.36	0.63	0.62	0.73	0.56	0.59	0.65
Number of returns	6,468,902	6,709,651	6,083,545	2,050,152	2,059,638	1,502,604	2,525,347	2,291,578	1,337,302
Footprint diameter at nadir, cm	18	18	35	35	35	70	53	53	105
Single	3,269,931	3,151,688	3,344,283	1,236,739	1,231,412	1,347,771	1,984,104	1,887,007	1,336,696
%	50.5%	47.0%	55.0%	60.3%	59.8%	89.7%	78.6%	82.3%	99.9%
Double	1,741,204	1,822,086	1,903,834	591,220	606,513	153,513	518,169	368,437	606
%	26.9%	27.2%	31.3%	28.8%	29.4%	10.2%	20.5%	16.1%	0.1%
Triple	933,480	1,087,821	673,996	181,753	183,627	1,316	22,510	35,130	0
%	14.4%	16.2%	11.1%	8.9%	8.9%	0.1%	0.9%	1.5%	0.0%
Quadruple	524,287	648,056	161,432	40,440	38,086	4	564	1,004	0
%	8.1%	9.7%	2.7%	2.0%	1.8%	0.0%	0.0%	0.0%	0.0%
First	4,584,010	4,588,576	4,562,217	1,603,452	1,605,753	1,425,026	2,251,163	2,083,401	1,336,999
Second	1,312,320	1,435,277	1,216,281	366,052	373,756	77,137	266,407	195,979	303
Third	441,804	524,168	264,788	70,566	70,627	440	7,636	11,947	0
Fourth	130,768	161,630	40,259	10082	9502	1	141	251	0
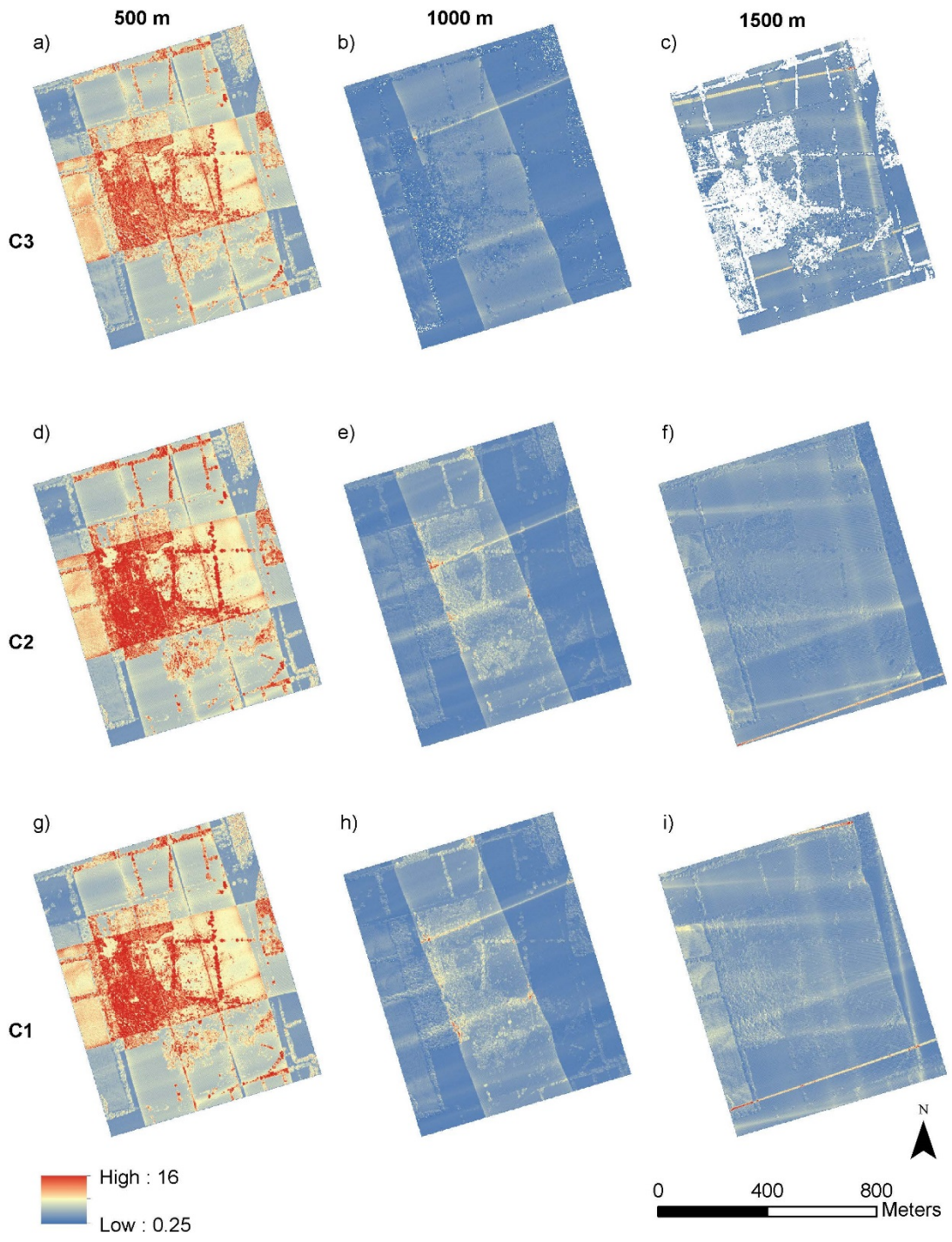
Figure 3.8 Point density maps from all returns, 2 m x 2 m grids. Top to bottom – C3, C2, and C1; left to right – 500 m, 1000 m, and 1500 m. Explanation for density patterns is in the text.

3.3.3   *Spectral Vegetation Indices maps*

On Figures 3.8 – 3.13, there are two types of normalized difference maps compared to corresponding simple ratios for all three combinations of interest – (C2, C3), (C2, C1), and (C1, C3) – for each altitude, the first type of maps are derived from all echoes and the second type is derived from single echoes. Maps in Figures 3.10, 3.12, and 3.14 are colored with a +/- two standard deviation colour scheme based on values derived from maps a) and d); maps on Figures 3.9, 3.11, and 3.13 are utilizing the same color scheme from the Figures 3.10, 3.12, and 3.14. Note the similarities over extended targets (e.g., fields) throughout all maps, consistency of values corresponding to vegetated areas on single-echoes indices` maps, and differences in pixel values of the same indices over the vegetated areas on maps derived from all echoes. Table 3.4 shows mean and standard deviation values for each image from Figures 3.8 - 3.13 and results of two-sample Kolmogorov – Smirnov tests of normalized differences and spectral ratios at 1000 m and 1500 m compared to those at 500 m in the form of D-values and p-values. Note, that all p-values are lower than 0.01 mainly due to the large sample size (~80,000) and do not represent "practical significance" (Lin, Lucas, & Shmueli, 2013). However, D-statistics of the test – the maximum distance between cumulative distribution functions – shows larger values for all returns (e.g., 0.19 for C2C3 at 1000 all) in comparison to single returns (0.02 for C2C3 at 1000 m singles).

Table 3.4 Mean values and standard deviation (in brackets) for nδ and sρ for the whole AOI at three altitudes, derived from all echoes and from single echoes - Figures 3.9-3.14. P-values and D-statistics from Kolmogorov-Smirnov test are given for comparisons of 500 m products to 1000 m products, and 1500 m products. All p-values are low because of the large sample size (~80,000) and D-statistics provide values of "practical significance" for interpretation.

	index	AGL, m	(C2,C3)		(C2,C1)		(C1,C3)	
			\<all\>	\<singles\>	\<all\>	\<singles\>	\<all\>	\<singles\>
a)	nδ	500	0.57 (0.10)	0.60 (0.12)	-0.14 (0.13)	-0.12 (0.16)	0.66 (0.06)	0.68 (0.07)
b)		1000	0.54 (0.09) D=0.19, p < 0.01	0.60 (0.12) D = 0.02, p < 0.01	-0.13 (0.14) D = 0.05, p < 0.01	-0.11 (0.16) D = 0.03, p < 0.01	0.62 (0.08) D = 0.24, p < 0.01	0.67 (0.07) D = 0.03, p < 0.01
c)		1500	0.50 (0.09) D = 0.33, p < 0.01	0.54 (0.08) D = 0.31, p < 0.01	-0.11 (0.13) D = 0.10, p < 0.01	-0.09 (0.14) D = 0.11, p < 0.01	0.60 (0.10) D = 0.31, p < 0.01	0.62 (0.08) D = 0.26, p < 0.01
d)	sρ	500	3.91 (1.11)	4.54 (2.03)	0.78 (0.23)	0.82 (0.27)	5.12 (1.05)	5.53 (1.60)
e)		1000	3.47 (0.85) D = 0.19, p < 0.01	4.49 (1.85) D = 0.02, p < 0.01	0.80 (0.23) D = 0.05, p < 0.01	0.84 (0.28) D = 0.03, p < 0.01	4.51 (1.09) D = 0.01, p < 0.01	5.42 (1.55) D = 0.03, p < 0.01
f)		1500	3.16 (0.75) D = 0.33, p < 0.01	3.44 (0.73) D = 0.31, p < 0.01	0.83 (0.21) D = 0.10, p < 0.01	0.87 (0.24) D = 0.11, p < 0.01	4.24 (1.17) D = 0.31, p < 0.01	4.49 (1.04) D = 0.26, p < 0.01
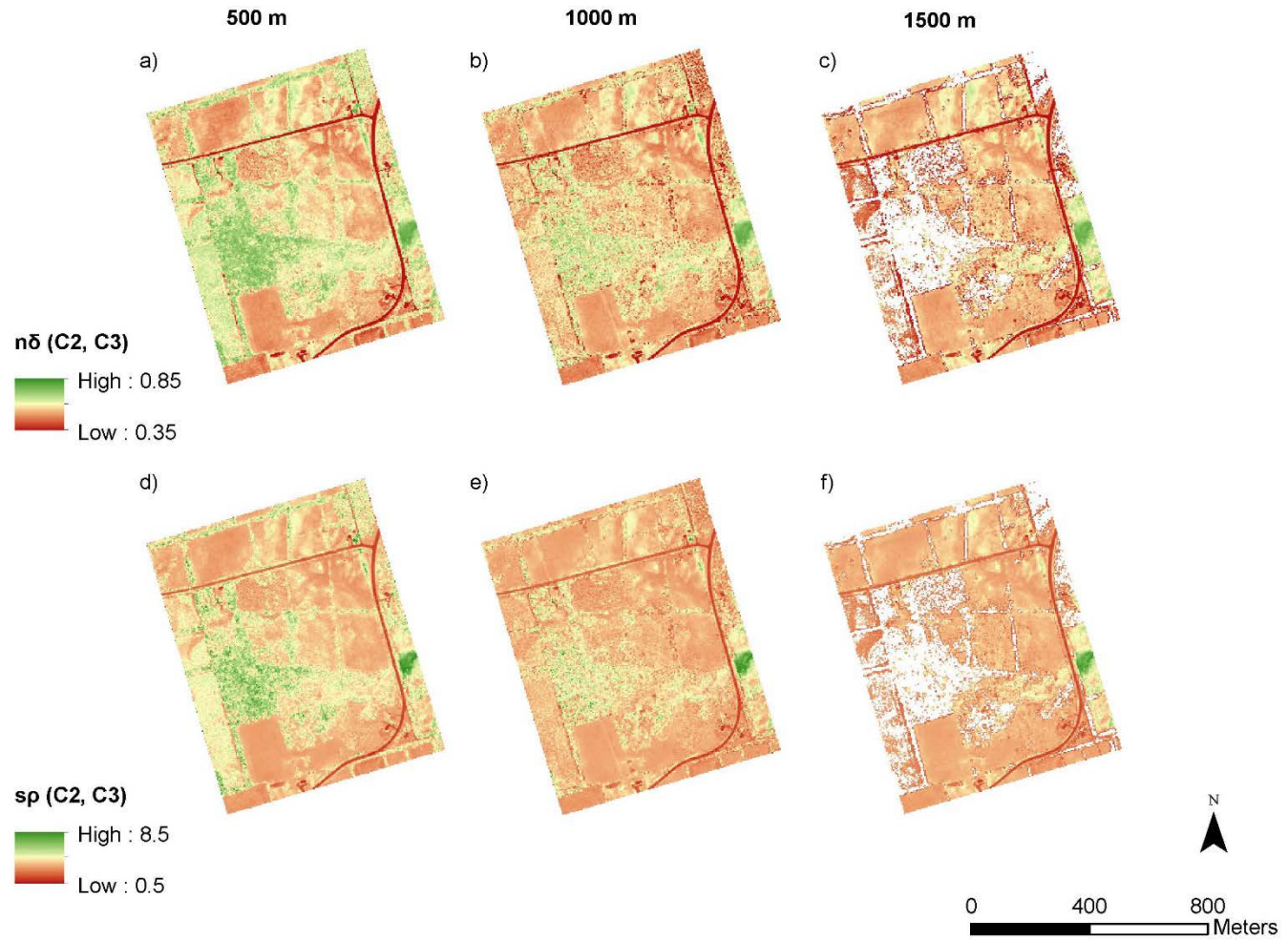
Figure 3.9 nδ (C2, C3) and sρ (C2, C3) for all returns, averaged over 4 m x 4 m grid.
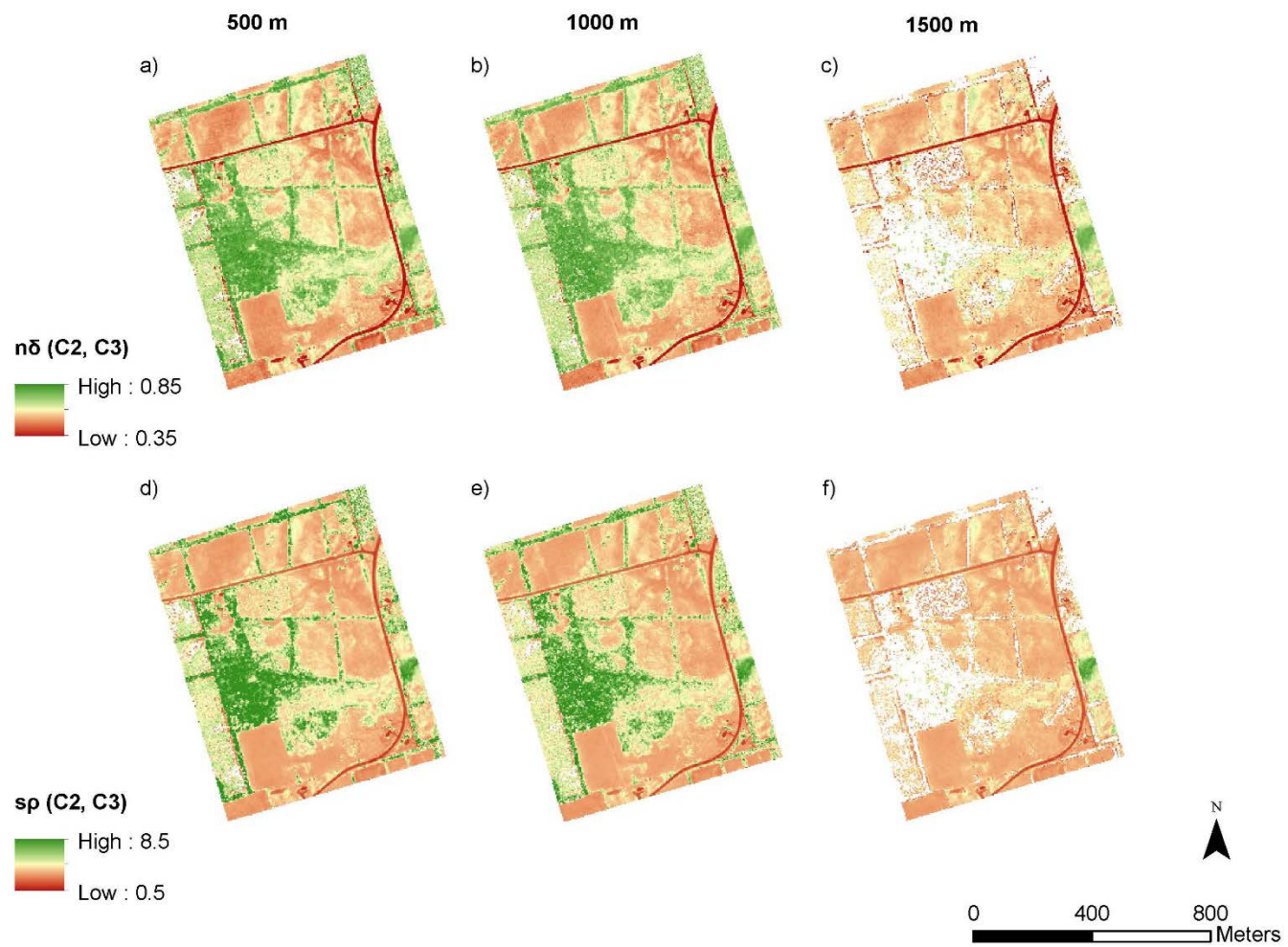
500 m **1000 m** **1500 m**

a)   b)   c)

nδ (C2, C3)

High : 0.85

Low : 0.35

d)   e)   f)

sρ (C2, C3)

High : 8.5

Low : 0.5

N

0   400   800
Meters

Figure 3.10 nδ (C2, C3) and sρ (C2, C3) for single returns, averaged over 4 m x 4 m grid.

Figure 3.11 nδ (C2, C3) and sρ (C2, C3) for all returns, averaged over 4 m x 4 m grid.

Figure 3.12 nδ (C2, C3) and sρ (C2, C3) for single returns, averaged over 4 m x 4 m grid.

500 m   **1000 m**   **1500 m**

a)   b)   c)

nδ (C1, C3)
High : 0.82
Low : 0.54

d)   e)   f)

sρ (C1, C3)
High : 8.73
Low : 2.33

N

0   400   800
Meters
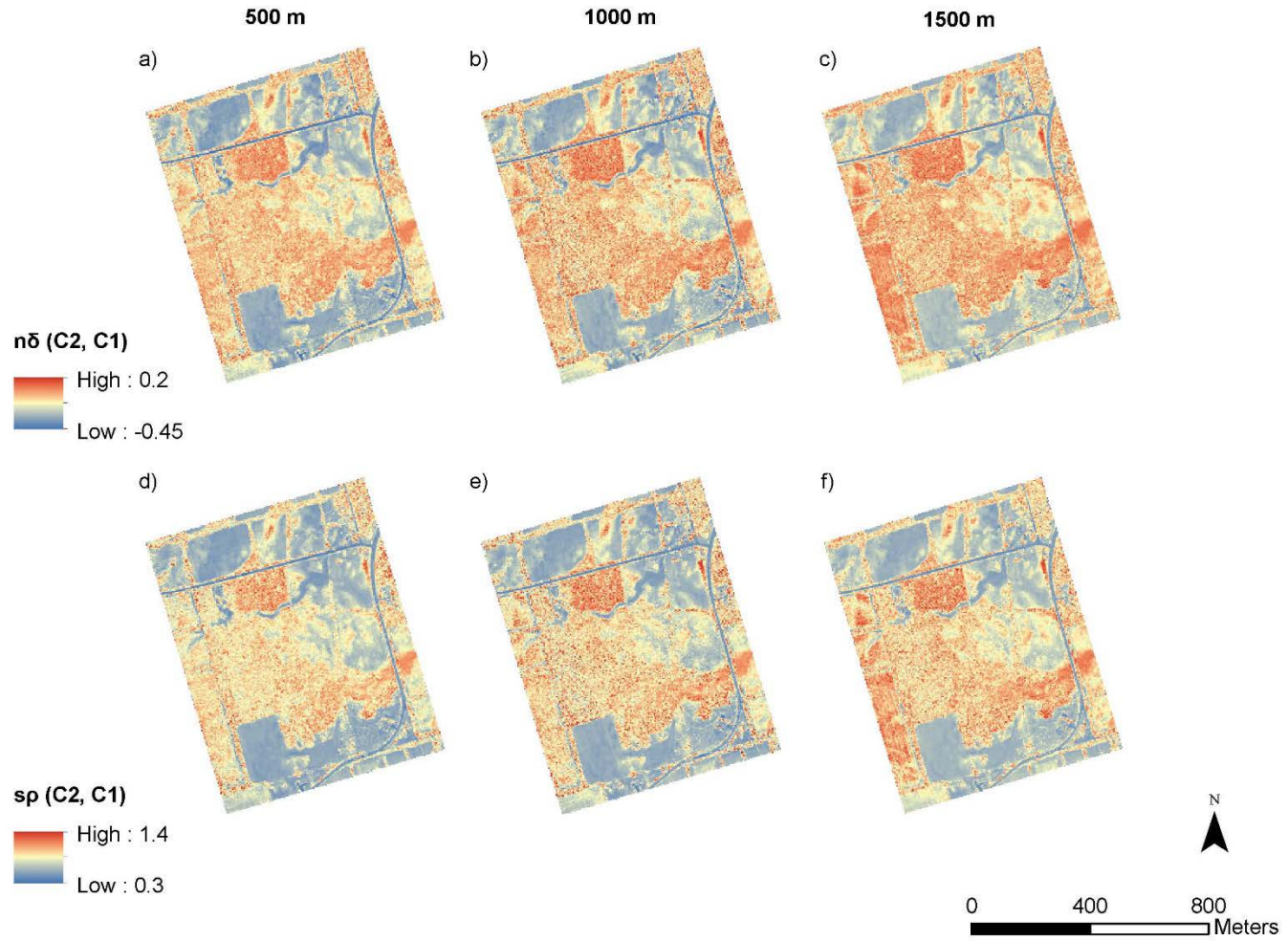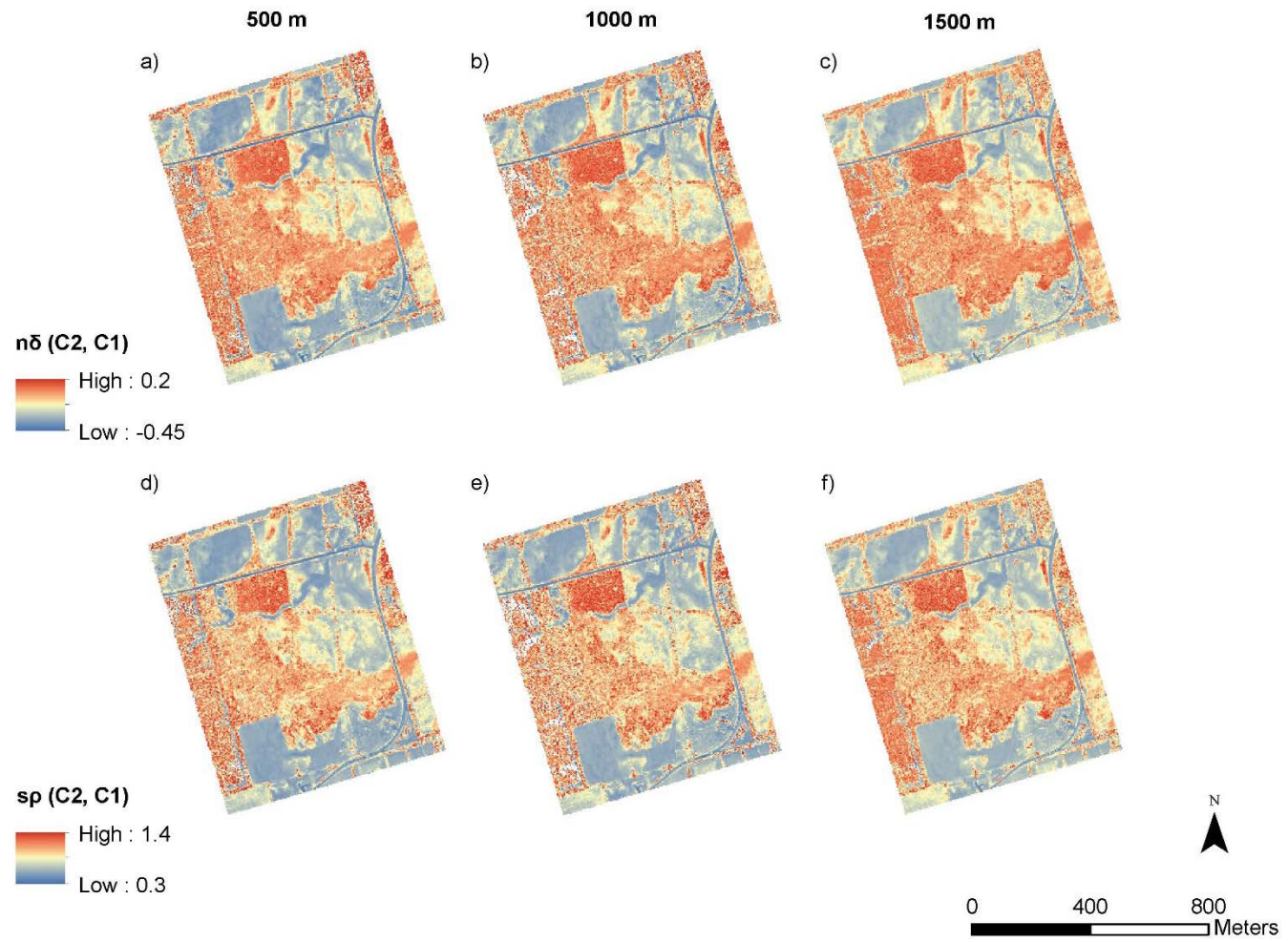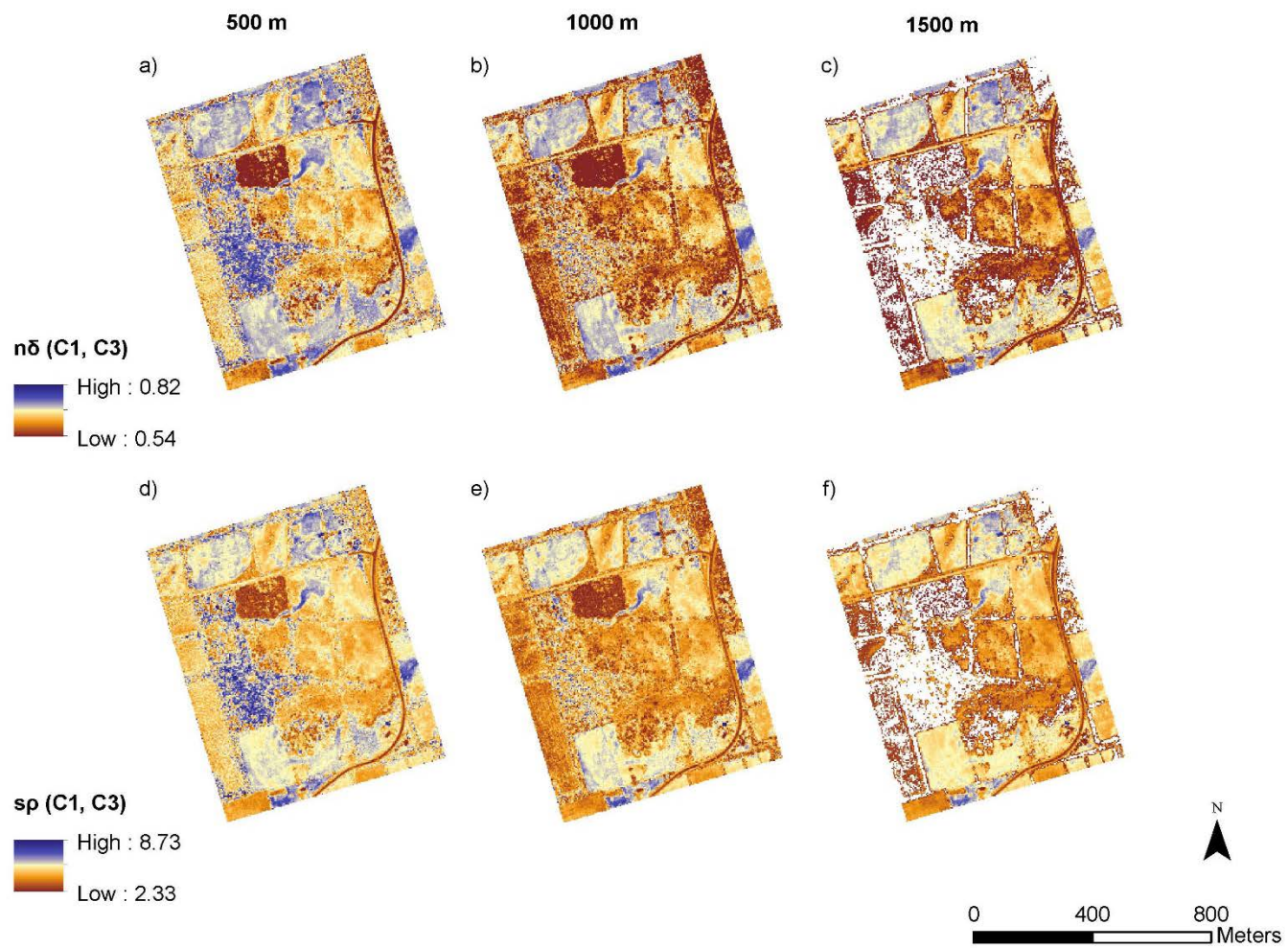
Figure 3.13 nδ (C1, C3) and sρ (C1, C3) for all returns, averaged over 4 m x 4 m grid.

79
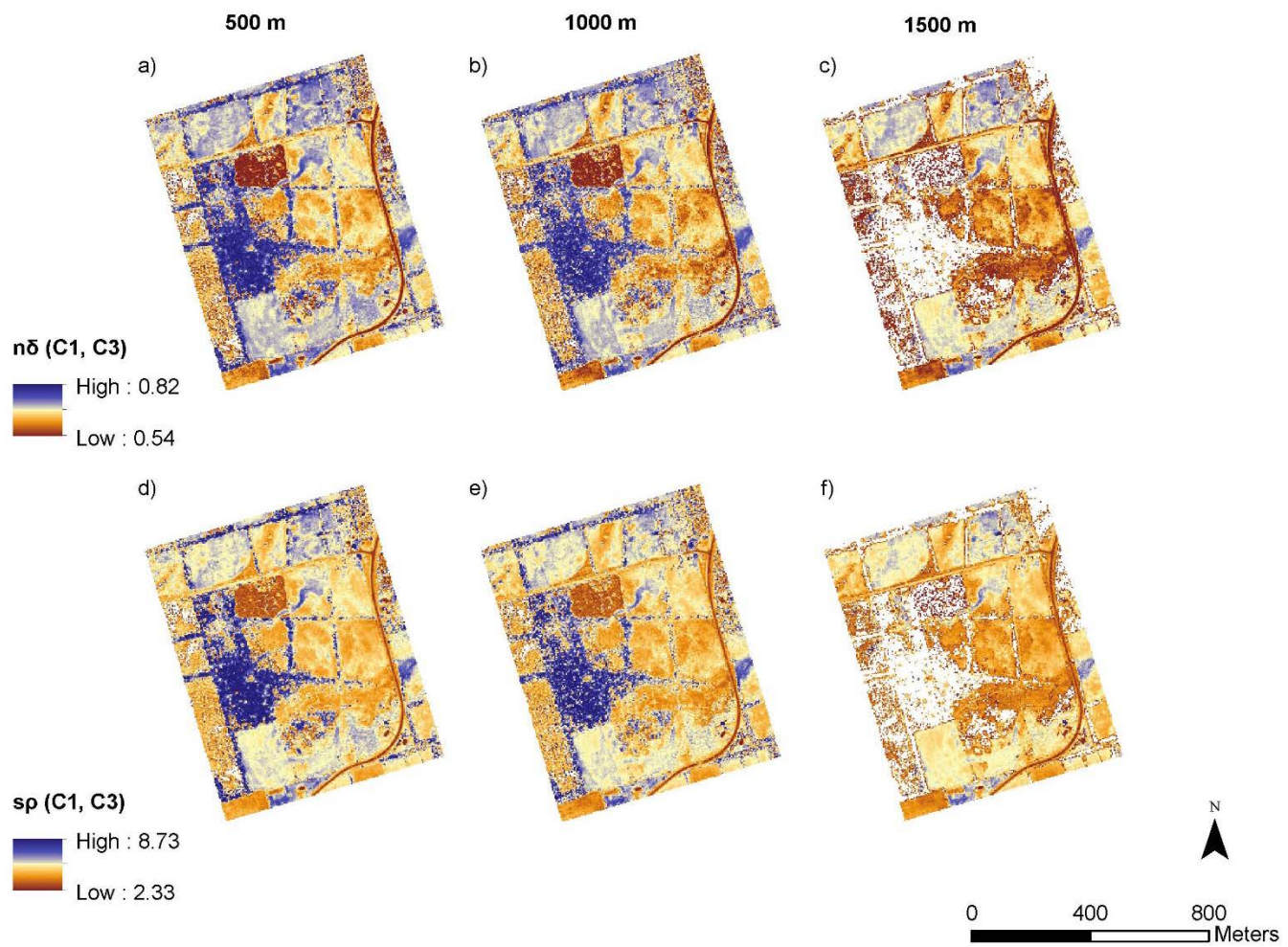
Figure 3.14 nδ (C1, C3) and sρ (C1, C3) for single returns, averaged over 4 m x 4 m grid.

3.3.4 Spectral Vegetation Indices altitude ratio maps and histograms

Figures 3.15, 3.17, and 3.19 show maps of SVI^i (500 m) / SVI^i (1000 m) together with SVI^i (500 m) / SVI^i (1500 m), Figures 3.16, 3.18, and 3.20 show the corresponding histograms for images a) and b) of the previous figure. Color scheme for all images is chosen base on +/- two standard deviations of *sρ (500 m) / sρ (1000 m) images*. The ratio range for all histograms is from 0.0 to 2.0. Table 3.5 shows mean, standard deviation, min, and max values for each image from Figures 3.15, 3.17, and 3.19.

Table 3.5 Mean, standard deviation, min, and max values of each image from Figures 3.15, 3.17, and 3.19.

		500 m / 1000 m			500 m / 1500 m		
		Mean(SD)	min	max	Mean(SD)	min	max
(C2,C3)	*sρ*	1.02(0.20)	0.15	10.10	1.13(0.40)	0.29	11.13
	nδ	1.00(0.62)	-11.95	130.06	1.05(0.33)	-35.06	28.14
(C2,C1)	*sρ*	1.00(0.18)	0.08	6.09	0.96(0.16)	0.07	5.78
	nδ	0.80(3.83)	-103.06	118.32	0.95(4.14)	-126.80	123.60
(C1,C3)	*sρ*	1.03(0.21)	0.08	12.68	1.21(0.41)	0.16	12.30
	nδ	1.01(0.09)	-5.92	8.43	1.09(0.22)	-15.81	12.07

sρ (C2, C3) **nδ (C2, C3)**

a) b)

index (500m)
index (1000m)

c) d)

index (500m)
index (1500m)

High : 1.4

Low : 0.6
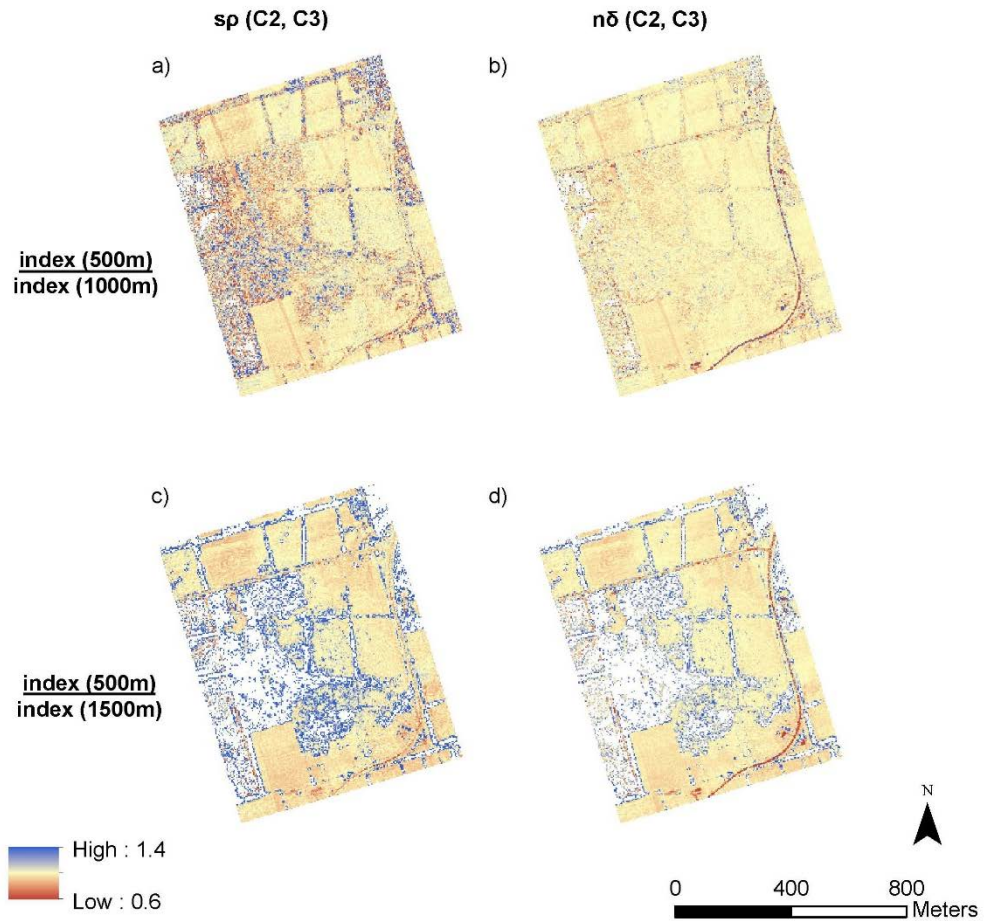
Figure 3.15 Ratios of sρ (C2, C3) at 500 m to sρ (C2, C3) at 1000 m and 1500 m - a) and c); and nδ (C2, C3) at 500 m to nδ (C2, C3) at 1000m and 1500m - b) and d); ratios are derived from single echoes indecies, 4 m x 4 m grid.
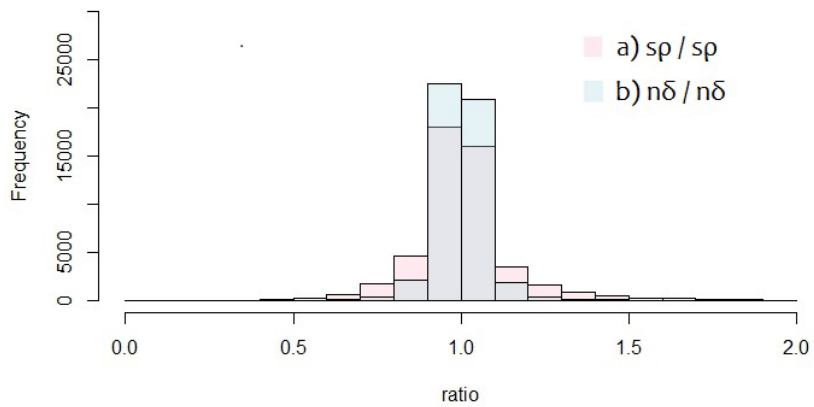
Figure 3.16 Histograms for Figures 3.15 a) and b).

sρ (C2, C1)   nδ (C2, C1)

a)   b)

<u>index (500m)</u>
index (1000m)

c)   d)

<u>index (500m)</u>
index (1500m)

High : 1.4

Low : 0.6

N

0   400   800
                        Meters
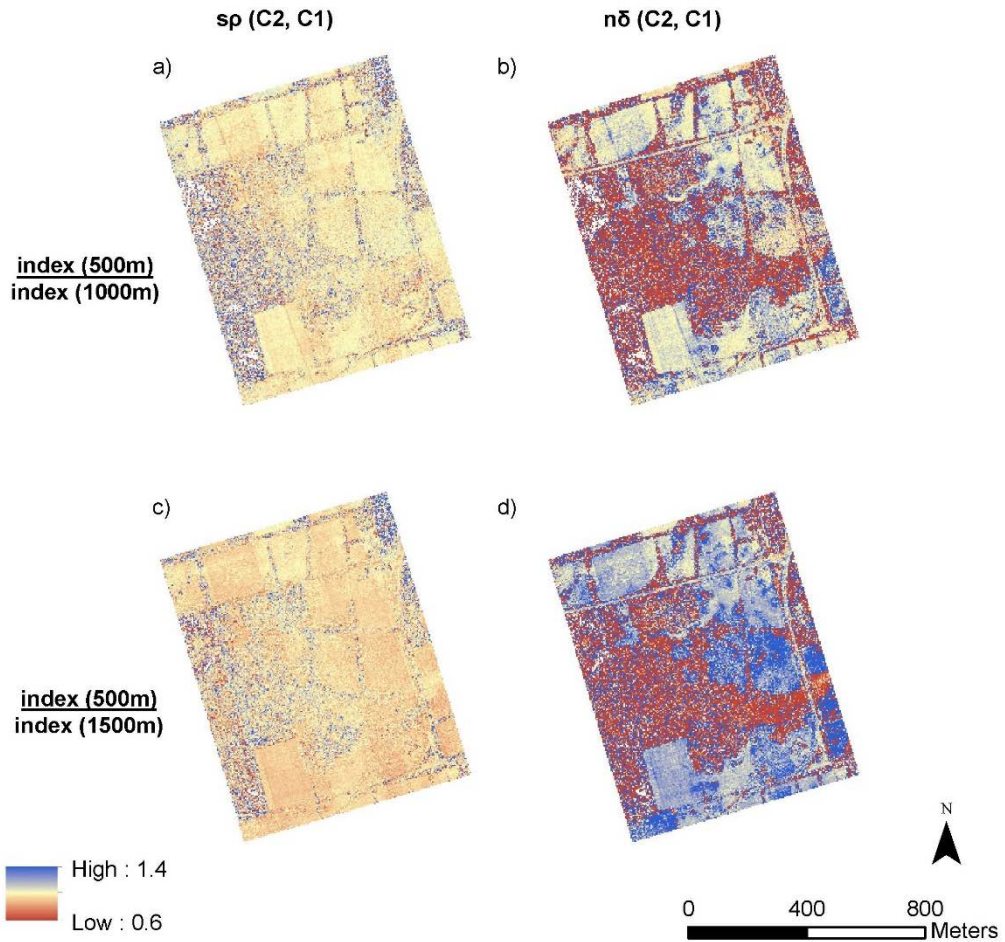
Figure 3.17 Ratios of sρ (C2, C1) at 500 m to sρ (C2, C1) at 1000 m and 1500 m - a) and c); and nδ (C2, C1) at 500 m to δ (C2, C1) at 1000m and 1500m - b) and d); ratios are derived from single echoes indecies, 4 m x 4 m grid.
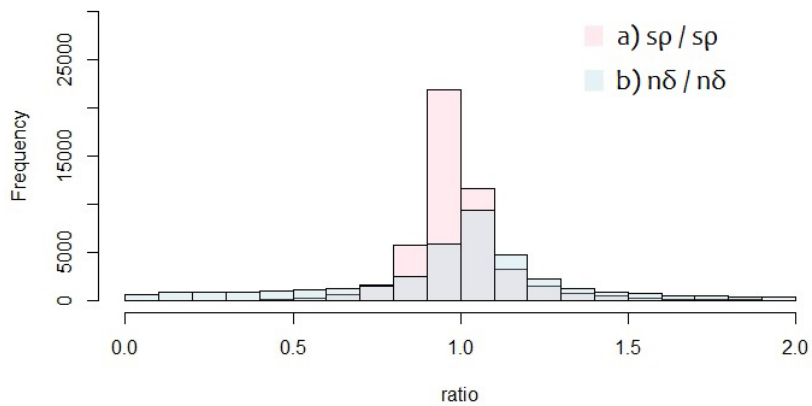
Figure 3.18 Histograms for Figures 3.17 a) and b).

sρ (C1, C3) nδ (C1, C3)

a) b)

$$\frac{index\ (500m)}{index\ (1000m)}$$

c) d)

$$\frac{index\ (500m)}{index\ (1500m)}$$

High : 1.4
Low : 0.6

N

0   400   800
Meters
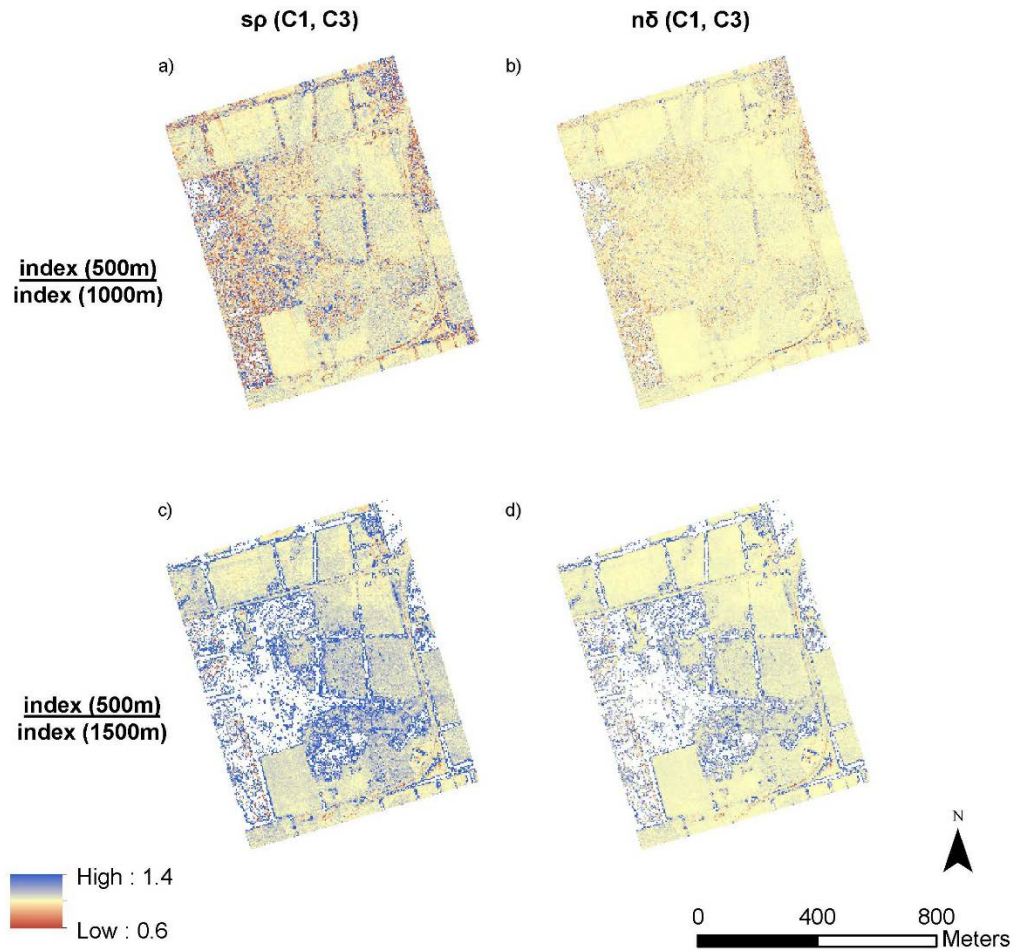
Figure 3.19 Ratios of sρ (C1, C3) at 500 m to sρ (C1, C3) at 1000 m and 1500 m - a) and c); and nδ (C1, C3) at 500 m to nδ (C1, C3) at 1000m and 1500m - b) and d); ratios are derived from single echoes indecies, 4 m x 4 m grid.
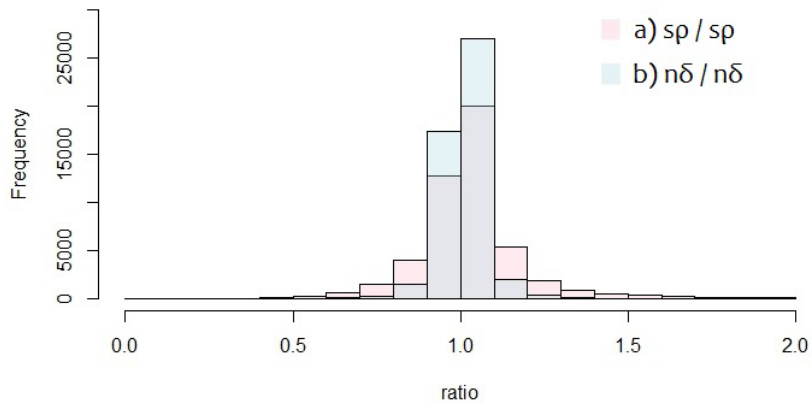
Figure 3.20 Histograms for Figures 3.19 a) and b).

3.4   Discussion

From Table 3.2, it is evident, and as expected from Equation 3.17, that the inverse square range normalization alone does not bring intensity DNs at different altitudes to equivalent values, and additional atmospheric correction is needed. However, we see that averages from all-echo ratios are smaller in comparison to averages from single-echo ratios. Moreover, from Figures 3.6 and 3.7, it is obvious that ratios over vegetated areas are increased in all-return ratio maps and decreased in single-return ratio maps in comparison to extended-target areas (e.g. hay stubble field). This effect can be explained by referring to the data in Table 3.3 – with higher altitudes, the proportion of split returns has decreased (i.e. more single returns). Multiple returns are, mainly, characteristics of tall vegetated areas. Thus, with ratios of averages-of-all-returns, we are, most likely, dividing intensity averaged over more returns from one pulse by intensity averaged over fewer returns from one pulse. If in Equation 3.17 we substitute extended targets with point targets and assume that only one emission-pulse is hitting the grid cell at nadir at two altitudes, then the average intensity at higher altitude is higher due to fewer return echoes. The average-of-all multiple returns intensity is not purely a spectral characteristic and such a metric cannot be compared through different areas inside the same raster as a spectral value (e.g., vegetation canopy vs. extended targets). In contrast, intensities derived from only single returns possess a more reliable and consistent spectral characteristic of the target. We see that with increasing altitude, the lidar backscatter signal weakened over vegetated areas to a greater degree than for extended target areas.

This observation can be explained by the temporal elongation of the lidar backscatter

response within tall vegetation, and an associated increase in the proportion of

backscatter below the system detection threshold (i.e. a reduction in return signal

below the noise floor).

From Figure 3.7, the green (532 nm) channel produced very little energy

backscatter from vegetation at 1500 m (in contrast to 1064 nm and 1550 nm) – no

signal above the noise level. Moreover, from Table 3.3 the proportion of split-returns

decreases with survey altitude for the Titan sensor. This observation justifies

proposing an altitude threshold (criterion) at which the point density from vegetation

is equal to that from a solid surface (or emission pulse density). Below this threshold

altitude, vegetation would have higher point density than extended targets (solid

surface), and above this altitude, vegetation displays lower point densities than

extended targets. This concept is illustrated in Table 3.6 with approximate values

from the Warkworth dataset.

Table 3.6 Point density m^{-2} of vegetated area in comparison to open area (second value) at one flight line averaging over 11.3 m radii circle area (both virtual plots, Figure 3.3a).

	532 nm	1064 nm	1550 nm
500 m	~ 4.2 / 2.4	~ 4.5 / 2.5	~ 4.2 / 2.4
1000 m	~ 1.0 / 1.3	~ 2.0 / 1.3	~ 2.1 / 1.3
1500 m	~ 0.04 / 0.8	~ 0.8 / 0.8	~ 0.9 / 0.9

From Figures 3.9 – 3.14, it is evident that spectral ratio maps display visibly consistent patterns and ranges in values over extended target areas. However, maps derived from single echoes are more consistent (smaller values of D statistics from the Kolmogorov-Smirnov test in Table 3.4) in comparison to maps derived from averages-of-all returns – the difference is evident in vegetated areas (Figure 3.3a shows delineated areas of vegetation). We also see that both $s\rho$- and $n\delta$- indices exhibit the same spatial patterns. Thus, it is possible to conclude that for vegetated areas, SVIs derived from single echoes over vegetated areas might be of more direct practical use than those derived from averaged intensity metrics. A similar result was reported in (Budei et al., 2018) after the implementation of a random forest technique for selecting the most useful ms lidar spectral metrics in individual tree species classification.

Figures 3.15 – 3.20 shows that the choice of the most consistent SVI between $s\rho$- and $n\delta$ – indices are wavelength dependent. Contrary to our expectation from Equations 3.26 and 3.27, $n\delta(C2,C3)$ and $n\delta(C1,C3)$ are superior over $s\rho(C2,C3)$ and $s\rho(C1,C3)$. However, in the case of the C1 and C2 combination, the spectral ratio $s\rho(C2,C1)$ is more consistent in comparison to $n\delta(C2,C1)$. This result is in line with the work of (Morsy et al., 2017) in which the authors concluded that $n\delta(C2,C1)$ – $NDVI_{NIR-MIR}$ in the author`s notation – is the noisiest index among Titan`s normalized differences. The reason for this result might be in the type of the land cover – the average simple ratio of C2 and C1 channels for the AOI is ~0.8, while simple ratios of C2 and C3, and C1 and C3 combinations are ~4.5 and ~5.5 (Table 3.4). Channel

dependent differences in atmospheric attenuation with altitude may lead to a change in intensity response from the scene, while the normalized difference may be oversensitive in areas where reflectance of C1 and C2 channels are close to each other. Thus, while it is possible to use combinations of $n\delta$(C2,C3), $n\delta$(C1,C3) and $s\rho$(C2,C1) indices for interpretation and basic classification purposes - such as vegetation and land-cover within an urban environment – it is recommended to combine all three laser channels for more sophisticated classification needs (e.g. Hopkinson et al. 2016).

3.5   Conclusions

It has been shown that atmospheric correction is needed to compare intensity DN values at different ranges and development of the atmospheric correction model is a next logical step. From point density analysis it became clear that the survey at 1500 m AGL with the Titan sensor does not provide enough lidar backscatter for the C3 channel over vegetated areas, and thus it is not recommended. Moreover, a survey altitude threshold criterion is proposed that may bring better comparability of datasets collected by different sensors and/or by the same sensor over different times and locations. It has been shown, that SVI products derived from single-echoes are more consistent across three altitudes over vegetated areas in comparison to SVIs derived from all echoes. After comparing the stability of SVIs through different altitudes, it is recommended to use the combination of $n\delta$(C2,C3), $n\delta$(C1,C3) and $s\rho$(C2,C1) indices for further analysis and classification of ms lidar point clouds. The

next logical step in studying radiometry of ms lidar sensors is radiometric correction

(Kaasalainen et al., 2009) which can be achieved by using ground reflectance targets.

4   Multi-spectral lidar: Radiometric calibrating targets, canopy reflectance, and vegetation vertical SVI profiles

Abstract

Multi-spectral (ms) airborne lidar data are increasingly used for mapping and change monitoring. Data is enriched by intensity digital numbers (DNs) and, by utilizing this additional information either directly or in the form of active Spectral Vegetation Indices (SVIs), enhancements in classification and change monitoring are possible. However, in case of SVIs, the indices should be calculated from reflectance values derived from intensity DNs after rigorous calibration.

In this thesis chapter, radiometric calibration of multi-spectral (ms) airborne lidar data collected over Cypress Hills Interprovincial Park in the summer of 2016 with a Teledyne Optech Titan sensor is presented. A novel low-cost diffuse reflectance coating was adopted for creating radiometric targets. Comparability of reflectance values derived from ms lidar data to available spectral libraries is shown. Active vertical profiles of Spectral Vegetation Indices (SVIs) were constructed and compared to modeled results available in the literature. The potential for a new landscape-level active 3D SVI voxel approach is demonstrated. Results of a field experiment with complex radiometric targets for estimating losses in detected lidar signals are described, and loss of up to 68% in the green channel is reported. Finally, an approach for estimating reflectance values from lidar split returns is analyzed and the results show similarity of estimated values of reflectance derived from split returns to reflectance values obtained from single returns.

90

4.1   Introduction

Light Detection and Ranging (lidar) established itself as a unique high-resolution remote sensing technology due to its 3D sampling of land cover and terrain, and its ability to penetrate into and characterize vegetation structure from treetop to ground (Vosselman & Maas, 2010). Lidar is primarily used to construct detailed digital elevation models (DEMs), but the intensity channel (an index of signal reflectance) is increasingly used in a similar fashion to black and white aerial photographs or single channels in multispectral imagery. In passive imagery, numerous SVIs (Spectral Vegetation Indices) have been developed based on reflectance values derived from image-based digital numbers (DNs) as quantitative indicators of vegetation phenology characteristics, including long-term patterns of loss or growth of photosynthesizing foliage. Modern multi-spectral (ms) lidar technology allows for active vertical spectral sampling of vegetation profiles opening new application prospects in forest inventory, habitat mapping, tree species classification, forest health assessment, and biomass and carbon stock estimation (Hancock, Lewis, Foster, Disney, & Muller, 2012; Hopkinson et al., 2016; Wallace, Nichol, & Woodhouse, 2012). However, it is well known (Holmgren, Nilsson, & Olsson, 2003; Hopkinson, Chasmer, & Hall, 2008; Stoker, Cochrane, & Roy, 2014) that when the data are collected with different sensors or sensor parameters, at different locations or at different times, the consistency of the obtained spectral information and its derivatives is not assured. Meanwhile, for developing comparable models (Mahoney, Hopkinson, Held, & Simard, 2016), classification and change detection (Yu,

91

Hyyppa, Kukko, Maltamo, & Kaartinen, 2006), and monitoring of yield curves and

vegetation health (Bater, Coops, Gergel, LeMay, & Collins, 2009; Donoghue et al.,

2007; Hopkinson et al., 2008), it is necessary to normalize spectral information

(intensity) from each channel or sensor (Hopkinson et al., 2016).

In recent years, a few publications have considered multi-spectral lidar for land

surface classification using traditional optical classification approaches (Hopkinson et

al., 2016; Karila, Matikainen, Puttonen, & Hyyppa, 2017; Matikainen et al., 2017), as well

as the development of active SVIs (Morsy et al., 2017; Morsy et al., 2016). Within a

forestry context, active SVIs, specifically active NDVIs (normalized difference

vegetation indices), were successfully used for classification of vegetation only

recently (Budei et al., 2018). Moreover, a potential of measuring plant physiology, leaf

moisture content, and leaf-bark separation by generating vertical profiles of spectral

indices was shown by modeling and lab experiments (Hancock et al., 2017; Morsdorf

et al., 2009; Woodhouse et al., 2011). This potential exists because spectral vegetation

indices can be linked to plant pigment concentration and leaf moisture content.

However, for consistency over time and comparability with other sensors and data

sets, SVIs should be calculated with reflectance derived from the lidar intensity DNs

after rigorous radiometric correction (Yan et al., 2012). For traditional single-channel

lidar (e.g., 1064 nm wavelength systems), there is over a decade of published

research into target-based radiometric calibration (Kaasalainen et al., 2009; A. Vain,

Kaasalainen, Pyysalo, Krooks, & Litkey, 2009; A. Vain, Yu, Kaasalainen, & Hyyppa,

2010), but such approaches have yet to be applied in operational ms lidar SVI

derivation.

Currently, two types of data output are available: DR (discrete-return) sensor-

supplied intensity values as an index of the peak signal amplitude, and not the time-

integrated backscattered light response; and FWF (full waveform) intensity profile

samples (typically 1 ns interval) of the detected intensity signal. However, even FWF

data with additional echo pulse width information cannot directly resolve the

ambiguity in intensity response between a combination of an area of contact of the

split return and the target reflectance. This constrains the analysis and interpretation

of split return intensities for SVI derivation, as it is impossible to know *a priori* if the

intensity of any individual return is mostly a function of contact area or reflectance

(as discussed in Chapter III). However, if the reflectance value of one of the echoes

from a double split return is *a priori* known, then, assuming homogeneous footprint

illumination, it should be possible to reconstruct both illuminated areas and the

unknown target reflectance using the following equations:

$$\rho_1 = \rho_0 \frac{I_1}{I_0 - I_2} \quad , \text{and} \qquad\qquad \text{Equation 4.1}$$

$$A_2 = A_0 \frac{I_2}{I_0} \quad . \qquad\qquad \text{Equation 4.2}$$

Here ρ_1 is the reflectance of the first point target, ρ_0 is the reflectance of the known

target, A_0 is the illuminated area of the whole footprint at nadir, A_2 is illuminated area

of the second target at nadir; I_0, I_1, and I_2 are intensity responses of the single echo

from the extended target, intensity of the first echo, and the intensity of the last echo

from the target with the same reflectance as ρ_0. For the volumetric returns, the

above equations should include pulse width, substituting intensity values with

calculated energy from a particular target cluster. A similar approach was utilized by

(Milenkovic et al., 2017) to introduce a new method of calculating total canopy

transmittance based only on the energy of ground echoes. However, Equation 4.1 has

never been rigorously tested in an experiment with a target of known reflectance. If

such a simple algorithm proves valid, it opens up the potential to derive reflectance

values for split returns with some *a priori* assumptions and, consequently, increases

the number of echoes available for SVI calculation or robust classification from a

particular survey.

To address issues associated with comparability of ms lidar derived reflectance

including reflectance derived from split returns to values obtained from other sensors

and to explore - and to compare to outcomes from modeling and laboratory

experiments - new type of data structure in form of active vertical SVI profiles, ms

lidar data were collected using a Teledyne Optech Titan sensor during August 2016,

over an area of interest (AOI) with installed radiometric targets. This experiment

addressed the following research objectives: i) to develop large scale radiometric

calibration targets and test them during an ms lidar data acquisition campaign, ii) to

derive reflectance (or pseudo-reflectance) values from calibrated ms lidar intensity

DNs and compare them to ground reflectance obtained by passive hyperspectral

sensors available in public spectral libraries, iii) to develop plot level active vertical SVI

profiles of vegetation from actual field data and compare them to modeled

(Morsdorf et al., 2009) and lab (Woodhouse et al., 2011) results published in the

literature, iv) to develop voxel data structure of active 3D SVIs and demonstrate its

potential on landscape level, and v) to set up an experiment with complex

radiometric targets for assessing feasibility of estimating reflectance from split

returns based on Equation 4.1 and explore energy losses of lidar backscatter signal in

the canopy.

4.2   Data and Methods

4.2.1   Radiometric calibration targets

Although there are plenty of options for lidar radiometric calibration targets

described in the literature (Kaasalainen et al., 2009; Kashani, Olsen, Parrish, & Wilson,

2015), a new version was adopted based on a low-cost diffuse reflective coating

developed by (Noble et al., 2008). This technique is similar to work by (Ants Vain,

Kaasalainen, Hyyppä, & Ahokas, 2009) and could be considered as a low-cost

operational alternative to Spectralon® targets. It was not possible to follow the

coating recipe precisely because some of the products are no longer available.

Anatase TiO2 pigment (Kronos® 1000) and a water-borne polyurethane binder

(Varathane® Interior Diamond Finish Water-based polyurethane) were used. Water

based white latex primer (Glidden, Vantage®) was used as the base layer and three

layers of coating were put on top using a roller. The reflectance of the targets was

validated in the lab using an ASD by comparison with a "white" Spectralon® panel of

known spectral reflectance values (~99%).

4.2.2   Radiometric calibration target experimental configuration

Figure 4.1 Photos of the radiometric calibration targets (made from 8' by 4' plywood). Photos a), b), and c) – are an open target, lifted target, and below-canopy target, respectively. Photos d) and f) illustrate corresponding transparency of the Lodgepole Pine foliage above the target and transparency of the lifted target.

Radiometric targets were constructed from 8' by 4' plywood sheets and

covered with a diffuse white coating as described above. To analyze split-return

characteristics of pulses passing through foliage, an elevated partial reflector surface

target was constructed with an accurately known 50% transmittance, achieved by

drilling 2.5" holes in the plywood sheet. One radiometric target was installed beneath

the forest canopy, while another target together with the elevated 50% transmittance

target were installed in a nearby clearing (Figure 4.1).

4.2.3 Study area and lidar data collection

The study was conducted in Cypress Hills Interprovincial Park (southwestern

Saskatchewan, Canada), 75 km north of the US border. The Cypress Hills is a unique

geological formation which rises on average 600 meters above the surrounding

plains (Beaty, 1975). There are four species of trees in the Cypress Hills, two of which

are coniferous. The Lodgepole Pine (*Pinus contorta*), which is usually found in the

Rocky Mountains, and is unique to the prairies. The second coniferous species is

white spruce (*Picea glauca*). There are two main deciduous tree species in the Cypress

Hills, Trembling aspen (*Populus tremuloides*) and balsam poplar (*Populus balsamifera*).

Almost 70 % of the AOI (Area of Interest, Figure 4.2) is covered with mature

Lodgepole Pine (LP) forest. An area of uniform LP stand was selected for further

analysis (Figure 4.2). One circle plot of 11.3m radii was established inside the stand

with 58 LP trees of average height 20.9m and of average DBH (Diameter at Breast

Height) 21cm. The plot displayed no developed understory and a uniform upper

canopy (Figure 4.1 c and c).

Discrete return multi-spectral lidar data were collected at three wavelengths

(532 nm, 1064 nm, and 1550 nm) using a Teledyne Optech Titan system on August 7th,

2016 at an average flying altitude of 600 m AGL. Data were collected at 100 kHz per

channel with a varied scan angle (from +/-22 to +/-27 degree) and scan frequency

(from 29 Hz to 35 Hz). Average aircraft speed varied from 63 m/s to 72 m/s depending

on the flight line. Consequently, point density varied; following the suggestion

(Chapter III) on comparing point density over vegetation to emission density as a

description of the dataset, average values are presented in Table 4.1. Sensor

characteristics can be found in Appendix I.

Table 4.1 Point density m^{-2} of vegetated area in comparison to open area (second
value) at one flight line averaging over 11.3 m radii circle area.

	532 nm	1064 nm	1550 nm
600 m	~ 4.5 / 2.7	~ 6.8 / 2.9	~ 5.8 / 2.9
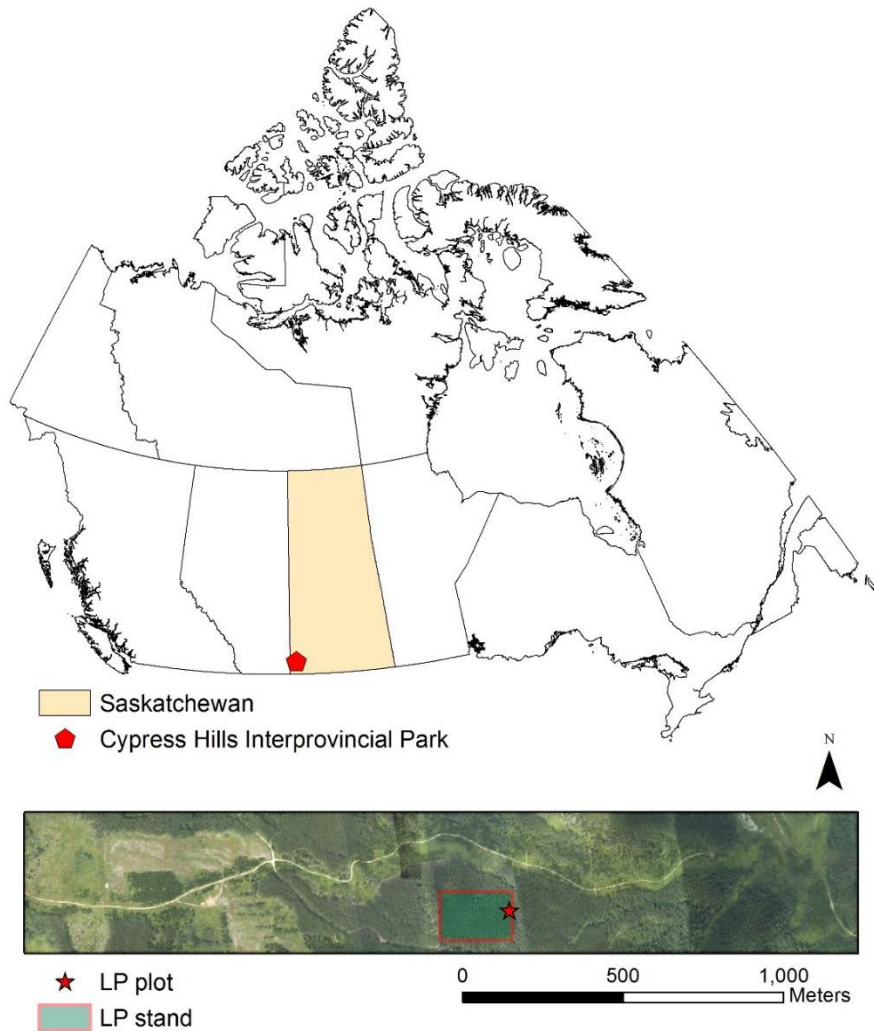
Figure 4.2 Area of interest (AOI) inside Cypress Hills Interprovincial Park colorized by RGB passive imagery. The LP stand and plot are depicted inside the AOI.

Raw data in the form of a range file and SBET file (Smoothed Best Estimate Trajectory) were processed in LMS (Lidar Mapping Suite, proprietary software from Teledyne Optech) and after block adjustment, point cloud data were obtained with verified accuracy (over available rooftops) of RMSE < 0.06 m in horizontal separation and RMSE < 0.04m in height separation.

4.2.4   Analysis

Lidar data were output from LMS in LAS format with intensities normalized to a range of 600 m. Firstly, due to the banding problem (described in Chapter III), half of the points were marked as compromised and omitted from the analysis. Locations of the targets were surveyed with a dual frequency Topcon Hiper SR survey-grade GNSS (Global Navigation Satellite System) receiver and coordinates of the target`s corners were post-processed using PPP (Precise Point Positioning (CSRS, 2017)). Returns from the targets were manually selected based on their spatial coincidence and proximity to the target border. Those which illuminated edges of the targets were excluded. Only points with the entire footprint (1/e², Gaussian shape) on a given target were used in analysis. Three flight lines provided returns from the targets – two because of the planned 50% overlap between lines and an additional crossline, which was planned for increasing the number of calibration target hits.

As a first step, DN values corresponding to 100% reflectance were derived for open target hits from two lines, leaving the cross line open target hits for verification. The DN value ($\tilde{I}^l_{\rho=100\%}$) corresponding to 100% reflectance and normalized to the inverse square range ($\mathbb{R}$) can be written in the form (see Chapter III, lidar radiometry):

$$\tilde{I}^l_{\rho=100\%} = \frac{100}{\rho_0^l} \overline{(I_k^l \frac{R_k^2}{\mathbb{R}^2} \frac{1}{\cos \vartheta_k})} \quad , \qquad \text{Equation 4.3}$$

with index l running through the three ms lidar channels and index k – through selected points over calibration target; I – intensity DN, angle ϑ – the angle between

the source and the target, and ρ_0^l – the known value of the calibrated target

reflectance for each channel. Consequently, all single-echo intensity DNs from every

point (index k) can be normalized with respect to the above value by the following

formula:

$$\rho_k^l = \frac{I_k^l}{\tilde{I}_{\rho=100\%}^l} \frac{R_k^2}{\mathbb{R}^2} \quad . \qquad\qquad \text{Equation 4.4}$$

Here, ρ_k^l represents a spectral pseudo-reflectance of a target at a particular

wavelength/channel (index l), i.e., a peak of the backscatter signal, normalized to the

response of an ideal diffuse Lambertian target of 100% reflectance.

Pseudo-reflectance of LP stands (Figure 4.2) was calculated separately for all

points from treetop to ground, and then only for the canopy (echoes higher than

10 m above ground). The resulting two point clouds were gridded into 15m pixel

reflectance raster maps (overall 150 pixels) with average values of pseudo-reflectance

assigned to each pixel. Then, the mean values of pseudo-reflectance for both maps

were compared to AVIRIS (Airborne Visible/infrared imaging spectrometer), AISA

Dual (Specim, Spectral Imaging Ltd.), and ASD (Analytical Spectral Device) data.

AVIRIS with 15 m resolution (R. F. Kokaly, Despain, Clark, & Livo, 2003) for mature LP

stands (45-150 years old, noted as LP1 in (R. F. Kokaly et al., 2003)) from Yellowstone

National Park (YNP) and ASD data for a stack of live LP needles (R.F. Kokaly et al.,

2017a) were retrieved from USGS (United States Geological Survey) spectral library.

AISA Dual hyperspectral sensor data with 2 m resolution for pines (unspecified

species) from the North Thompson, BC were received from Olaf Niemann

(Hyperspectral-LiDAR Research Group, University of Victoria). In addition, histograms of pseudo-reflectance for all single echoes from the canopy inside an LP plot (only echoes which were higher than 10 m above ground) were output.

For developing vertical normalized differences, the vertical distribution of each channel for the LP plot was analyzed, and after finding a lower canopy threshold, the echoes were binned in 0.5 m increments (index h). Then, from the average of each bin pseudo-reflectance value $\hat{\rho}_h^l$, normalized differences $n\delta_h^{lm}$ were calculated using the following formula (indices l and m run through Titans channels; see Chapter III for detailed explanation of $n\delta_m^l$):

$$n\delta_h^{lm} = \frac{\hat{\rho}_h^l - \hat{\rho}_h^m}{\hat{\rho}_h^l + \hat{\rho}_h^m} \quad . \qquad\qquad \text{Equation 4.5}$$

For the lifted target, the sum of the pseudo-intensity values of split returns, additionally normalized toward the cosine of the incident angle, were compared with the known reflectance of the open target. For the below-canopy target, single returns were compared with the returns from the open target, and double and triple echoes (with an assumption for triple echoes that first and second echoes detecting the same media) were used for deriving reflectance values of the canopy using Equation 4.1.

For illustrating mapping potential of the voxels approach, two types of map were created – ground nδ(C2,C1) map, and canopy nδ(C2,C1) and nδ(C2,C3) maps. For the ground map, only single echoes from ground returns and those up to 0.5 meters above the ground level were used. Ground nδ(C2,C1) map was visually compared with

DTM (Digital Terrain Model) map, and TPI (Topographic Positioning Index) map,

derived from 20m resolution DTM. For canopy maps, only single echoes penetrated

up to a certain depth (threshold value) into the canopy but of which some are still 2 m

above the ground. A two-sample Kolmogorov-Smirnov test on point height

distributions for each pair of all three channels was performed to find the threshold

value of canopy height that allows to compare vertical intensity distributions from

different channels. In addition, a vertical profile of $n\delta(C_2,C_1)$ was constructed with

Equation 4.3 along a 20 m wide transect, with voxels of 20 m by 20 m in plane and

0.5 m in height.

4.3   Results and Discussion

4.3.1   Radiometric calibration targets

A spectral reflectance curve of the target obtained from laboratory

measurements is presented in Figure 4.3. Values of spectral reflectance with RMSE of

measurements for Titan`s wavelengths are presented in Table 4.2. Spectral

reflectance values of the constructed target are similar to those reported by (Noble

et al., 2008).
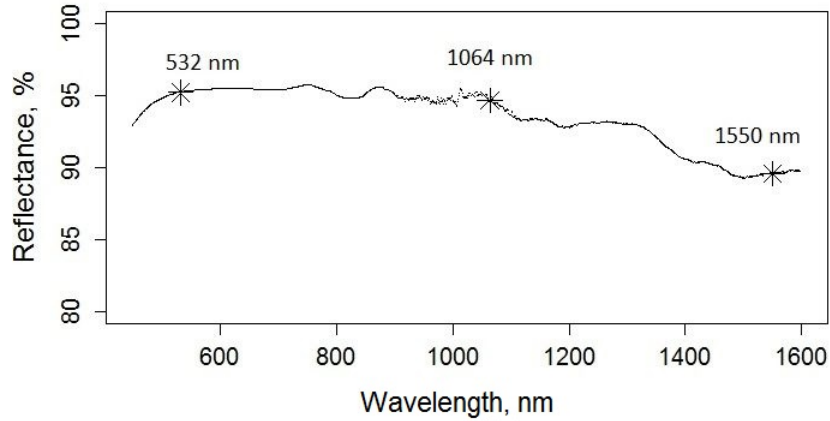
Figure 4.3 Spectral reflectance curve for the constructed targets.

Table 4.2 Values of spectral reflectance for wavelengths corresponding to Titan measured by ASD (20 samples). RMSE values in brackets.

Wavelength	532 nm	1064 nm	1550 nm
Reflectance, %	95.5 (0.1)	95.0 (0.5)	90.5 (0.9)

4.3.2 Verification of the intensity normalization

Calculated values of $\tilde{I}^l_{\rho=100\%}$ for each channel together with the values of reflectance derived for the open target hits from the crossline and additionally corrected to the cosine of the incidence angle are presented in Table 4.3. Additionally, these values are compared with the reflectance measured in the laboratory using an ASD.

Table 4.3 Values of DNs corresponding to 100% reflectance, normalized to 600m and calculated values of reflectance from the cross line. RMSE values and number of measurements (RMSE | N) are given in brackets.

	C1 (1550nm)	C2 (1064nm)	C3 (532nm)
DN normalized to 100% reflectance (600m)	3267 (145 | 6)	3151 (52 | 5)	3068 (116 | 3)
Verification of reflectance, %	91.0 (1.4 | 5)	96.4 (2.9 | 5)	93.4 (1.8 | 4)

Verification of the radiometric calibration shows good results – the derived values differ by 0.5% for the C1 channel, by 1.4% for the C2 channel, and by 2.1 % for the C3 channel (Tables 4.2 and 4.3). The derived reflectance was higher for the C1 and C2 channels and lower for the C3 channel. Since one of the lines used to derive the calibration value was flown 80 m lower than the second line and the cross-line used for the verification, one would expect that all derived values should be lower. Accounting for the difference in atmospheric losses may improve the results. However, it is assumed here that the 1-2% achieved accuracy is sufficient for constructing SVIs.

4.3.3   *Pseudo-reflectance derived from Titan compared to hyperspectral sensors data*

Comparison of Titan's derived pseudo-reflectance to the AVIRIS, AISA dual, and ASD data is shown in Table 4.4. Histograms of pseudo-reflectance for LP plot canopy are presented in Figure 4.4.

Table 4.4 Comparison of pseudo-reflectance derived from Titan single returns (SD in brackets) for LP stand in Cypress Hills compared to reflectance data from AVIRIS, AISA Dual, and ASD, and calculated two simple ratios ($s\rho^{532nm}_{1064nm}$ and $s\rho^{1550nm}_{1064nm}$). P-values of two-sample Mann-Whitney test for comparing Titan`s pseudo-reflectance and spectral ratios vs. AVIRIS and AISA Dual data are given.

	Pixel size	N	C3 (532 nm)	C2 (1064 nm)	C1 (1550 nm)	$s\rho^{532\,nm}_{1064\,nm}$	$s\rho^{1550\,nm}_{1064\,nm}$
Titan All LP, %			3.4(0.5)	27.7(3.3)	18.2(2.8)	0.12(0.01)	0.66(0.07)
Vs. AVIRIS	15m	150	p < 0.05	p < 0.05	p < 0.05	p < 0.05	p < 0.05
Vs. Aisa Dual			p < 0.05	p < 0.05	p < 0.05	p < 0.05	p < 0.05
Titan Canopy LP, %			2.5(0.1)	17.6(0.7)	8.4(0.3)	0.14(0.01)	0.48(0.02)
Vs. AVIRIS	15m	150	p = 0.09	p < 0.05	p = 0.51	p = 1	p = 0.39
Vs. Aisa Dual			p < 0.05	p < 0.05	p < 0.05	p < 0.05	p < 0.05
AVIRIS YNP-LP1, %	15m	4	2.3 (0.5)	15.3 (0.9)	8.0 (1.4)	0.15(0.02)	0.52(0.07)
AISA Dual Pines, %	2m	37	5.5 (0.7)	31.5 (5.4)	10.7 (2.8)	0.18(0.02)	0.34(0.08)
ASD LP, %	*	1	19.2(5.0)	67.1(2.3)	38.4(3.9)	0.28	57,2
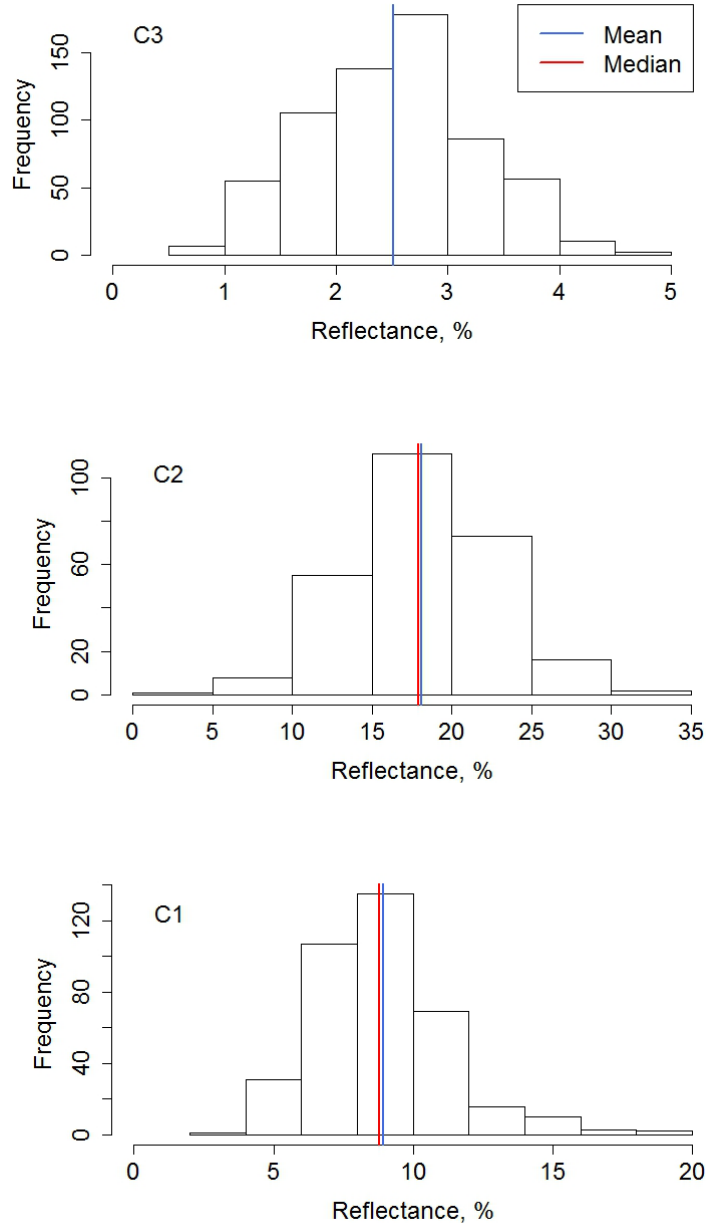
Figure 4.4 Top to bottom: C1, C2, and C3 reflectance (in %) histograms for single returns of the canopy (10m above ground) of the Lodgpole Pine plot of 11.3 m radii.

Comparison of derived pseudo-reflectance canopy values shows good

correspondence with AVIRIS reflectance data (Table 4.4) – p = 0.09 for C3, p = 0.51 for

C1. Although, p < 0.05 for C2 channel, both simple ratios ($s\rho_{1064nm}^{532nm}$ and $s\rho_{1064nm}^{1550nm}$)

comparison shows no significant difference between Titan derived values for canopy

and AVIRIS data (Table 4.4). However, it should be emphasized that values for AVIRIS

reflectance were obtained for different LP stands and it is rather the similarity in

overall magnitude of values that we are referring to in our comparison. For instance,

reflectance data from AISA Dual sensor are almost double those for C2 and C3

channels, and only 25% higher for C1 channel. In contrast, the ASD reflectance values

are approximately four times higher than those obtained from single echoes of ms

lidar. The latter can be explained assuming that canopy does not represent a

continuous target but rather a transparent target and, thus, absolute values of

reflectance should be lower than those obtained with ASD for elements of the

canopy, such as needles stacked together. However, comparison of pseudo-

reflectance derived from split returns to ASD data is more interesting, because the

algorithm based on Equation 4.1 accounts for transparency.

4.3.4   Lifted target and below-canopy target experiments

Values of double echoes pseudo reflectance from the lifted target and percentage of

the sum in comparison to the open target response are provided in Table 4.5. The

average loss (and range) are calculated and presented in Table 4.5 for each channel.

Table 4.5 Lifted target calibrated DNs from double echoes with the percentage of the sum to the open target DN in brackets. The average loss in comparison to the open target is shown in the bottom row.

	C3	C2	C1
	953-1381 (79.7%)	2162-430 (86.6%)	1369 – 1277 (84.4%)
	1265-1001 (77.3%)	1224-1240 (82.3%)	1344 – 1198 (81.0%)
	1333-824 (73.6%)	1314-1192 (83.7%)	1778 – 1101 (91.8%)
		1776-816 (86.6%)	
Average loss (range):	23.1% (6.1%)	15.2% (4.3%)	14.3% (10.8%)

Three single-echo hits from the below-canopy-target were observed (one hit for each channel) and their normalized intensities presented in Table 4.6 in comparison to DN values from the open target together with the calculated percentage of loss.

Table 4.6 Below-canopy single return DNs vs. open target DNs and the corresponding loss in intensity values in percentage. DN values were normalized to a 600 m range and corrected with the cosine of incidence angle. Only one hit (N = 1) for each channel was detected for the below-canopy target.

	C3	C2	C1
Below-canopy target single echo hit, DN	942	2838	3054
Open target, DN	2930	2994	3136
Loss, %	68 %	5 %	3 %

Tables 4.7 presents pseudo-reflectance derived from the first and second canopy echoes of the pulses with the last echo on the below-canopy target and the associated illuminated area calculated from the intensity of the last echo, illustrating

algorithm from Equations 4.1 and 4.2. The illuminated area percentage corresponds

to the fraction of pulse energy that penetrated through the canopy to the ground.

Table 4.7 Canopy reflectance derived from below-canopy echo responses and illuminated area on the below-canopy radiometric calibration target as a percentage of the footprint area at nadir.

Channel	Target hit	Canopy reflectance, ρ_1	First echo backscatter	Intermediate echo backscatter	Illuminated area on the target, % $\frac{A_2}{A_0}$
C1	1	8.5%	6.0%	2.5%	1%
	2	12.0%	12.0%		64%
	3	12.1%	9.7%	2.4%	3%
	4	18.1%	12.1%	6.0%	29%
	5	11.4%	3.9%	7.5%	57%
C2	1	21.8%	21.8%		54%
C3	1	2.6%	1.3%	1.3%	11%
	2	2.2%	2.2%		8%
	3	2.4%	1.3%	1.1%	20%
	4	3.1%	3.1%		18%
	5	1.4%	1.4%		27%
	6	1.9%	1.9%		29%

From the lifted target experiment we see that the simple algorithm from

Equation 4.1 does not work – we observed losses of 14.3%, 15.2%, and 23.1% for

channels C1, C2, and C3 respectively (Table 4.5). Moreover, from the single returns

from the below-canopy target, we observed small losses of 3% and 5% for channels C1

and C2 and a dramatic loss of 68% for channel C3. These results, besides the 68% loss

in C3 channel, are comparable with the reported losses between 5% and 15% by (Korpela, 2017). However, even though 68% loss for C3 was observed only in case of one hit, it may be due to underestimates of canopy radiant energy losses in the green wavelength region.

On the other hand, estimates of canopy reflectance from Equation 4.1, obtained from split pulse returns which hit the below-canopy target are all in the range derived from the single echo returns. For C1 channel, values of reflectance from 8.5% to 18.1% (Table 4.7) were obtained and these values are inside the range of the histogram for C1 on Figure 4.4. There is only one observation for channel C2 resulting in a reflectance value of 21.8% and six observations for the channel C2 with the values of reflectance from 1.4% to 3.1%. Both channel C2 and C3 results are also inside the range of reflectance values obtained from single returns (Table 4.7 and Figure 4.4).

One may expect, that the values, obtained from split returns are more likely to be higher than values obtained from single returns, because they account for a transparent part of the signal. Without accounting for volumetric scattering and additional losses through the canopy, reflectance values derived from split returns with Equation 4.1 ideally should approach values from the ASD measurements of canopy elements such as branches or stacks of needles (Table 4.4). However, it appears not to be the case in the experiment. Probably, it is the volumetric nature of the echo backscatter which plays an additional role in lowering absolute values of reflectance.

4.3.5 Vertical Spectral Vegetation Indices profiles of the Lodgepole Pine plot

Top and side view of the LP plot single echoes derived from the pseudo-reflectance values are shown in Figures 4.5 for each channel.
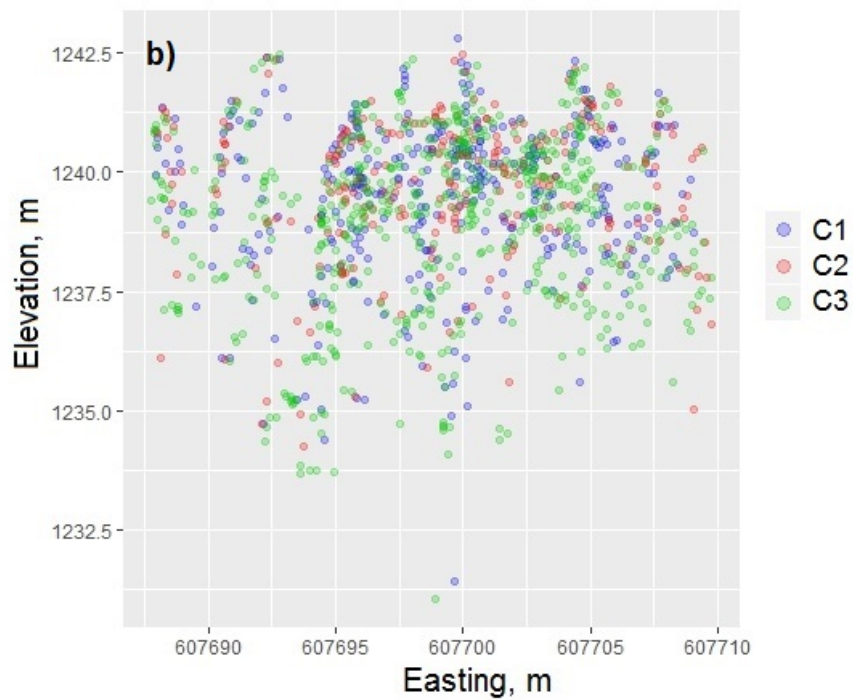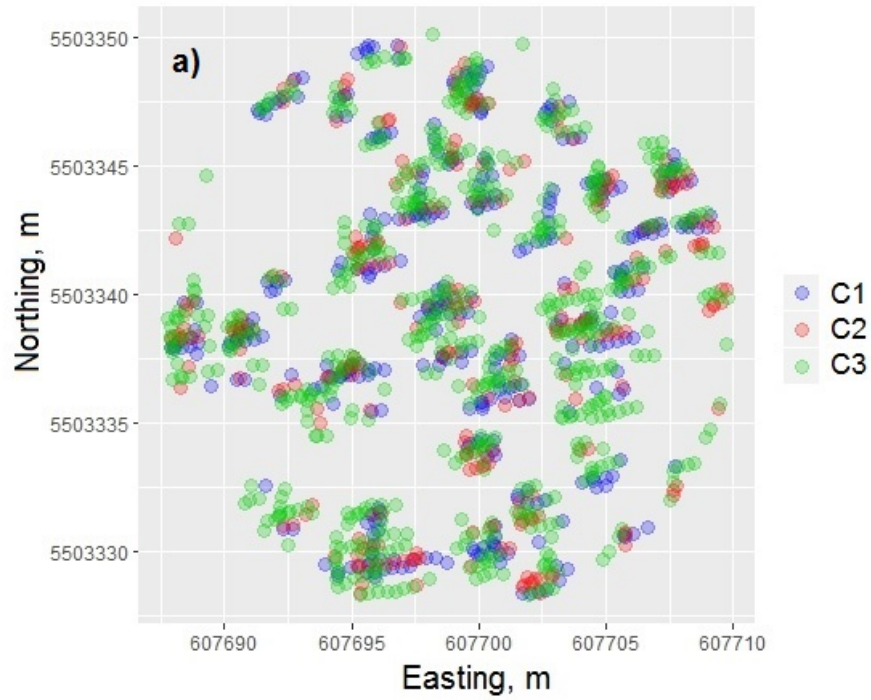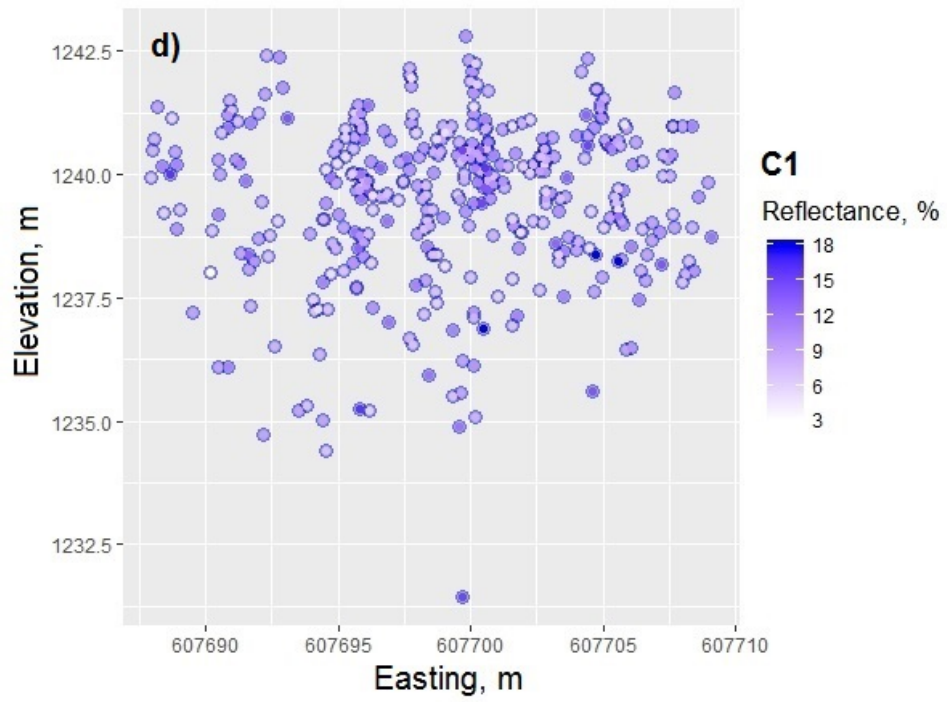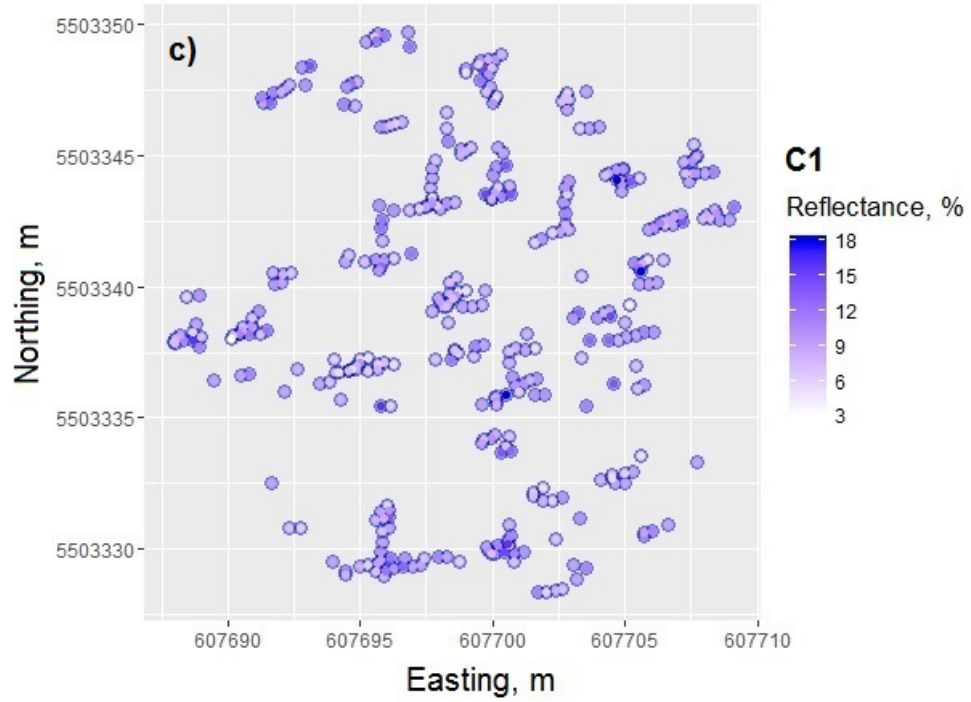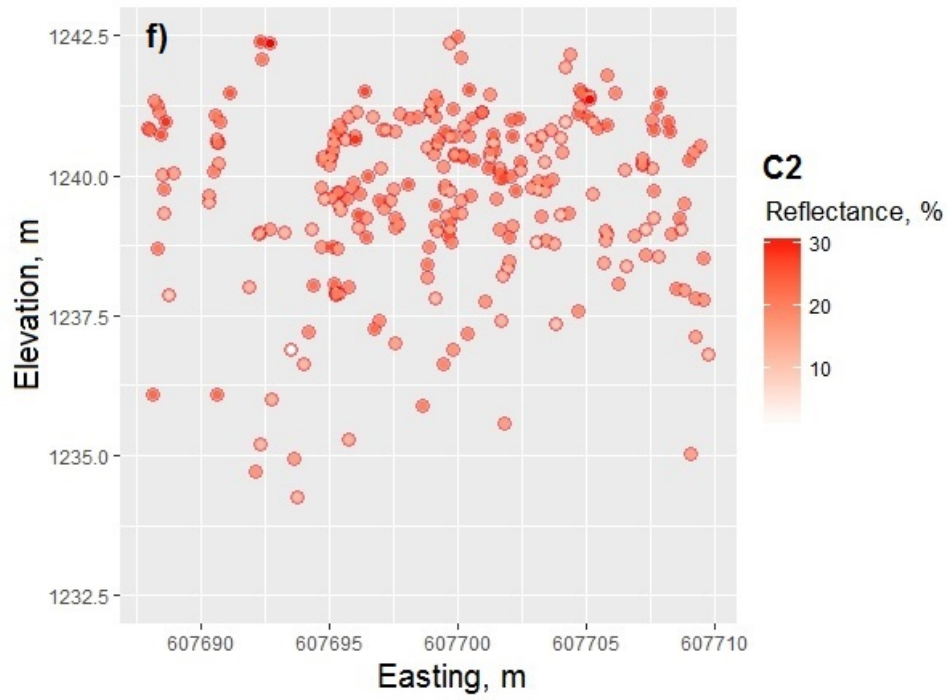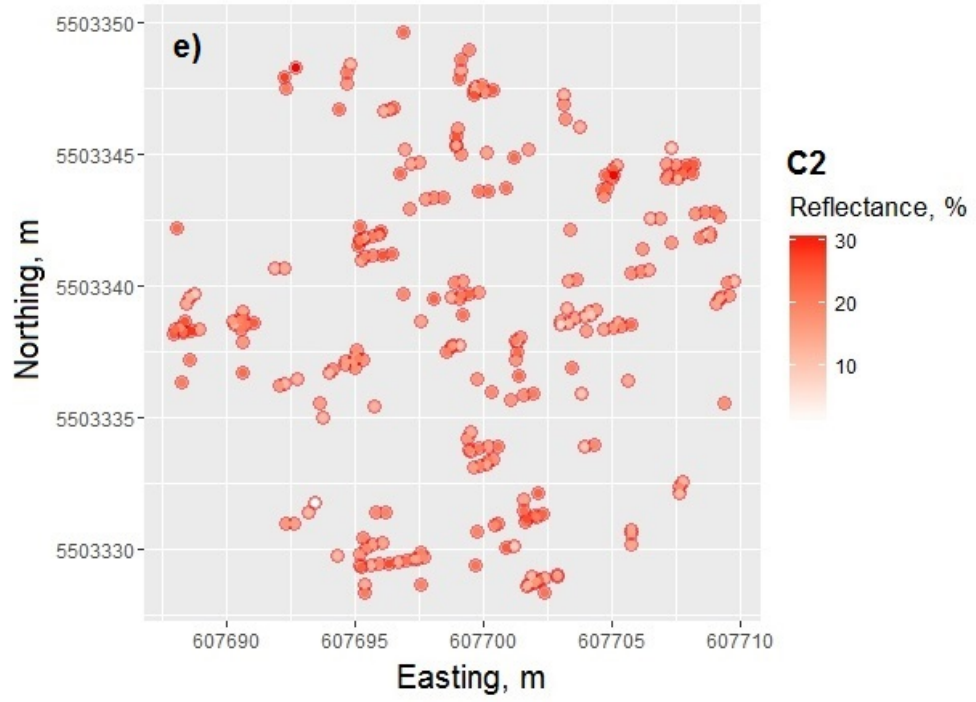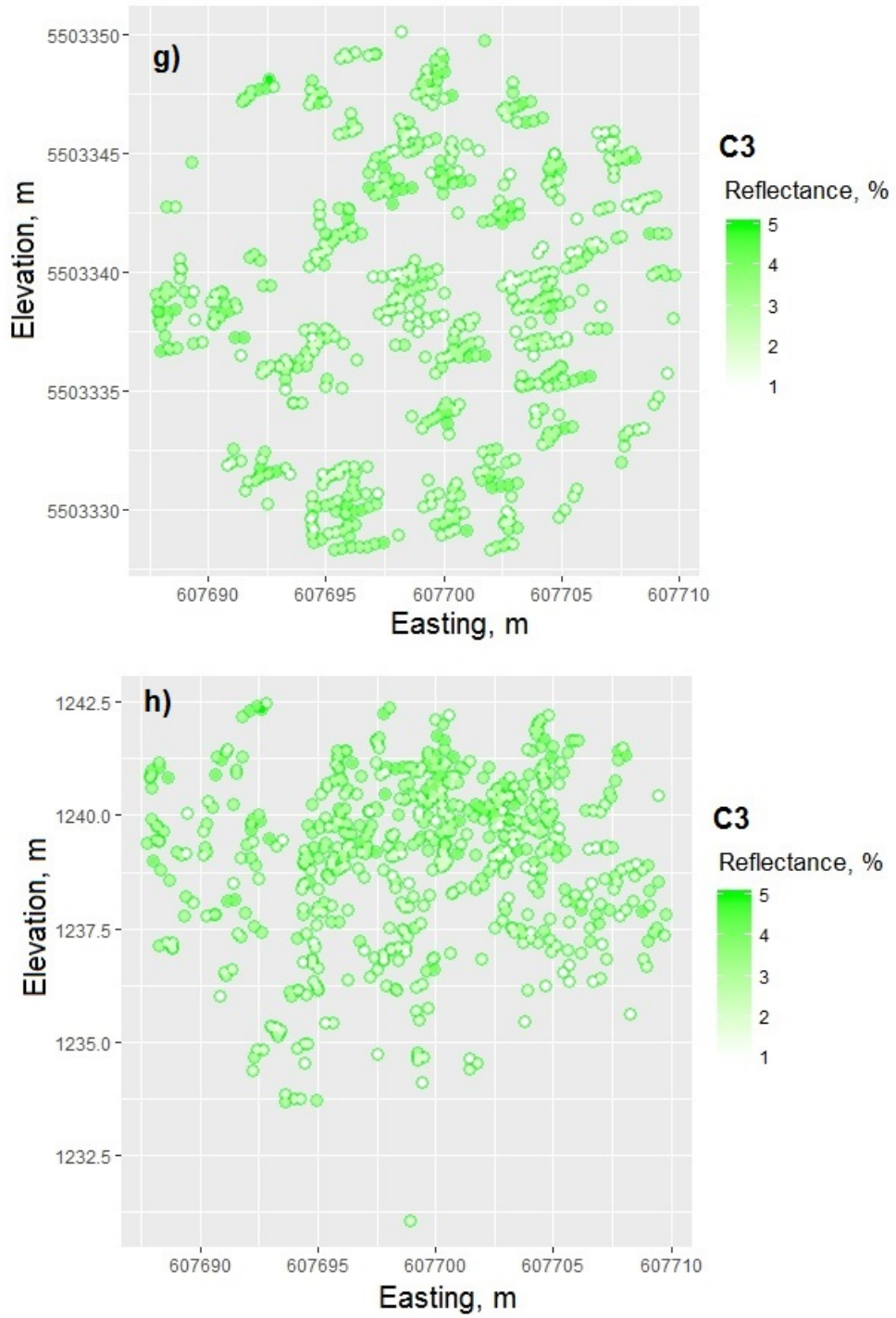
Figure 4.5 a) and b) All channel single echoes for the LP plot canopy combined in one image without intensity information. c)-h) Single-echo intensities coded with color for the LP plot canopy for all three channels.

Height distribution histograms and their kernel densities for each channel for the LP plot are presented in Figure 4.6. Table 4.8 shows results of Kolmogorov-Smirnov tests for two types of height distribution – one with a cut at 10 m above ground, and the second one – with a cut at 19 m above ground.
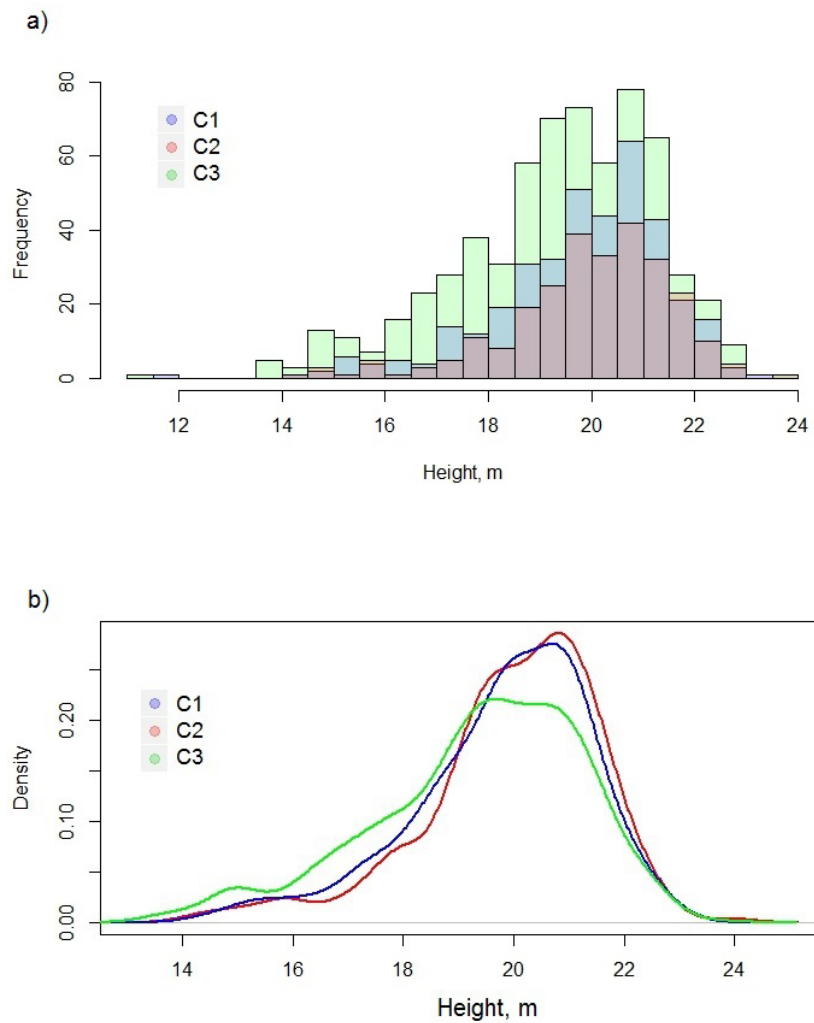
Figure 4.6 Histograms of height distribution of single echoes for C1, C2, and C3 over LP plot (a), and corresponding kernel densities (b).

Table 4.8 Results of KS test – D value (p-value in brackets) - for echoes higher than 10 m above ground (in the upper-right part), and echoes higher than 19 m above ground (in the bottom-left part).

	C1	C2	C3
C1	0 (1.0)	0.068 (0.46)	0.138(< 0.01)
C2	0.053 (0.89)	0 (1.0)	0.173 (< 0.01)
C3	0.085 (0.19)	0.081 (0.33)	0 (1.0)

From Figures 4.5 and 4.6, it can be seen that there are more single returns from the canopy from the C3 channel in comparison to C2 and C1 channels. It is clear from the kernel density of height distributions for single echoes higher than 10 m above ground on Figure 4.6b, that C3 channel samples different parts of the canopy compared with C1 and C2 channels (p values < 0.01 in Kolmogorov-Smirnov test, Table 4.8). In contrast, C1 and C2 channel distributions look more alike, and the Kolmogorov-Smirnov test gives small D value (0.068) with corresponding large value of p (0.46) failing to reject the hypothesis that C1 and C2 channels sampled the same population (canopy). These results corroborate similar observations reported in (Hopkinson et al., 2016). In addition, results from the below-canopy target experiment also show higher losses for the C3 channel in comparison with the C1 and C2 channels (Table 4.6). However, for single echoes which are higher than 19 m above ground, all three pairs C1 vs C2, C2 vs C3, and C1 vs C3, fail to reject the null hypothesis in the Kolmogorov-Smirnov test – p values 0.89, 0.33, and 0.19. Thus, we can establish that constructing vertical spectral vegetation indices profiles may be feasible for the pair C1C2 channels through the whole vertical profile, and for pairs C2C3 and C1C3,

only for the upper foliage elements of the vegetation canopy (the top 4 meters in the

plot used in this study, for canopy between 19m and 23 m height). In addition,

Figure 4.5a illustrates potential for individual tree delineation based on spatial

information only, showing obvious visible clustering patterns coincident with

individual tree locations.

Vertical profiles of normalized differences for the LP plot canopy with the

0.5 m height bins are shown in Figure 4.7. Profiles start at 14 m above ground

because there are insufficient single echo returns (Figure 4.7a) to derive indices

below this canopy height.
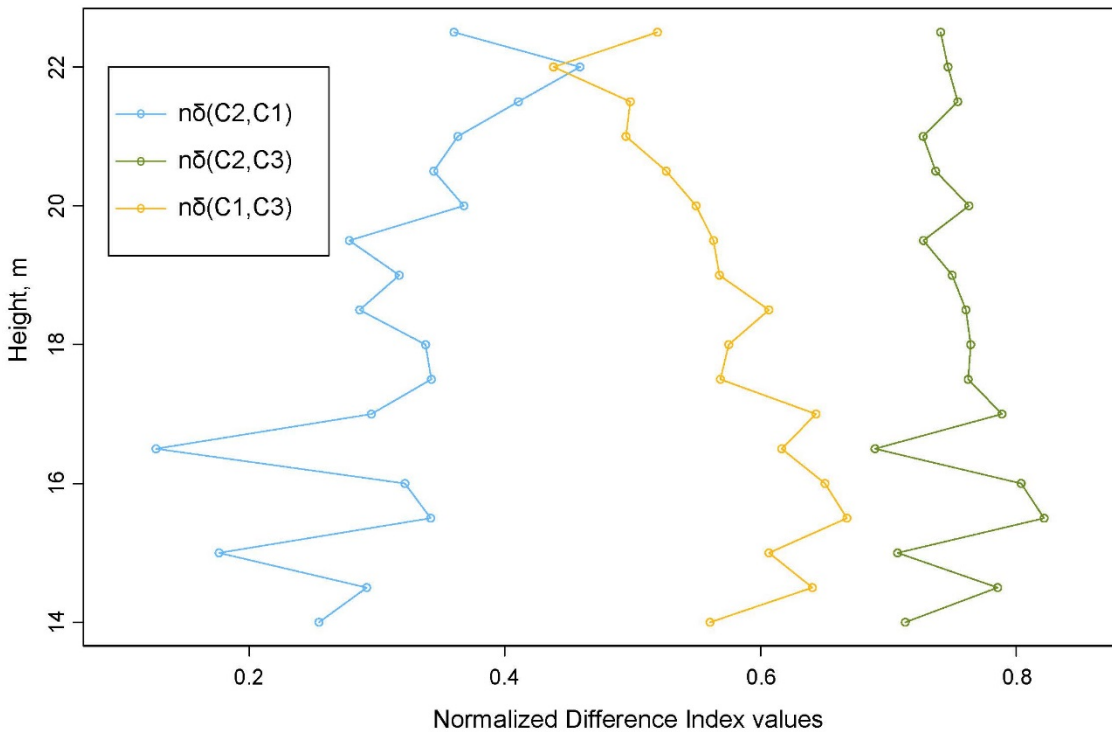
Figure 4.7 Lodgepole Pine plot canopy vertical SVIs derived from pseudo-reflectance values.

From Figure 4.7, it can be seen that all three indices become noisy below a height of 18 m due to decreasing single return counts. The lower voxel elements in two out of three indices are also noisy for the same reason. Also, the nδ(1064nm, 532nm) is almost constant through the canopy; in contrast, nδ(1064nm, 1500nm) and nδ(1550nm, 532nm) have clear trends. The decrease of the water index nδ(1064nm, 1500nm) with distance from the top of the canopy might be linked to the evapotranspiration characteristics of the vegetation and requires further investigation. The third index nδ(1550nm, 532nm) resembles the combined behavior of the first two indices because it can be re-written as their combination. The resulting nδ(1064nm, 532nm) on Figure 4.7 is comparable with the modeled response of ms lidar in (Morsdorf et al., 2009) and lab measurement results in (Woodhouse et al., 2011).

4.3.6 Maps and vertical profile of Spectral Vegetation Indices

The map of the ground-level nδ(1064nm, 1500nm) in Figure 4.8a shows distinct patterns across the surface (lower values of the index). When compared to the DTM (Figure 4.8b) and TPI (Figure 4.8c), it illustrates some visible spatial correspondence with hills and local valleys (R = -0.35, Pearson correlation coefficient for the TPI map). The canopy nδ(1064nm, 1500nm) map on Figure 4.8d exhibits higher values than the ground map (mean values 0.36 and 0.15) and there is an interesting pattern of higher values along the road between hills with younger vegetation. The nδ(1064nm, 532nm) map of the canopy (Figure 4.8d) shows relatively

high values (mean 0.75) across the whole map with the distinct area of higher values

in the eastern part depicting a hill with young aspen stands. Also, the same pattern of

higher values along the road can be traced following the pattern on Figure 4.8e map.
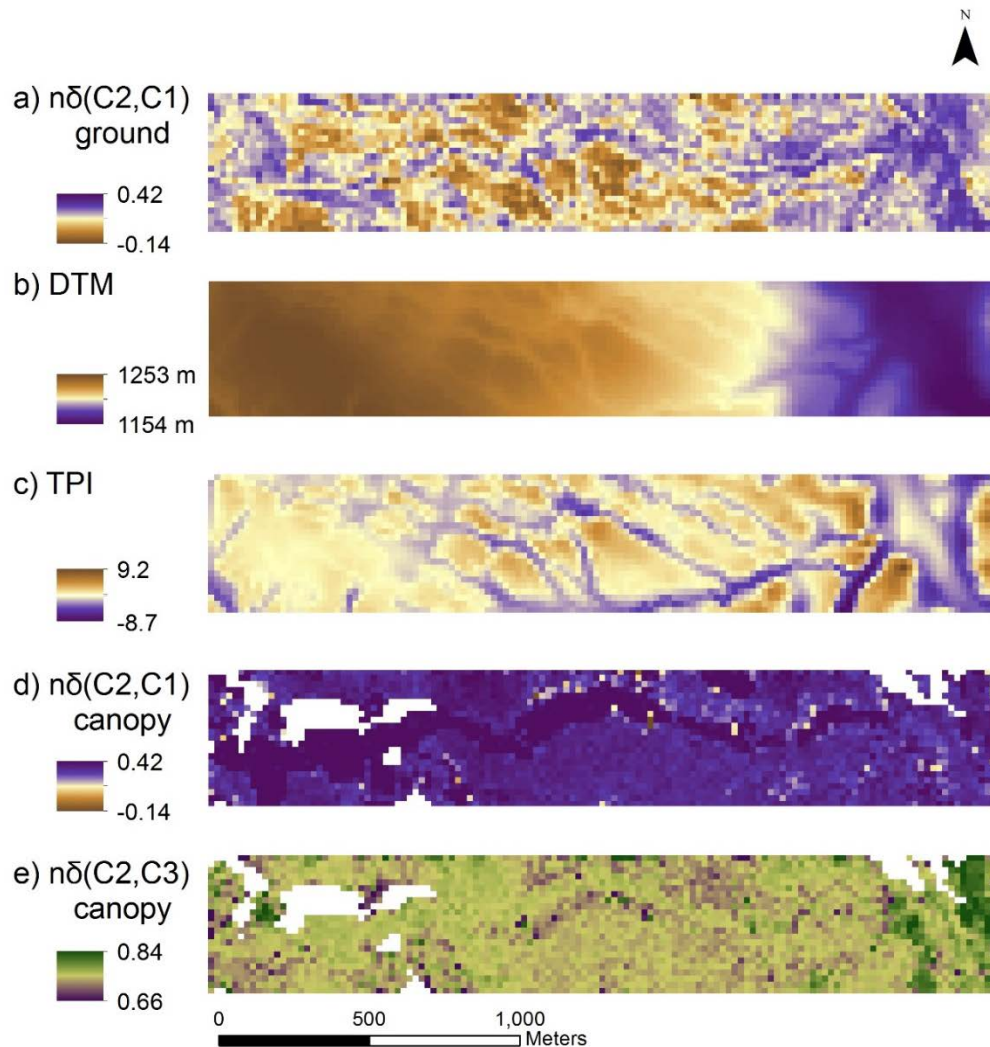
Figure 4.8 AOI maps of a) ground nδ(C2,C1), b) DTM (Digital Terrain Model), c) TPI (Topographic Position Index) , d) canopy nδ(C2,C1), and e) canopy nδ(C2,C3).

a) CHM

b) Vertical nδ(C2,C1) profile
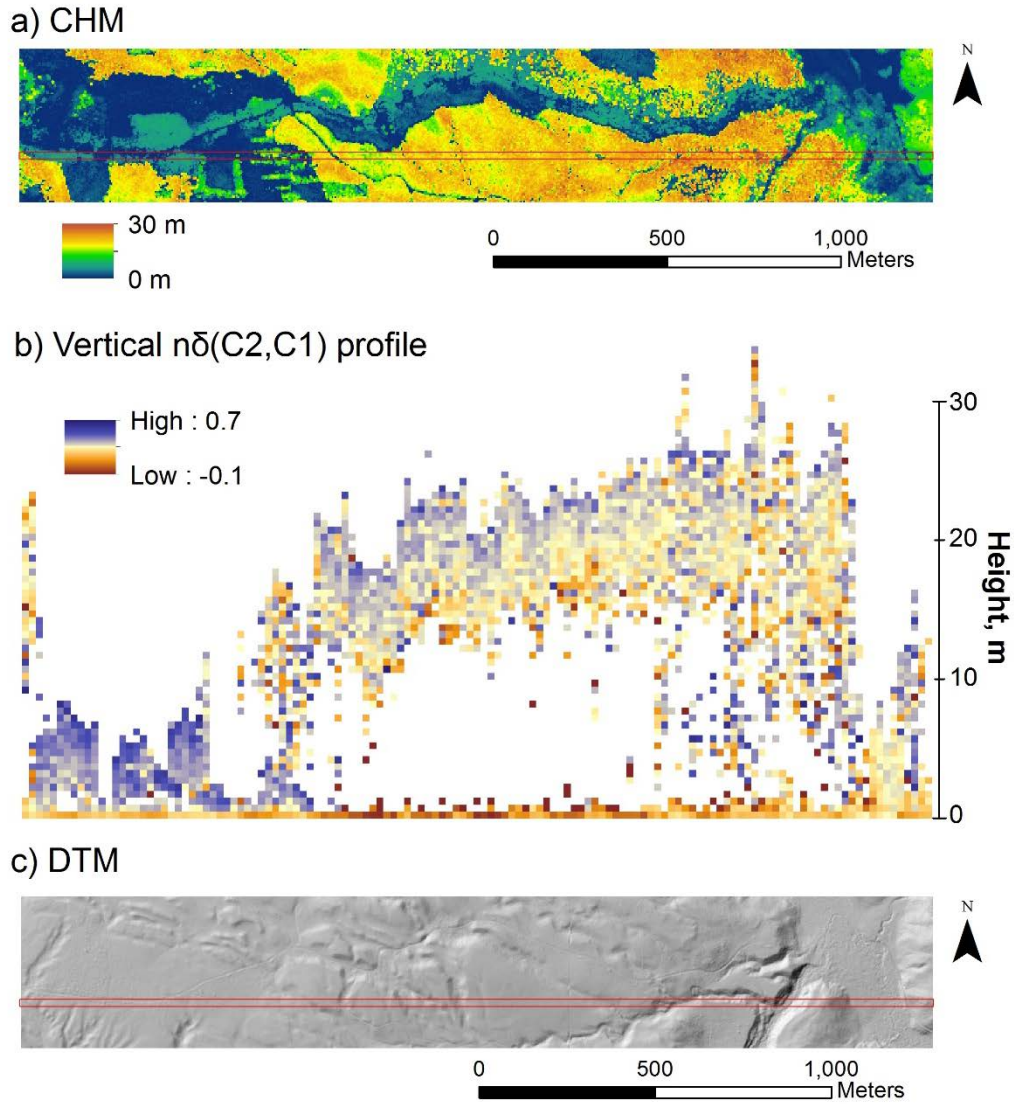
c) DTM

Figure 4.9 a) - Canopy Height Model (CHM) with a cross-section (shown in red) used to calculate vertical nδ(C2,C1); b) - Vertical nδ(C2,C1) profile, height is scaled 40x in comparison to Easting; c) – DTM with a cross-section (shown in red) used to calculate vertical nδ(C2,C1) profile presented in b).

The vertical profile map of nδ(1064nm, 1500nm) on Figure 4.9b shows a distinct gradient of the index through the canopy. Moreover, the map helps to catch the difference in index values and its gradient between younger stands (western part of the transect), mature LP stands (central part of the transect), and the diverse

121

understory on the steep hills near the wetland area (eastern part of the transect). Thus, the vertical profile map on Figure 4.9b illustrates the potential of the plot level voxel approach in the 3D mapping of active spectral vegetation indices.

4.4   Conclusions

Radiometric calibration targets help bridge the gap between ms lidar products and available spectral signature libraries. Low-cost diffuse reflecting coating (Noble's coating) is an acceptable operational substitute to Spectralon® panels allowing investigation of complex lidar backscatter without being cost-prohibitive and also allows custom calibration targets. The algorithm described by Equation 4.1, is promising; however, it should be combined with an additional model of energy losses in the canopy, and an explanation of the results of the lifted target experiment may be a first step in creating such a model. Vertical SVIs for the canopy can be calculated from corrected Titan DNs up to a certain penetration depth – in our study plot up to 4m. Canopy vertical profile of normalized difference of C2 and C3 channels in case of an LP plot looks similar to predicted profiles of NDVI by modeling and lab measurements (Morsdorf et al., 2009; Woodhouse et al., 2011). It is possible to derive vertical profiles of the normalized difference of C1 and C2 channels of the Titan sensor from the top of the canopy to the ground, providing enough single echoes, and the obtained spatial distribution of ground values for $n\delta(1064nm, 1550nm)$ coincides with local morphology. Potential of the plot level voxel approach in the 3D mapping of active spectral vegetation indices was illustrated with vertical profile $n\delta(1064nm, 1550nm)$ map of a transect across AOI.

Future work should include development of recipes for coatings with lower reflectance values, down to 1%. Targets covered with such a coating would allow the prediction of receiver response to low values of lidar backscatter and enable modeling of sensor SNR for analyzing volumetric backscatter of the canopy. Additional analysis of energy losses in the lifted target experiment may help to understand signal attenuation in canopy foliage and allow derivation of reflectance and estimation of illuminated areas from split returns. The new methodology of constructing voxel-based active 3D SVIs on a stand level brings new potential to classification, comparison, and change monitoring in forest environments. However, to be able to compare active 3D SVIs through time and space, more research is needed into standardization. In addition, segmentation of the lidar point cloud from the forest stand into individual trees (Okhrimenko & Grabarnik, 2016), if successful, could provide a means to construct vertical SVI profiles for each detected tree allowing the enhancement of species classification and forest health monitoring with ms lidar.

5   Conclusions

5.1   Main results

In Chapter II, an algorithm for *in situ* bathymetric correction of lidar returns was presented which does not require trajectory information from the sensor. Although the resulting correction is less precise than the conventional one (introduced inaccuracy is up to 2 cm in height and up to 15 cm in plane for 1 m of water depth), it is still close to lidar point-level accuracy (4 cm in height and 7 cm in plane) for shallow river channels with depth below 2 m. This algorithm may be presented in a quality assurance perspective - by creating two surfaces corresponding to zero and maximum scan angles, the end-user may, in some cases, use this approach to validate the more precise bathymetric correction provided by the vendor.

A semi-automated bathymetric correction routine was proposed, the key component of which is the automated generation of a virtual digital water surface. Application of this routine provided more favorable results compared to the vendor`s OTS (off-the-shelf) correction when applied to the complex urban river environment in the Calgary case study. In addition, water surface variations of up to 80 cm were observed across two channels of the river around a small island, illustrating that the assumption of a flat water surface is not viable for bathymetric correction in dynamic river environments. The depth performance assessment of the sensor confirmed specification values and stressed a need for a prediction algorithm based on readily accessible data such as water clarity measured in NTU.

In Chapter III it was shown, that atmospheric correction is needed to compare intensity DN values at different altitudes and it also became clear that the survey at 1500 m AGL with the Titan sensor does not provide enough lidar backscatter for C3 over vegetated areas and thus is not recommended. The altitude threshold criterion was introduced which, in an operational context, may bring better comparability across datasets. It was demonstrated that SVIs derived from single echoes are more consistent across three altitudes over vegetated areas in comparison to SVIs derived from all echoes. This led to the conclusion that single-echo intensities have greater potential for constructing consistent active spectral indices. After comparing two families of spectral indices – simple ratios ($s\rho$) and normalized differences ($n\delta$) – it was recommended to use a combination of $n\delta(C2,C3)$, $n\delta(C1,C3)$ and $s\rho(C2,C1)$ indices for classification because of the improved consistency in these indices across three altitudes.

In Chapter IV it was shown, that a low-cost diffuse reflecting coating (Noble's coating (Noble et al., 2008)) is an acceptable operational substitute to Spectralon® panels for radiometric calibration and allows investigation of complex lidar backscatter without being cost-prohibitive. It was demonstrated that reflectance derived from ms lidar intensity DNs is close to reflectance obtained with AVIRIS hyperspectral sensor (R. F. Kokaly et al., 2003) and concluded that radiometric calibration targets help bridge the gap between ms lidar products and available spectral signature libraries.

Plot level single-echo height distributions were analyzed and it was found that for the pairs of channels (C2,C3) and (C1,C3), vertical SVIs for the canopy can be calculated from corrected Titan DNs, only up to a certain penetration depth – in the case of the study plot for up to 4m; for the (C2,C1) pair of channels, it was established that a vertical SVI profile for the Titan sensor can be calculated from the top of the canopy to the ground - similar behaviour for these two channels was reported in (Hopkinson et al., 2016). It was demonstrated that a map of normalized difference from channels C1 and C2 ($n\delta_{1550nm}^{1064nm}$) – sometimes referred as WI (water index) – constructed from the ground and close to the ground (up to 0.5 m) echoes coincides with local terrain morphology. It was shown that calculated plot-level canopy C2 and C3 vertical normalized difference ($n\delta_{532nm}^{1064nm}$) profile – NDVI analog of ms lidar spectral indices - resembles vertical NDVI profiles obtained by modelling (Morsdorf et al., 2009; Woodhouse et al., 2011). A potential of the plot-level voxel approach in the 3D mapping of active spectral vegetation indices was illustrated with the vertical profile $n\delta_{1550nm}^{1064nm}$ map of a transect across the Cypress Hills AOI (Figure 4.9).

The experiment with complex radiometric targets – a lifted target, and a below-canopy target – described in Chapter IV, demonstrated that lidar signal attenuation in the canopy is still poorly understood. The observations do not support the distributive property of the signal encountering the transparent target, something that is expected from a transparent target cross-section because of the linear dependence of intensity on power in the case of flat continuous targets. Moreover, a 68% loss in intensity of the C3 channel single-echo was observed from

the below-tree target. This amount is more than four times larger than results reported in (Korpela, 2017) and suggest some limitations of the methodology proposed by (Milenkovic et al., 2017). Also, it was expected that the reflectance values derived with Equation 4.1 for canopy echoes from pulses which hit the below-tree target would be higher than values obtained from the single echoes. However, the obtained values were in the range of values calculated from the single echoes.

The main implication of the Chapter IV findings is the recommendation to use radiometric calibration targets in ms lidar acquisition campaigns. Resulting radiometric calibration of the intensity data will allow for better comparison of ms lidar spectral products with data from other sensors and/or through time and space. This, in turn, should produce more comparable land cover classification leading to more reliable monitoring and more accurate change detection. In addition, the presented methodology of constructing vertical $n\delta_{1550nm}^{1064nm}$ profiles can be tested in wetland detection and classification in various landscapes, especially in most challenging boreal 'Green' zones in which this task is confounded by vegetation cover.

5.2 Future work

Further research is proposed in four areas: bathymetry, atmospheric correction, analysis of the signal attenuation from the sub-footprint targets, and individual tree vertical SVI profiles.

5.2.1   Bathymetry

It is expected that data fusion with passive imagery will allow for the prediction of depth performance of the system in a given mission, and may help to distinguish volumetric returns from waterbed returns. Data fusion may also provide a way of extrapolating the lidar-derived waterbed to areas where actual bathymetric data are absent. While bathymetry based on passive imagery tone analysis has been introduced and tested intensively (Legleiter, 2012; Legleiter, Roberts, & Lawrence, 2009), there are recent reports on applying image matching algorithms from RGB and hyperspectral images to create a point cloud of a water bed in clear mountain creeks (Dietrich, 2017; Woodget, Carbonneau, Visser, & Maddock, 2015). It appears that bathymetry belongs to the domain of complex remote sensing tasks and different approaches may add to each other and create a synergistic effect. Multispectral lidar, combined with an RGB camera and a full waveform digitizer for a green channel provides a tremendous amount of information and it is clear that more advanced algorithms may be developed, potentially, based on Bayesian networks or machine-learning algorithms, and combined with an intensive usage of known *a priori* information, such as contemporary regional hydrology GIS.

5.2.2   Atmospheric correction

Based on (Sabatini & Richardson, 2013), it is expected that atmospheric correction over significantly different altitudes works better if it is assumed that the extinction coefficient in the Bouguer–Lambert–Beer`s law is linearly dependent on altitude, rather than a constant extinction coefficient. Consequently, radiometric

targets will allow experimental derivation of the extinction coefficient of atmospheric losses; provided enough altitude strata, the dependence of extinction coefficients on altitude can be investigated. This work is of prime interest in mountainous terrains, such as the West Castle Watershed, where atmospheric losses are a substantial part of radiometric calibration for ms lidar intensity data. Subsequently, vertical spectral indices can be constructed for further analysis of areas with significant elevation gradients.

5.2.3   Attenuation losses in the canopy

Future work should include development of recipes for coatings with lower reflectance values, down to 5%. Targets covered with such a coating would allow the prediction of receiver response to low values of lidar backscatter and enable modeling of sensor SNR for analyzing volumetric backscatter of the canopy. Additional analysis of energy losses in the lifted target experiment may help to understand signal attenuation in canopy foliage and allow derivation of reflectance and estimation of illuminated areas from split returns.

5.2.4   Vertical Spectral Vegetation Indices

Segmentation of the lidar point cloud from the forest stand into individual trees (Okhrimenko & Grabarnik, 2016), if successful, should provide a means to construct vertical SVI profiles for each detected tree, thereby enhancing all aspects of current forest monitoring with ms lidar.

References

ANSI. (2007). **Z136.1-2007**. In *Safe Use of Lasers* (pp. 276): American National Standard Institute.

Axelsson, P. E. (1999). Processing of laser scanner data - algorithms and applications. *Isprs Journal of Photogrammetry and Remote Sensing, 54*(2-3), 138-147. doi:Doi 10.1016/S0924-2716(99)00008-8

Baltsavias, E. P. (1999a). Airborne laser scanning: basic relations and formulas. *Isprs Journal of Photogrammetry and Remote Sensing, 54*(2-3), 199-214. doi:Doi 10.1016/S0924-2716(99)00015-5

Baltsavias, E. P. (1999b). Airborne laser scanning: existing systems and firms and other resources. *Isprs Journal of Photogrammetry and Remote Sensing, 54*(2-3), 164-198. doi:Doi 10.1016/S0924-2716(99)00016-7

Bannari, A., Morin, D., Bonn, F., & Huete, A. R. (1995). A review of vegetation indices. *Remote Sensing Reviews, 13*(1-2), 95-120. doi:10.1080/02757259509532298

Baret, F., & Guyot, G. (1991). Potentials and Limits of Vegetation Indexes for Lai and Apar Assessment. *Remote Sensing of Environment, 35*(2-3), 161-173. doi:Doi 10.1016/0034-4257(91)90009-U

Bater, C. W., Coops, N. C., Gergel, S. E., LeMay, V., & Collins, D. (2009). Estimation of standing dead tree class distributions in northwest coastal forests using lidar remote sensing. *Canadian Journal of Forest Research-Revue Canadienne De Recherche Forestiere, 39*(6), 1080-1091. doi:10.1139/X09-030

Beaty, C. B. (1975). *The Landscapes of Southern Alberta.* Lethbridge, Alberta: The University of Lethbridge.

Blanckaert, K., Kleinhans, M. G., McLelland, S. J., Uijttewaal, W. S. J., Murphy, B. J., van de Kruijs, A., . . . Chen, Q. W. (2013). Flow separation at the inner (convex) and outer (concave) banks of constant-width and widening open-channel bends. *Earth Surface Processes and Landforms, 38*(7), 696-716. doi:10.1002/esp.3324

Budei, B. C., St-Onge, B., Hopkinson, C., & Audet, F. A. (2018). Identifying the genus or species of individual trees using a three-wavelength airborne lidar system. *Remote Sensing of Environment, 204*, 632-647. doi:10.1016/j.rse.2017.09.037

Calgary. (2016). Retrieved 01.11.2016, from City of Calgary https://data.calgary.ca/Environment/Hydrology/a2cn-dxht

Chasmer, L. E., Hopkinson, C. D., Petrone, R. M., & Sitar, M. (2017). Using Multitemporal and Multispectral Airborne Lidar to Assess Depth of Peat Loss and Correspondence With a New Active Normalized Burn Ratio for Wildfires. *Geophysical Research Letters, 44*(23), 11851-11859. doi:10.1002/2017gl075488

CSRS. (2017). PPP service. Retrieved from
https://webapp.geod.nrcan.gc.ca/geod/tools-outils/ppp.php?locale=en

Davies-Colley, R. J., & Nagels, J. W. (2008). Predicting light penetration into river waters. *Journal of Geophysical Research-Biogeosciences, 113*(G3). doi:10.1029/2008jg000722

Davies-Colley, R. J., & Smith, D. G. (2001). Turbidity, suspended sediment, and water clarity: A review. *Journal of the American Water Resources Association, 37*(5), 1085-1101. doi:DOI 10.1111/j.1752-1688.2001.tb03624.x

Dietrich, J. T. (2017). Bathymetric Structure-from-Motion: extracting shallow stream bathymetry from multi-view stereo photogrammetry. *Earth Surface Processes and Landforms, 42*(2), 355-364. doi:10.1002/esp.4060

Dogliotti, A., Ruddick, K. G., Nechad, B., Doxaran, D., & Knaeps, E. (2015). A single algorithm to retrieve turbidity from remotely-sensed data in all coastal and estuarine waters. *Remote Sensing of Environment, 156*, 157-168. doi:10.1016/j.rse.2014.09.020

Donoghue, D. N. M., Watt, P. J., Cox, N. J., & Wilson, J. (2007). Remote sensing of species mixtures in conifer plantations using LiDAR height and intensity data. *Remote Sensing of Environment, 110*(4), 509-522. doi:10.1016/j.rse.2007.02.032

Dutta, D., Herath, S., & Musiake, K. (2006). An application of a flood risk analysis system for impact analysis of a flood control plan in a river basin. *Hydrological Processes, 20*(6), 1365-1384. doi:10.1002/hyp.6092

Environment-Canada. (2016). Water level data. Retrieved 01.11.2016 https://wateroffice.ec.gc.ca/report/real_time_e.html?stn=05BH004

Fernandez-Diaz, J. C., Carter, W. E., Glennie, C., Shrestha, R. L., Pan, Z., Ekhtari, N., . . . Sartori, M. (2016). Capability Assessment and Performance Metrics for the Titan Multispectral Mapping Lidar. *Remote Sensing, 8*(11). doi:10.3390/rs8110936

Fernandez-Diaz, J. C., Glennie, C. L., Carter, W. E., Shrestha, R. L., Sartori, M. P., Singhania, A., . . . Overstreet, B. T. (2014). Early Results of Simultaneous Terrain and Shallow Water Bathymetry Mapping Using a Single-Wavelength Airborne LiDAR Sensor. *Ieee Journal of Selected Topics in Applied Earth Observations and Remote Sensing, 7*(2), 623-635. doi:10.1109/Jstars.2013.2265255

Friess, P. (1989). Empirical Accuracy of Positions Computed from Airborne GPS Data. In L. K. & H. U. (Eds.), *High Precision Navigation.*: Springer, Berlin, Heidelberg.

Gamon, J. A., Penuelas, J., & Field, C. B. (1992). A Narrow-Waveband Spectral Index That Tracks Diurnal Changes in Photosynthetic Efficiency. *Remote Sensing of Environment, 41*(1), 35-44. doi:Doi 10.1016/0034-4257(92)90059-S

Gamon, J. A., Serrano, L., & Surfus, J. S. (1997). The photochemical reflectance index: an optical indicator of photosynthetic radiation use efficiency across species, functional types, and nutrient levels. *Oecologia, 112*(4), 492-501. doi:DOI 10.1007/s004420050337

Garcia, M., Riano, D., Chuvieco, E., & Danson, F. M. (2010). Estimating biomass carbon stocks for a Mediterranean forest in central Spain using LiDAR height and intensity data. *Remote Sensing of Environment, 114*(4), 816-830. doi:10.1016/j.rse.2009.11.021

Gates, D. M., Keegan, H. J., Schleter, J. C., & Weidner, V. R. (1965). Spectral Properties of Plants. *Applied Optics, 4*(1), 11-&. doi:Doi 10.1364/Ao.4.000011

Gaulton, R., Danson, F. M., Ramirez, F. A., & Gunawan, O. (2013). The potential of dual-wavelength laser scanning for estimating vegetation moisture content. *Remote Sensing of Environment, 132*, 32-39. doi:10.1016/j.rse.2013.01.001

Glennie, C. L., Carter, W. E., Shrestha, R. L., & Dietrich, W. E. (2013). Geodetic imaging with airborne LiDAR: the Earth's surface revealed. *Reports on Progress in Physics, 76*(8). doi:10.1088/0034-4885/76/8/086801

Gordon, H. R. (1989). Can the Lambert-Beer Law Be Applied to the Diffuse Attenuation Coefficient of Ocean Water. *Limnology and Oceanography, 34*(8), 1389-1409. doi:DOI 10.4319/lo.1989.34.8.1389

Gordon, H. R., Brown, O. B., & Jacobs, M. M. (1975). Computed Relationships between Inherent and Apparent Optical-Properties of a Flat Homogeneous Ocean. *Applied Optics, 14*(2), 417-427. doi:Doi 10.1364/Ao.14.000417

Govaerts, Y. M., Jacquemoud, S., Verstraete, M. M., & Ustin, S. L. (1996). Three-dimensional radiation transfer modeling in a dicotyledon leaf. *Applied Optics, 35*(33), 6585-6598. doi:Doi 10.1364/Ao.35.006585

Grunthal, G., Thieken, A. H., Schwarz, J., Radtke, K. S., Smolka, A., & Merz, B. (2006). Comparative risk assessments for the city of Cologne - Storms, floods, earthquakes. *Natural Hazards, 38*(1-2), 21-44. doi:10.1007/s11069-005-8598-0

Guenther, G. C., Brooks, M. W., & LaRocque, P. E. (2000). New capabilities of the "SHOALS" airborne lidar bathymeter. *Remote Sensing of Environment, 73*(2), 247-255. doi:Doi 10.1016/S0034-4257(00)00099-7

Guenther, G. C., Cunningham, A. G., LaRocque, P. E., & Reid, D. J. (2000). Meeting the Accuracy Challenge in Airborne Bathymetry. *NATIONAL OCEANIC ATMOSPHERIC ADMINISTRATION/NESDIS SILVER SPRING MD.*

Hakala, T., Nevalainen, O., Kaasalainen, S., & Makipaa, R. (2015). Technical Note: Multispectral lidar time series of pine canopy chlorophyll content. *Biogeosciences, 12*(5), 1629-1634. doi:10.5194/bg-12-1629-2015

Hancock, S., Gaulton, R., & Danson, F. M. (2017). Angular Reflectance of Leaves With a Dual-Wavelength Terrestrial Lidar and Its Implications for Leaf-Bark Separation and Leaf Moisture Estimation. *Ieee Transactions on Geoscience and Remote Sensing, 55*(6), 3084-3090. doi:10.1109/Tgrs.2017.2652140

Hancock, S., Lewis, P., Foster, M., Disney, M., & Muller, J. P. (2012). Measuring forests with dual wavelength lidar: A simulation study over topography. *Agricultural and Forest Meteorology, 161*, 123-133. doi:10.1016/j.agrformet.2012.03.014

Hardisky, M. A., Klemas, V., & Smart, R. M. (1983). The Influence of Soil-Salinity, Growth Form, and Leaf Moisture on the Spectral Radiance of Spartina-Alterniflora Canopies. *Photogrammetric Engineering and Remote Sensing, 49*(1), 77-83.

Hofton, M. A., Minster, J. B., & Blair, J. B. (2000). Decomposition of laser altimeter waveforms. *Ieee Transactions on Geoscience and Remote Sensing, 38*(4), 1989-1996. doi:Doi 10.1109/36.851780

Holmgren, J., Nilsson, M., & Olsson, H. (2003). Simulating the effects of lidar scanning angle for estimation of mean tree height and canopy closure. *Canadian Journal of Remote Sensing, 29*(5), 623-632. doi:DOI 10.5589/m03-030

Holmgren, J., & Persson, A. (2004). Identifying species of individual trees using airborne laser scanner. *Remote Sensing of Environment, 90*(4), 415-423. doi:10.1016/S0034-4257(03)00140-8

Hopkinson, C. (2007). The influence of flying altitude, beam divergence, and pulse repetition frequency on laser pulse return intensity and canopy frequency distribution. *Canadian Journal of Remote Sensing, 33*(4), 312-324. doi:DOI 10.5589/m07-029

Hopkinson, C., & Chasmer, L. (2009). Testing LiDAR models of fractional cover across multiple forest ecozones. *Remote Sensing of Environment, 113*(1), 275-288. doi:10.1016/j.rse.2008.09.012

Hopkinson, C., Chasmer, L., Gynan, C., Mahoney, C., & Sitar, M. (2016). Multisensor and Multispectral LiDAR Characterization and Classification of a Forest Environment. *Canadian Journal of Remote Sensing, 42*(5), 501-520. doi:10.1080/07038992.2016.1196584

Hopkinson, C., Chasmer, L., & Hall, R. J. (2008). The uncertainty in conifer plantation growth prediction from multi-temporal lidar datasets. *Remote Sensing of Environment, 112*(3), 1168-1180. doi:10.1016/j.rse.2007.07.020

Hopkinson, C., Crasto, N., Marsh, P., Forbes, D., & Lesack, L. (2011). Investigating the spatial distribution of water levels in the Mackenzie Delta using airborne LiDAR. *Hydrological Processes, 25*(19), 2995-3011. doi:10.1002/hyp.8167

Huete, A. R. (1987). Soil and Sun Angle Interactions on Partial Canopy Spectra. *International Journal of Remote Sensing, 8*(9), 1307-1317. doi:Doi 10.1080/01431168708954776

Hunt, E. R., & Rock, B. N. (1989). Detection of Changes in Leaf Water-Content Using near-Infrared and Middle-Infrared Reflectances. *Remote Sensing of Environment, 30*(1), 43-54. doi:Doi 10.1016/0034-4257(89)90046-1

Irish, J. L., & Lillycrop, W. J. (1999). Scanning laser mapping of the coastal zone: the SHOALS system. *Isprs Journal of Photogrammetry and Remote Sensing, 54*(2-3), 123-129. doi:Doi 10.1016/S0924-2716(99)00003-9

Isenburg, M. (2016). LAStools - efficient LiDAR processing software" (version 161029, academic), obtained from http://rapidlasso.com/LAStools.

Jackson, R. D., Slater, P. N., & Pinter, P. J. (1983). Discrimination of Growth and Water-Stress in Wheat by Various Vegetation Indexes through Clear and Turbid Atmospheres. *Remote Sensing of Environment, 13*(3), 187-208. doi:Doi 10.1016/0034-4257(83)90039-1

Jelalian, A. (1992). *Laser Radar Systems:* Artech House.

Kaasalainen, S., Hyyppa, H., Kukko, A., Litkey, P., Ahokas, E., Hyyppa, J., . . . Pyysalo, U. (2009). Radiometric Calibration of LIDAR Intensity With Commercially Available Reference Targets. *Ieee Transactions on Geoscience and Remote Sensing, 47*(2), 588-598. doi:10.1109/Tgrs.2008.2003351

Karila, K., Matikainen, L., Puttonen, E., & Hyyppa, J. (2017). Feasibility of Multispectral Airborne Laser Scanning Data for Road Mapping. *Ieee Geoscience and Remote Sensing Letters, 14*(3), 294-298. doi:10.1109/Lgrs.2016.2631261

Kashani, A. G., Olsen, M. J., Parrish, C. E., & Wilson, N. (2015). A Review of LIDAR Radiometric Processing: From Ad Hoc Intensity Correction to Rigorous Radiometric Calibration. *Sensors, 15*(11), 28099-28128. doi:10.3390/s151128099

Kokaly, R. F., Clark, R. N., Swayze, G. A., Livo, K. E., Hoefen, T. M., Pearson, N. C., . . . Klein, A. J. (2017a). Lodgepole-Pine LP-Needles-1. from USGS Spectral Library Version 7: U.S. Geological Survey Data Series 1035

Kokaly, R. F., Clark, R. N., Swayze, G. A., Livo, K. E., Hoefen, T. M., Pearson, N. C., . . . Klein, A. J. (2017b). Oak Oak-Leaf-1 fresh. from USGS Spectral Library Version 7: U.S. Geological Survey Data Series 1035

Kokaly, R. F., Despain, D. G., Clark, R. N., & Livo, K. E. (2003). Mapping vegetation in Yellowstone National Park using spectral feature analysis of AVIRIS data. *Remote Sensing of Environment, 84*(3), 437-456. doi:Doi 10.1016/S0034-4257(02)00133-5

Korpela, I. (2017). Acquisition and evaluation of radiometrically comparable multi-footprint airborne LiDAR data for forest remote sensing. *Remote Sensing of Environment, 194,* 414-423. doi:10.1016/j.rse.2016.10.052

Korpela, I., Orka, H. O., Maltamo, M., Tokola, T., & Hyyppa, J. (2010). Tree Species Classification Using Airborne LiDAR - Effects of Stand and Tree Parameters, Downsizing of Training Set, Intensity Normalization, and Sensor Type. *Silva Fennica, 44*(2), 319-339. doi:10.14214/sf.156

Korpela, I., Tuomola, T., Tokola, T., & Dahlin, B. (2008). Appraisal of Seedling Stand Vegetation with Airborne Imagery and Discrete-Return LiDAR - an Exploratory Analysis. *Silva Fennica, 42*(5), 753-772. doi:10.14214/sf.466

Kukko, A., Kaasalainen, S., & Litkey, P. (2008). Effect of incidence angle on laser scanner intensity and surface data. *Applied Optics, 47*(7), 986-992. doi:Doi 10.1364/Ao.47.000986

Lane, S. N., & Chandler, J. H. (2003). Editorial: The generation of high quality topographic data for hydrology and geomorphology: New data sources, new applications and new problems. *Earth Surface Processes and Landforms, 28*(3), 229-230. doi:10.1002/esp.479

LaRocque, P. (2017). Personal communication.

LaRocque, P., Smith, B., & Shaker, A. (June, 2015). The Optech Titan: A Multi-Spectral Lidar for Multiple Applications. *16th Annual JALBTCX Airborne Coastal Mapping and Charting Workshop.*

Legleiter, C. J. (2012). Remote measurement of river morphology via fusion of LiDAR topography and spectrally based bathymetry. *Earth Surface Processes and Landforms, 37*(5), 499-518. doi:10.1002/esp.2262

Legleiter, C. J., Overstreet, B. T., Glennie, C. L., Pan, Z. G., Fernandez-Diaz, J. C., & Singhania, A. (2016). Evaluating the capabilities of the CASI hyperspectral imaging system and Aquarius bathymetric LiDAR for measuring channel morphology in two distinct river environments. *Earth Surface Processes and Landforms, 41*(3), 344-363. doi:10.1002/esp.3794

Legleiter, C. J., Roberts, D. A., & Lawrence, R. L. (2009). Spectrally based remote sensing of river bathymetry. *Earth Surface Processes and Landforms, 34*(8), 1039-1059. doi:10.1002/esp.1787

Lin, M. F., Lucas, H. C., & Shmueli, G. (2013). Too Big to Fail: Large Samples and the p-Value Problem. *Information Systems Research, 24*(4), 906-917. doi:10.1287/isre.2013.0480

Lu, D., Mausel, P., Brondizio, E., & Moran, E. (2004). Change detection techniques. *International Journal of Remote Sensing, 25*(12), 2365-2407. doi:10.1080/0143116031000139863

Lyon, J. G., Yuan, D., Lunetta, R. S., & Elvidge, C. D. (1998). A change detection experiment using vegetation indices. *Photogrammetric Engineering and Remote Sensing, 64*(2), 143-150.

Mahoney, C., Hopkinson, C., Held, A., & Simard, M. (2016). Continental-Scale Canopy Height Modeling by Integrating National, Spaceborne, and Airborne LiDAR Data. *Canadian Journal of Remote Sensing, 42*(5), 574-590. doi:10.1080/07038992.2016.1196580

Mandlburger, G., & Briese, C. (2007). Using Airborne Laser Scanning for Improved Hydraulic Models. *Modsim 2007: International Congress on Modelling and Simulation*, 731-738.

Mandlburger, G., Pfennigbauer, M., & Pfeifer, N. (2013). Analyzing near water surface penetration in laser bathymetry—A case study at the River Pielach. *In Proceedings of ISPRS Annals of the Photogrammetry, Remote Sensing and Spatial Information Sciences, Antalya, Turkey,.*

Matikainen, L., Karila, K., Hyyppa, J., Litkey, P., Puttonen, E., & Ahokas, E. (2017). Object-based analysis of multispectral airborne laser scanner data for land cover classification and map updating. *Isprs Journal of Photogrammetry and Remote Sensing, 128*, 298-313. doi:10.1016/j.isprsjprs.2017.04.005

Milenkovic, M., Wagner, W., Quast, R., Hollaus, M., Ressl, C., & Pfeifer, N. (2017). Total canopy transmittance estimated from small-footprint, full-waveform airborne LiDAR. *Isprs Journal of Photogrammetry and Remote Sensing, 128*, 61-72. doi:10.1016/j.isprsjprs.2017.03.008

Morsdorf, F., Nichol, C., Malthus, T., & Woodhouse, I. H. (2009). Assessing forest structural and physiological information content of multi-spectral LiDAR waveforms by radiative transfer modelling. *Remote Sensing of Environment, 113*(10), 2152-2163. doi:10.1016/j.rse.2009.05.019

Morsy, S., Shaker, A., & El-Rabbany, A. (2017). Multispectral LiDAR Data for Land Cover Classification of Urban Areas. *Sensors, 17*(5). doi:10.3390/s17050958

Morsy, S., Shaker, A., El-Rabbany, A., & LaRocque, P. E. (2016). Airborne Multispectral Lidar Data for Land-Cover Classification and Land/Water Mapping Using Different Spectral Indexes. *Xxiii Isprs Congress, Commission Iii, 3*(3), 217-224. doi:10.5194/isprsannals-III-3-217-2016

Nicodemus, F. E., Richmond, J. C., Hsia, J. J., Ginsgerb, I. W., & Limperis, T. (1977). *Geometrical considerations and nomenclature for reflectance.* . Washington, DC.

Noble, S. D., Boere, A., Kondratowicz, T., Crowe, T. G., Brown, R. B., & Naylor, D. A. (2008). Characterization of a low-cost diffuse reflectance coating. *Canadian Journal of Remote Sensing, 34*(2), 68-76. doi:DOI 10.5589/m08-012

Okhrimenko, M. (2017). Code for virtual WSM generation. Retrieved from https://github.com/MaximOkhrimenkoUofL/Thesis_bathy

Okhrimenko, M., & Grabarnik, P. (2016, October 16-21). *Segmentation of LiDAR points in forest environment based on unidirected graphs.* Paper presented at the VII International Conference "Mathematical Biology and Bioinformatics" Pushchino, Moscow Region, Russia.

Optech Titan. (January, 2017). Retrieved from http://www.teledyneoptech.com/index.php/product/titan/

Penny, M. F., Billard, B., & Abbot, R. H. (1989). LADS—the Australian Laser Airborne Depth Sounder. *International Journal of Remote Sensing, 10*(9), 1463-1479. doi:10.1080/01431168908903984

Perry, C. R., & Lautenschlager, L. F. (1984). Functional Equivalence of Spectral Vegetation Indexes. *Remote Sensing of Environment, 14*(1-3), 169-182. doi:Doi 10.1016/0034-4257(84)90013-0

Pettorelli, N. (2013). *The Normalized Difference Vegetation Index*: Oxford University Press.

Rees, W. G. (2004). *Physical Principles of Remote Sensing* (2nd ed.): Cambridge University Press.

Roncat, A., Morsdorf, F., Briese, C., Wagner, W., & Pfeifer, N. (2014). Laser Pulse Interaction with Forest Canopy: Geometric and Radiometric Issues. *Forestry Applications of Airborne Laser Scanning: Concepts and Case Studies, 27*, 19-41. doi:10.1007/978-94-017-8663-8_2

Rouse Jr, J., Haas, R. H., Schell, J. A., & Deering, D. W. (1974). Monitoring vegetation systems in the Great Plains with ERTS. *NASA special publication, 351*.

Sabatini, R., & Richardson, M. (2013). Novel atmospheric extinction measurement techniques for aerospace laser system applications. *Infrared Physics & Technology, 56*, 30-50. doi:10.1016/j.infrared.2012.10.002

Schott, J. R. (2007). *Remote Sensing: The Image Chain Approach*: Oxford University Press; 2 edition.

Schwarz, K.-P., Chapman, M. A., Cannon, M. E., Gong, P., & Cosandier, D. (June 6-10, 1994, Ottawa). A Precise Positioning/Attitude System in Support of Airborne Remote Sensing. *Proceedings of the ISPRS Commission II*, 191-202.

Skolnik, M. (2008). *Radar Handbook*: McGraw-Hill Education.

Steven, M. D., Malthus, T. J., Baret, F., Xu, H., & Chopping, M. J. (2003). Intercalibration of vegetation indices from different sensor systems. *Remote Sensing of Environment, 88*(4), 412-422. doi:10.1016/j.rse.2003.08.010

Stoker, J. M., Cochrane, M. A., & Roy, D. P. (2014). Integrating Disparate Lidar Data at the National Scale to Assess the Relationships between Height Above Ground,

Land Cover and Ecoregions. *Photogrammetric Engineering and Remote Sensing, 80*(1), 59-70. doi:Doi 10.14358/Pers.80.1.59

Tyler, J. E. (1968). The Secchi disc. *Luminology and Oceanography, 13*(1). doi:10.4319/lo.1968.13.1.0001

Vain, A., Kaasalainen, S., Hyyppä, J., & Ahokas, E. (2009). Calibration of laser scanning intensity data using brightness targets. The method developed by the Finnish Geodetic Institute. *Geodezija ir Kartografija, 35*(3), 77-81.

Vain, A., Kaasalainen, S., Pyysalo, U., Krooks, A., & Litkey, P. (2009). Use of Naturally Available Reference Targets to Calibrate Airborne Laser Scanning Intensity Data. *Sensors, 9*(4), 2780-2796. doi:10.3390/s90402780

Vain, A., Yu, X. W., Kaasalainen, S., & Hyyppa, J. (2010). Correcting Airborne Laser Scanning Intensity Data for Automatic Gain Control Effect. *Ieee Geoscience and Remote Sensing Letters, 7*(3), 511-514. doi:10.1109/Lgrs.2010.2040578

Vosselman, G., & Maas, H. (2010). *Airborne and Terrestrial Laser Scanning*. FL, Boca Raton: CRC Pres.

Wagner, W. (2010). Radiometric calibration of small-footprint full-waveform airborne laser scanner measurements: Basic physical concepts. *Isprs Journal of Photogrammetry and Remote Sensing, 65*(6), 505-513. doi:10.1016/j.isprsjprs.2010.06.007

Wagner, W., Ullrich, A., Ducic, V., Melzer, T., & Studnicka, N. (2006). Gaussian decomposition and calibration of a novel small-footprint full-waveform digitising airborne laser scanner. *Isprs Journal of Photogrammetry and Remote Sensing, 60*(2), 100-112. doi:10.1016/j.isprsjprs.2005.12.001

Wagner, W., Ulrich, A., Melzer, T., Briese, C., & Kraus, K. (2004). *From single-pulse to full-waveform airborne laser scanners: Potential and practical challenges* (Vol. 35).

Wallace, A., Nichol, C., & Woodhouse, I. (2012). Recovery of Forest Canopy Parameters by Inversion of Multispectral LiDAR Data. *Remote Sensing, 4*(2), 509-531. doi:10.3390/rs4020509

Wehr, A., & Lohr, U. (1999). Airborne laser scanning - an introduction and overview. *Isprs Journal of Photogrammetry and Remote Sensing, 54*(2-3), 68-82. doi:Doi 10.1016/S0924-2716(99)00011-8

Westfeld, P., Maas, H. G., Richter, K., & Weiss, R. (2017). Analysis and correction of ocean wave pattern induced systematic coordinate errors in airborne LiDAR bathymetry. *Isprs Journal of Photogrammetry and Remote Sensing, 128*, 314-325. doi:10.1016/j.isprsjprs.2017.04.008

Westfeld, P., Richter, K., Maas, H. G., & Weiss, R. (2016). Analysis of the Effect of Wave Patterns on Refraction in Airborne Lidar Bathymetry. *XXIII ISPRS Congress, Commission I, 41*(B1), 133-139. doi:10.5194/isprsarchives-XLI-B1-133-2016

Whitfield, P. H., & Pomeroy, J. W. (2016). Changes to flood peaks of a mountain river: implications for analysis of the 2013 flood in the Upper Bow River, Canada. *Hydrological Processes, 30*(25), 4657-4673. doi:10.1002/hyp.10957

Woodget, A. S., Carbonneau, P. E., Visser, F., & Maddock, I. P. (2015). Quantifying submerged fluvial topography using hyperspatial resolution UAS imagery and structure from motion photogrammetry. *Earth Surface Processes and Landforms, 40*(1), 47-64. doi:10.1002/esp.3613

Woodhouse, I. H., Nichol, C., Sinclair, P., Jack, J., Morsdorf, F., Malthus, T. J., & Patenaude, G. (2011). A Multispectral Canopy LiDAR Demonstrator Project. *Ieee Geoscience and Remote Sensing Letters, 8*(5), 839-843. doi:10.1109/Lgrs.2011.2113312

Wu, W. M., Rodi, W., & Wenka, T. (2000). 3D numerical modeling of flow and sediment transport in open channels. *Journal of Hydraulic Engineering-Asce, 126*(1), 4-15. doi:Doi 10.1061/(Asce)0733-9429(2000)126:1(4)

Xu, H. Q. (2006). Modification of normalised difference water index (NDWI) to enhance open water features in remotely sensed imagery. *International Journal of Remote Sensing, 27*(14), 3025-3033. doi:Doi 10.1080/01431160600589179

Yan, W. Y., Shaker, A., & El-Ashmawy, N. (2015). Urban land cover classification using airborne LiDAR data: A review. *Remote Sensing of Environment, 158*, 295-310. doi:10.1016/j.rse.2014.11.001

Yan, W. Y., Shaker, A., Habib, A., & Kersting, A. P. (2012). Improving classification accuracy of airborne LiDAR intensity data by geometric calibration and radiometric correction. *Isprs Journal of Photogrammetry and Remote Sensing, 67*, 35-44. doi:10.1016/j.isprsjprs.2011.10.005

Yu, X. W., Hyyppa, J., Kukko, A., Maltamo, M., & Kaartinen, H. (2006). Change detection techniques for canopy height growth measurements using airborne laser scanner data. *Photogrammetric Engineering and Remote Sensing, 72*(12), 1339-1348. doi:Doi 10.14358/Pers.72.12.1339

Zhang, Y. Q., Chen, J. M., Miller, J. R., & Noland, T. L. (2008). Leaf chlorophyll content retrieval from airborne hyperspectral remote sensing imagery. *Remote Sensing of Environment, 112*(7), 3234-3247. doi:10.1016/j.rse.2008.04.005

Appendix I. Optech Titan Specification

Laser Configuration

Channel1	1550 nm IR
Channel2	1064 nm NIR
Channel3	532 nm visible
Beam divergence	Channel 1 & 2: =0.35 mrad {1/e) Channel 3: =0.7 mrad (1/e)
Laser classification	Class IV (US FDA 21 CFR 10 40.10 and 1040.11; IEC/EN 60825-1)
Operating altitudes.[1][2]	Topographic: 300 - 2000 m AGL, all channels Bathymetric: 300 - 600 m AGL, 532 nm
Depth performance [1][A]	Dmax (m) = 1.5/Kd, where Kd is the diffuse attenuation coefficient of the water
Effective PRF	Programmable; 50 - 300 kHz (per channel); 900 kHz total
Point density [4]	Bathymetric : >15 pts/m2 Topographic: >45 pts/m2
Scan angle (FOV)	Programmable; 0 - *60°* maximum
Effective scan frequency	Programmable; 0 - 210 Hz
Swath width	0 -115% of AGL
Horizontal accuracy.[2][3]	1/7,500 x altitude; 1 o
Elevation accuracy[2][3]	< 5-10 cm; Io
Laser range precision [5]	< 0.008 m; 1 o

Camera Configuration

Q/A camera	29 MP RGB/CIR; 5.5 µm pixel; 6,600 x 4,400 pixels; 0.5 sec/frame
Medium format camera (optional)	80 MP RGB/CIR; 5.2 µm pixel; 10,320 x 7,760 pixels; 2.5 sec/frame

Sensor Configuration

Gyro-stabilization	SOMAG GSM3000/4000 compatible (optional)
Roll compensation	Programmable; ±5° at SO· FOV; increasing with decreasing FOV from SO·
Position and orientation system	POSAV APSO (OEM); 220-channel dual frequency GNSS receiver
Inertial measurement unit	ITAR-free FMU-301 (JMU-46)
Flight management system	Optech FMS with real-time point display
Minimum target separation distance	<1.0 m (discrete)
Range capture	Up to 4 range measurements for each pulse, including last
Intensity capture	Up to 4 range measurements for each pulse, including last 12 bit dynamic measurement and data range

Data storage drives	Removable solid state drive SSD (SATA II)
Waveform capture	12 bit, 1 Gs/sec (optional)
Power requirements	28 V (continuous); 800W (nominal); 30A
Operation temperature	0° to +35°C
Dimensions and weight	Sensor head : 850 x 500 x 680 mm, 71kg Control rack: 485 x 535 x 545 mm, 45 kg

[1.] 20% reflective surface or bottom. Note: Vegetation and other targets may result in a lower response in the green channel, as compared to the IR channels. Lower operating altitudes may be required to ensure measurable returns from low reflectance targets at 532 nm.

[2.] Dependent on selected operational parameters using nominal *50* • FOV in standard atmospheric conditions (i.e. 23 km visibility)

[3.] Valid for *1064* nm and *1550* nm channels on above-water targets only

[4.] Assumes *400 m* AGL, *60 m/s* aircraft speed, 40 • FOV

[5.] Under Teledyne Optech test conditions